



TECHNISCHE UNIVERSITÄT MÜNCHEN

Fakultät für Chemie

**Mechanistic Studies on Artificial Photosynthesis:
Photocatalytic Water Oxidation and Carbon
Dioxide Reduction with Carbon Nitrides**

DISSERTATION

Zur Erlangung des akademischen Grades
Doktor der Naturwissenschaften

vorgelegt von
Johannes Ehrmaier

Garching bei München, 2019



TECHNISCHE UNIVERSITÄT MÜNCHEN

Fakultät für Chemie

**Mechanistic Studies on Artificial Photosynthesis:
Photocatalytic Water Oxidation and Carbon
Dioxide Reduction with Carbon Nitrides**

Johannes Ehrmaier

Vollständiger Abdruck der von der
Fakultät für Chemie der Technischen Universität München
zur Erlangung des akademischen Grades eines
Doktors der Naturwissenschaften
genehmigten Dissertation

Vorsitzende:

Prof. Dr. Tanja Gulder

Prüfer der Dissertation:

1. Prof. Dr. Wolfgang Domcke
2. Prof. Dr. Karsten Reuter
3. Prof. Dr. Peter Saalfrank (schriftliches Gutachten)
Prof. Dr. Corinna Hess (mündliche Prüfung)

Die Dissertation wurde am 29.5.2019 bei der Technischen Universität München eingereicht und durch die Fakultät für Chemie am 22.7.2019 angenommen.

Abstract

Polymeric carbon nitride materials consisting of triazine or heptazine building blocks recently have attracted extensive interest in the field of water oxidation and CO₂ reduction photocatalysis. However, the underlying mechanisms are not understood. In this work, the photochemical reaction mechanisms in hydrogen-bonded complexes of the aromatic chromophores pyridine, triazine and heptazine with water and carbon dioxide molecules have been investigated with wave-function based ab initio electronic-structure calculations. These calculations revealed the existence of low-barrier excited-state pathways for H-atom transfer reactions from water to the photoexcited chromophores (water oxidation) as well as from the reduced chromophores to carbon dioxide (CO₂ reduction). Moreover, the dynamics of a heptazine molecule in an ensemble of 120 water molecules has been simulated with density functional theory. The results provide evidence that the oxidation of water molecules by photoexcited N-heterocycles is possible in cold molecular beams as well as in liquid water at room temperature. These results have recently been confirmed by experimental investigations which were stimulated by the present work. The pyridinyl-CO₂ complex has been selected as model system for the exploration of the light-driven CO₂ reduction reaction, since prior experimental and computational studies exist for this system. It has been demonstrated that a barrierless reaction pathway for H-atom transfer from the photoexcited pyridinyl radical to CO₂ exists. Taken together, these results provide evidence for a novel biphotonic reaction cycle for integrated water oxidation and carbon dioxide reduction. With the first photon, an H-atom is transferred from a water molecule to the N-heterocyclic chromophore, generating a free OH radical and the reduced chromophore. With a second photon, the excess H-atom is transferred from the hydrogenated chromophore to a CO₂ molecule, which reduces the CO₂ molecule and regenerates the chromophore. These results provide a blueprint for a novel artificial photosynthesis cycle with carbon nitride materials, in which the N-heterocyclic chromophore simultaneously acts as absorber and as redox-active catalyst.

Zusammenfassung

Polymere Kohlenstoffnitride, welche aus Triazin- oder Heptazin- Bausteinen bestehen, sind von großem Interesse im Bereich der photokatalytischen Oxidation von Wasser und Reduktion von Kohlenstoffdioxid. Die zugrundeliegenden Mechanismen sind jedoch nicht bekannt. In dieser Arbeit wurden photochemische Reaktionsmechanismen in Wasserstoffbrücken-gebundenen Komplexen der aromatischen Chromophore Pyridin, Triazin und Heptazin mit Wasser- und Kohlenstoffdioxid-Molekülen mit wellenfunktions-basierten ab initio Elektronenstruktur-Methoden untersucht. Diese Rechnungen liefern Evidenz für Reaktionswege mit niedrigen Barrieren für H-Atom Transfer-Reaktionen von Wasser zu den photoangeregten Chromophoren (Wasseroxidation) und von den photoangeregten reduzierten Chromophoren zu Kohlenstoffdioxid (CO_2 -Reduktion). Außerdem wurde die Dynamik eines photoangeregten Heptazin-Moleküls in einem Ensemble von 120 Wasser-Molekülen mit Dichtefunktionaltheorie simuliert. Die Ergebnisse zeigen, dass die Oxidation von Wasser-Molekülen durch photoangeregte N-Heteroaromaten sowohl in kalten Molekülstrahlen als auch in flüssigem Wasser bei Raumtemperatur möglich ist. Kürzlich wurden diese Ergebnisse durch Experimente bestätigt, welche durch die vorliegende Arbeit stimuliert wurden. Der Pyridinyl- CO_2 -Komplex wurde als Modellsystem für die Untersuchung der photoinduzierten CO_2 -Reduktion gewählt, da bereits experimentelle und theoretische Studien darüber existieren. Wir konnten zeigen, dass ein barrierefreier Reaktionsweg für den H-Atom Transfer von dem photoangeregten Pyridinyl-Radikal zum CO_2 existiert. Insgesamt belegen diese Ergebnisse die Existenz eines neuartigen biphotonischen Zyklus für eine integrierte Wasseroxidation und Kohlenstoffdioxid-Reduktion. Mit dem ersten Photon wird ein H-Atom von einem Wasser Molekül zu dem N-heteroaromatischen Chromophor übertragen, wobei ein freies OH-Radikal und der reduzierte Chromophor gebildet werden. Mit dem zweiten Photon wird das zusätzliche H-Atom vom reduzierten Chromophor zum CO_2 - Molekül übertragen. Damit wird das CO_2 -Molekül reduziert und der Chromophor regeneriert. Diese Ergebnisse liefern eine Blaupause für einen neuartigen künstlichen Photosynthese-Zyklus, bei dem der N-heterozyklische Chromophor gleichzeitig als Absorber und als redoxaktiver Katalysator fungiert.

To Nina

Firstly, I would like to express my sincere gratitude to my supervisor Prof. Wolfgang Domcke for the continuous support of my PhD, for his patience, trust, and enormous knowledge. I benefitted from a superb balance between guidance and freedom which was essential for my personal (academic) development and the project. I could not have imagined having a better advisor, mentor and idol for my PhD study.

Moreover, special thanks is owed to all members and visitors of the Domcke research group for the relaxed and productive time and the wonderful working atmosphere, which I was allowed to enjoy.

Finally, I want to thank my family for all their support, patience and understanding during my whole studies. Particular thanks is given to Nina, who has always supported my passion for solar energy conversion.

Thank you!

This doctoral thesis is a publication-based thesis and the herein presented work has been published in international peer-reviewed scientific journals. This work provides a compact literature review on water oxidation and CO₂ reduction with carbon-nitride materials and proposes a novel biphotonic artificial photosynthesis cycle. An overview on the employed ab-initio methods as well as photochemical concepts is given. For each of the four published papers, a short summary as well as a description of my contribution to each piece of work is provided. In the last section, the existing mechanistic explanations of the literature are critically analyzed and the individual publications of this work are combined as an artificial photosynthesis cycle. Possible future extensions and research directions are proposed.

The presented work was performed from April 2016 to May 2019 in the Department of Chemistry of the Technical University of Munich under the supervision of Prof. Dr. Wolfgang Domcke.

Johannes Ehrmaier
Garching, May 2019

“It’s easy to make scrambled eggs, but the opposite is difficult.”

Wolfgang Domcke

Contents

1	Introduction	1
2	Electronic Structure Methods and Photochemical Reaction Paths	11
2.1	Electronic Structure Methods.....	11
2.1.1	Wave-Function Based Methods.....	11
2.1.1.1	MP2 Method	11
2.1.1.2	ADC(2) Method	13
2.1.1.3	CASSCF/CASPT2 Method	15
2.1.2	Density-Based Methods	17
2.1.2.1	DFT Method	17
2.1.2.2	TDDFT Method.....	19
2.2	Photochemical Reaction Paths and Potential-Energy Surfaces .	20
3	Summary of Publications	23
3.1	Mechanism of Photocatalytic Water Splitting with Triazine-Based Carbon Nitrides: Insights from Ab Initio Calculations for the Triazine-Water Complex.....	24
3.2	Mechanism of Photocatalytic Water Splitting with Graphitic Carbon Nitride: Photochemistry of the Heptazine-Water Complex.....	26
3.3	Mechanism of Photocatalytic Water Oxidation by Graphitic Carbon Nitride.....	28
3.4	Role of the Pyridinyl Radical in the Light-Driven Reduction of Carbon Dioxide: A First-Principles Study.....	30
4	Discussion and Summary.....	33
	Bibliography	39
	Appendix: Publications	57

1 Introduction

The growing modern society causes an increasing worldwide energy demand, which has mostly been covered by combustion of fossil fuels.¹ Consequently, the atmospheric CO₂ level has been rapidly increasing during the last 100 years,² which may have dramatic negative impacts on the environment. The benefits of chemical fuels as energy carriers are unique: They provide high energy density, are easily transportable and can be stored for long time. Aiming towards a sustainable energy supply, the light of the sun, as the largest sustainable primary energy source, will play a key role. Considering the advantages of chemical fuels and sun light as unique primary energy source, the dream reaction for a sustainable carbon-neutral energy supply is the conversion of solar energy directly into chemical fuels. This leads to an artificial photosynthesis cycle imitating natural photosynthesis, in which solar energy is used to oxidize water and to reduce CO₂.

In 1972, Fujishima and Honda reported for the first time photoelectrochemical water splitting using TiO₂ as electrode material and photocatalyst.³ Many studies on the photocatalytic function of TiO₂ followed, which investigated the mechanism and tried to overcome limitations.⁴⁻⁶ The present status of photocatalytic water oxidation with semiconductor materials, in particular TiO₂, has been summarized in several review articles.⁷⁻¹⁰ Major problems of this approach are the wide bandgap of TiO₂, due to which only a small part of the solar spectrum can be used, the fast recombination of electrons and holes, which reduces the efficiency, and the high overpotentials which are needed to drive the reaction.

A milestone in the search for molecular catalysts for water oxidation was the work of Meyer and coworkers, who reported water oxidation with a homogenous ruthenium-based molecular catalyst, the so-called "Blue Dimer".¹¹ Molecular photocatalysts can be divided in two groups. In one group, the compounds act as chromophore and catalyst at the same time. In the other

group, a photosensitizer collects photons and electrons are then transferred to a separate catalyst. Recent progress in this area has been summarized in several review articles.¹²⁻¹⁷ A severe disadvantage of these organometallic systems is that 2nd- or 3rd-row transition metals, for example ruthenium or iridium, are needed, which are rare and expensive. Attempts to use complexes with isoelectronic 1st-row transition metals, which are cheap and earth abundant, were not successful so far due to the short lifetime of charge-transfer states in 1st-row transition metal complexes.¹⁸

During the last decade, a class of organic materials, so called graphitic carbon nitrides, have attracted vast interest in the field of photocatalytic water-splitting.^{19, 20} Carbon nitride polymers are known for a long time. In 1834, Liebig and Berzelius reported the synthesis of a polymer consisting of carbon and nitrogen which Liebig called “melon”.²¹ More than 150 years later, Yanagida and coworkers investigated photoinduced hydrogen evolution with polymeric photocatalysts like polyphenylene and polypyridine, a sacrificial electron donor and nano-scale noble-metal particles.^{22, 23} In 2009, Wang and coworkers reported sacrificial photocatalytic hydrogen evolution from water with a graphitic carbon nitride catalyst.²⁴ Since then, thousands of scientific articles have been published on photocatalysis with graphitic carbon nitride.¹⁹ Due to its extraordinary photostability, facile synthesis, non-toxicity, earth abundancy and its photochemical and photophysical properties, it looks very attractive for future sustainable large-scale energy-conversion applications.

Most carbon-nitride materials are based on either triazine or heptazine (tri-s-triazine) units as building blocks.²⁰ Polymeric carbon nitrides with triazine units have been synthesized²⁵⁻²⁸ and triazine-based covalent organic frameworks were constructed²⁹⁻³¹ and tested for hydrogen evolution.³²⁻³⁷ Most carbon-nitride materials, however, are one-dimensional heptazine-based polymer chains that are arranged in two-dimensional sheets without long-range ordered crystalline structure.³⁸ In the last decade, a vast amount of modified carbon nitride materials has been synthesized using different precursor materials, generating metallic/organic/inorganic heterojunctions, varying the structure and inserting dopants and defect sites.^{20, 39-44}

The majority of studies with these materials is devoted to the investigation of hydrogen evolution from water using sacrificial electron donors or hole scavengers, such as triethanolamine (TEOA).^{24, 42, 45-50} There exist also a few reports on non-sacrificial and stoichiometric evolution of molecular hydrogen and oxygen with carbon-nitride materials with and without Pt co-doping.⁵¹⁻⁵³

From the computational point of view, the thermodynamics of the formation of different carbon-nitride structures has been investigated with density functional theory (DFT) calculations.^{54, 55} The electronic structure (band structure) and the molecular structure have been analyzed^{56, 57} and stacking effects were simulated.^{58, 59} The electronic structure of heterojunctions with carbon nanodots and metal atoms was analyzed.^{60, 61} Exciton binding energies, absorption spectra and reduction potentials in clusters were calculated.⁶²⁻⁶⁴ Water adsorption and desorption on carbon-nitrides were investigated to suggest possible reaction pathways for the water splitting reaction.⁶⁵⁻⁶⁸ Overall, carbon nitrides provide a promising alternative for future energy conversion applications, but the underlying mechanism of water splitting under visible irradiation is not known.

In 2013, Liu et al. suggested a biphotonic water-splitting cycle for the pyridine-H₂O complex.^{69, 70} The water-splitting reaction in this system occurs in two steps, as is schematically shown in Fig. 1. The first photon induces an H-atom transfer from water to the N-atom of pyridine, generating a pyridinyl radical (hydrogenated catalyst) and a hydroxyl radical. By absorption of a second photon, the transferred H-atom is detached from the pyridinyl radical, recovering the chromophore and releasing an H-atom. Later on, this photocatalytic cycle has been computationally explored for complexes of several heterocyclic molecules like acridine,⁷¹ acridine-orange,⁷² benzacridine⁷² and benzoquinone⁷³ with water molecules.

Jouvet and coworkers have experimentally observed both steps of the photocatalytic reaction in pyridine-water clusters in a supersonic jet.⁷⁴ For pyridine-water clusters containing more than three water molecules, the

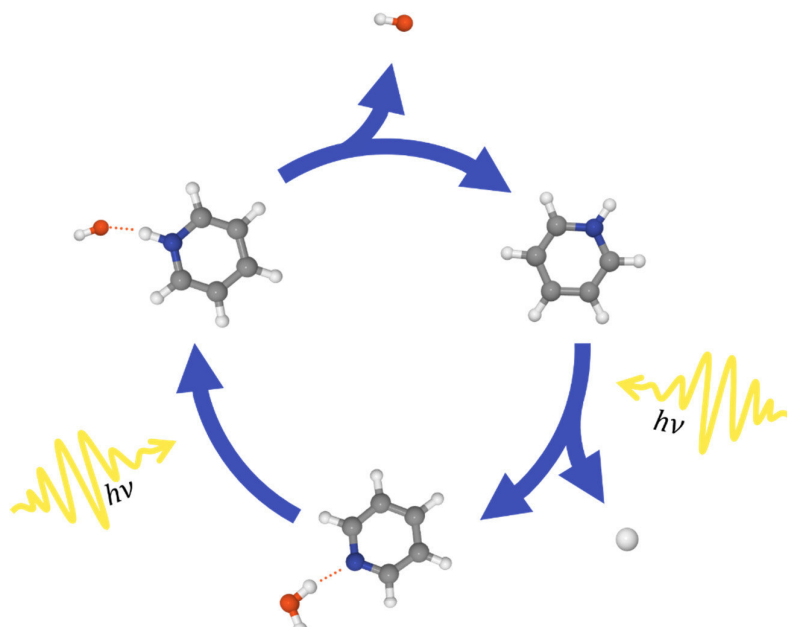


Fig. 1: Schematic illustration of the molecular biphotonic splitting mechanism with pyridine as chromophore and photocatalyst. The first photon drives an H-atom transfer from water to pyridine, forming a pyridinyl radical and a hydroxyl radical. With the second photon, the transferred H-atom is detached from the pyridinyl radical. Reproduced from Ref. 69.

H-atom transfer process from water to pyridine and the H-atom detachment reaction from the pyridinyl radical were detected with mass spectrometry.⁷⁴

While the majority of experimental and theoretical studies of artificial photosynthesis are focussed on the evolution of molecular hydrogen and/or molecular oxygen from water, the ultimate goal is the conversion of CO_2 to liquid fuels which are easy to store and to transport. Conversion of CO_2 to methane was already investigated by Sabatier more than 100 years ago. Nowadays, molecular hydrogen and CO_2 are transformed to methane, methanol and other hydrocarbons under high pressure and temperature.⁷⁵⁻⁷⁸ Conditions, reactor design and catalysts have been continuously optimized for this process.⁷⁹⁻⁸¹ Due to their comparatively low price, high efficiency and high selectivity, Ni catalysts are nowadays mostly used in so-called power to gas applications.⁸² There are several methanation plants at pilot or commercial

stage.^{82, 83} The hydrogen for the Sabatier process is produced by the electrolysis of water so that overall electric power is converted to methane.⁷⁹

Another approach is electrochemical reduction of CO₂ under ambient conditions.⁸⁴⁻⁸⁷ In the photoelectrochemical approach, a semiconductor material is used to generate electron-hole pairs under irradiation which then drive CO₂ reduction reactions.¹⁴ It has been found that copper catalysts are able to break the C-O bond in CO₂ which can lead to useful feedstock molecules.⁸⁸ A variety of materials and heterojunctions has been tested for the photoelectrochemical reduction of CO₂ during the last decades.⁸⁹

In 2007, Goettmann et al. reported CO₂ reduction to CO with a mesoporous graphitic carbon-nitride material.⁹⁰ Later, Dong and Zhang showed non-sacrificial CO₂ reduction to CO with a carbon-nitride polymer as photocatalyst and water as reducing agent.⁹¹ Several studies on CO₂ reduction followed using heterojunctions and doped carbon-nitride materials.⁹²⁻¹⁰¹

As it is relevant for the present work, a recent intensive discussion on the role of the pyridinyl radical in the photochemical or photoelectrochemical reduction of CO₂ is mentioned here. Bocarsly and coworkers published a series of articles on CO₂ reduction with pyridinyl radicals in (photo)electrochemical cells.¹⁰²⁻¹⁰⁹ Moreover, Colussi and coworkers observed homogenous reduction of CO₂ to OCOH by pyridinyl radicals.¹¹⁰ However, from the thermodynamics of their first-principle simulations, Keith and Carter, on the other hand, concluded on the basis of first-principles calculations that the reduction of CO₂ by pyridinyl radicals is thermodynamically impossible.^{111, 112} Detailed alternative mechanisms for a two-electron reduction reaction of CO₂ have been suggested, some of them also including an electrode surface.¹¹³⁻¹²¹ Musgrave and coworkers calculated barrier-heights for the reduction reaction of CO₂ with pyridinyl radicals and reported a decrease of the barrier when more water molecules are considered. They proposed that pyridinyl radicals may possibly reduce CO₂ in bulk water.¹²²

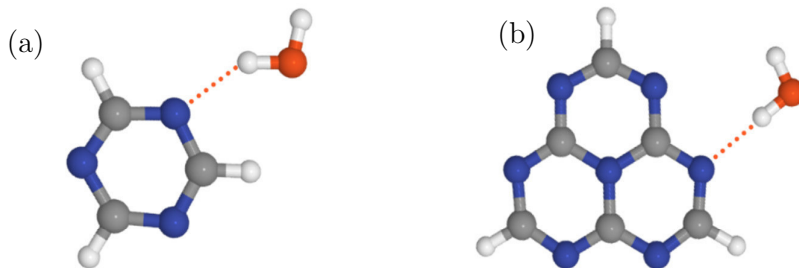


Fig. 2: Structures of the (a) the triazine-water complex and (b) the heptazine-water complex.

In this work, we extend the biphotonic water-splitting mechanism of Domcke and coworkers⁶⁹ to the carbon nitrides triazine and heptazine as well as to the carbon dioxide reduction reaction. While pyridine, as the simplest heterocycle, was chosen as model system for theoretical explorations of the fundamental photocatalytic reaction mechanisms, triazine and heptazine are the building blocks of the currently most extensively studied organic photocatalytic materials, covalent organic frameworks¹²³ and graphitic carbon nitride.²⁰ The two fundamental reactions of water oxidation are shown in Eqs. (1) and (2), where A stands for one of the chromophores (triazine or heptazine).



In the first photoinduced reaction, Eq. (1), a hydrogen atom is abstracted from a water molecule by the photoexcited chromophore, generating an OH radical and the reduced chromophore, AH. In the second photoinduced reaction, the surplus hydrogen atom is detached from the AH radical, which yields a free H-atom and regenerates the catalyst. While most previous investigations of the water oxidation reaction were focussed on the thermodynamics of educts and products, we are guided in our studies by a detailed mechanistic picture of all individual steps of the water oxidation reaction. The detailed understanding of the reaction mechanisms will allow future rational and systematic improvements of the materials.

Triazine is the building block of photocatalytically active covalent organic frameworks.¹²³ Due to the small size of this system, accurate electronic-structure calculations are possible for the triazine-water complex (shown in Fig. 2a) and a full analysis of the photochemistry is computationally feasible. Several possible reaction paths for the H-atom transfer reaction from water to triazine on singlet and triplet potential-energy surfaces were investigated in the present work. The decisive feature of the potential-energy surface of the reaction is the barrier connecting the Franck-Condon region with the biradical. To estimate this barrier, two-dimensional relaxed potential-energy surfaces were constructed for the lowest singlet and triplet excited states. To characterize the second photoinduced reaction, the H-atom detachment reaction from the triazinyl radical, rigid scans along the reaction coordinate were constructed.

As most carbon nitride materials used for water splitting are based on heptazine units, the most relevant model system for photoinduced water oxidation with carbon nitrides is the hydrogen-bonded heptazine-water complex, shown in Fig. 2b. The excited-state H-atom transfer reaction from water to heptazine involving a low-lying singlet charge-transfer state of $\pi\pi^*$ character has been explored. Relaxed scans and two-dimensional surfaces were evaluated in a similar manner as for triazine, which reveal that a low-barrier nonadiabatic proton transfer reaction is likely to occur in this system. Moreover, the photoinduced H-atom detachment reaction from the heptazinyl radical has been investigated.

In experimental investigations of the water-splitting reaction, carbon-nitride materials are dispersed in liquid water and a sacrificial reagent and nano-scale Pt particles are added. The aqueous environment may enhance or hinder the reaction. To estimate these environmental effects, we simulated a heptazine chromophore in liquid water with DFT calculations. The water molecules are explicitly taken into account and are treated at the same level of theory as the chromophore to avoid as much as possible crude approximations. To account for the statistical fluctuations of the solvent at room temperature, the complete system was propagated in time and at a large number of snapshots

its absorption spectrum and the density of states was analyzed. The results explain the low-energy region of the experimental absorption spectrum and confirm the mechanism of the H-atom transfer reaction from water to the chromophore, which was inferred from calculations for the heptazine-H₂O cluster.

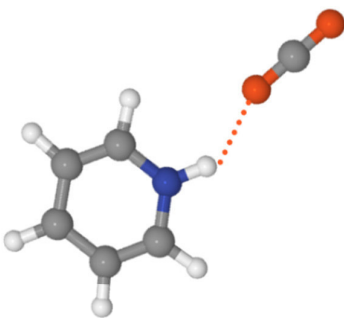


Fig. 3: Structure of the pyridinyl-CO₂ complex.

The free hydrogen atom generated in the biphotonic Domcke-Sobolewski cycle has a much higher reduction potential than the hydrogen molecule. However, even the free H-atom is not suitable for the reduction of CO₂, since the 1s orbital of an H-atom is too compact to interact with the unoccupied orbitals of CO₂, although the kinetic energy of the H-atom generated by photodetachment from the pyridinyl, triazinyl or heptazinyl radicals is sufficient to overcome the barrier for attachment to CO₂. Alternatively to H-atom detachment from the hydrogenated chromophore (Eq. (2)), the H-atom can be directly transferred to a CO₂ molecule after photoexcitation of the hydrogen-bonded A-CO₂ complex (see Fig. 3).



Using ab-initio computational methods, we examined the photochemistry of the hydrogen-bonded pyridinyl-CO₂ complex. Analyzing excited-state potential-energy surfaces along the H-atom transfer reaction from pyridinyl to CO₂, a barrierfree excited-state reaction pathway was found for the CO₂ reduction reaction. In contrast to the ground-state reaction, which is

determined by high barriers and the corresponding kinetics, the excited-state reaction is an ultrafast process, dominated by the dynamical behavior at two conical intersections along the reaction pathway.

Due to the extensive experimental and theoretical work on the role of the pyridinyl radical in the CO₂ reduction reaction, we focussed our computational studies on the pyridinyl-CO₂ complex. The basic reaction mechanisms will be similar for the triazinyl-CO₂ and heptazinyl-CO₂ complexes, which will be investigated in future work.

2 Electronic Structure Methods and Photochemical Reaction Paths

2.1 Electronic Structure Methods

2.1.1 Wave-Function Based Methods

2.1.1.1 MP2 Method

Møller-Plesset (MP) perturbation theory is a post Hartree-Fock method which accounts for the correlation energy in the framework of Rayleigh-Schrödinger perturbation theory. The unperturbed Hamiltonian is the sum of the single-electron Fock operators, which counts the average electron-electron repulsion twice. Consequently, the perturbation is the electron-electron repulsion operator minus twice the averaged one. MP perturbation theory can be carried out up to an arbitrary order n and the methods are accordingly called MP_n methods. The first-order energy correction takes care of the double counting of the averaged electron-electron repulsion energy so that the MP1 energy corresponds to the Hartree-Fock energy. The second-order correction is the first contribution to the correlation energy. Including higher order correction terms may lead to oscillations of the energy and improvements are in general minor and not necessarily systematic.

The computational scaling of MP2 is N^5 , which makes it quite efficient compared to the coupled-cluster method with singles and doubles, which scales like N^6 . Due to its perturbative nature, MP_n is not variational, but it is size extensive. MP2 is the most popular many-body perturbation approach to account for correlation energy. For open-shell systems, the perturbation theory can be implemented with unrestricted Hartree-Fock orbitals, which leads to the unrestricted MP_n method (UMP n). Using restricted open-shell Hartree-Fock orbitals for open-shell systems, the method is called ROHF- MP_n .

Several approximations have been implemented to reduce the computational cost of MP2 calculations. Pulay and Saebø proposed a local correlation approach that leads to a linear scaling MP algorithm.¹²⁴⁻¹²⁶ In the present work, we make use of the resolution-of-identity (RI) approximation which allows an efficient evaluation of two-electron repulsion integrals with negligible errors.¹²⁷⁻¹²⁹ Ochsenfeld and coworkers hold the present record for the largest MP2 calculation with more than 2000 atoms.¹³⁰

For all MP2 and UMP2 calculations of this work the Turbomole program package was used.

2.1.1.2 ADC(2) Method

The energies of excited states can be obtained, among other methods, with Green’s function methods, which extract the desired information from one-particle or two-particle Green’s functions.¹³¹ The excitation energies are poles of the polarization propagator. An efficient approximation scheme for the polarization propagator is the algebraic diagrammatic construction (ADC), which can be derived up to different orders. ADC yields excitation energies, oscillator strengths as well as other molecular properties determined by the polarization propagator. Recently, a third-order ADC scheme has been developed, implemented and benchmarked for excitation energies.¹³² In this work, the second-order ADC, ADC(2), has been used due to its favourable computational cost.

In the strict ADC(2) scheme, the matrix elements for the singly excited states are expanded up to second order of perturbation theory, while the matrix elements for the coupling between singly and doubly excited states are considered up to first order. The energies of the doubly excited states are approximated in zeroth order.¹³³ One advantage of ADC(2), and ADC methods in general, is their ability to describe points of degeneracy of excited-state energies correctly. For instance, conical intersections between excited states of the same symmetry are correctly described, since the excited-state energies are calculated as eigenvalues of a Hermitian secular matrix.¹³³ Moreover, charge-transfer states, Rydberg states and doubly excited states can be described with reasonable computational cost. ADC(2) scales as N^5 and an efficient implementation of analytical gradients allows excited-state geometry optimizations. Therefore, ADC(2) is the method of choice to study excited-state reaction paths for H-atom transfer reactions in small to medium size systems. Like MP2, ADC(2) is size extensive, but not variational.

As the ADC scheme is based on the single-reference Hartree-Fock ground-state wave function, it suffers from the same drawbacks as MP2. In particular, conical intersections involving the electronic ground state require inherently a multi-reference ground-state wave function. Therefore, conical intersections of excited states with the ground state cannot be characterized by ADC methods.

For open-shell systems, an unrestricted ADC(2) (UADC(2)) scheme is available, which is based on unrestricted Hartree-Fock orbitals. UADC(2) has been carefully benchmarked for excited-state energies of organic molecules.¹³⁴ Dreuw and coworkers have recently developed a spin-flip version of ADC (SF-ADC). Here, a triplet state serves as reference state and the ground state is calculated, like an excited state, by an excitation and spin-flip from the reference state.^{135, 136} SF-ADC is particularly suited for few-reference problems and can describe conical intersections between the ground state and excited states correctly.¹³⁷

For all ADC(2)/UADC(2) calculations the Turbomole program package was used.

2.1.1.3 CASSCF/CASPT2 Method

In the multiconfigurational self-consistent field (MCSCF) approach, a linear combination of Slater determinants is chosen as variational trial wave function. The orbitals and configuration-interaction (CI) coefficients are optimized in order to minimize the energy. MCSCF energies are variational and size extensive. The number of configurations has to be restricted in order to limit the computational cost. One solution is to perform a full CI calculation in a limited orbital space. In the complete-active-space self-consistent-field (CASSCF) method, the orbitals are divided in three groups: inactive occupied orbitals, inactive virtual orbitals and active orbitals. The inactive occupied orbitals are kept doubly occupied, the inactive virtual orbitals are kept unoccupied, while in the space of the active orbitals all possible Slater determinants are generated and included in the expansion of the wave function. There are several variations of the CASSCF algorithm, for example, the restricted-active-space SCF algorithm (RASSCF)¹³⁸⁻¹⁴⁰ or the generalized-active-space SCF method (GASSCF)¹⁴⁰, where further restrictions are applied in the construction of Slater determinants. To obtain a balanced description of several electronic states of the same symmetry, their energies can be optimized in a so-called state-averaged CASSCF calculation. By including several Slater determinants in the wave function, MCSCF and CASSCF calculations can describe static electron correlation in situations like bond-breaking reactions and conical intersections. CASSCF calculations are computationally feasible only for relatively small systems and the computational cost scales steeply with the number of active orbitals. Moreover, the selection of the active space requires experience and the results may heavily depend on it.

To account for dynamical correlation effects, multireference perturbation theory can be formulated with a MCSCF wavefunction. The main challenge is to construct the unperturbed Hamiltonian, which has a given MCSCF wavefunction as eigenfunction with the lowest energy. The CASPT2 method¹⁴¹ includes second-order perturbative corrections to the CASSCF energy. The unperturbed Hamiltonian is defined with the help of the CASSCF Fock operator and a projection operator so that its lowest eigenfunction is the CASSCF

wavefunction. In CASPT2 calculations, the perturbative energy correction may lower the energy of certain higher-lying states substantially, which have not been included in the underlying CASSCF calculation. To overcome this problem of so-called intruder states, an imaginary “level shift” parameter is added to the zero-order Hamiltonian to remove the effect of these intruder states and improve convergence. Using CASSCF gradients to optimize geometries and performing single-point CASPT2 calculations to determine the energies is a commonly applied protocol in computational photochemistry.¹⁴²

Finally, we mention a few recently developed concepts to overcome the computational bottleneck of CASSCF calculations for larger active spaces. Alavi and coworkers replaced the Davidson CI eigensolver, which is usually used in CASSCF implementations, with a Full-Configuration-Interaction Quantum-Monte-Carlo (FCIQMC) solver. This reduces memory requirements and computational costs. The algorithm can be well parallelized, which allows the treatment of much larger active spaces.¹⁴³⁻¹⁴⁵ In the Density Matrix Renormalization Group (DMRG) approach, the CI coefficient tensor is decomposed as a tensor product, reducing its dimensionality.^{146, 147} This allows to treat much larger active spaces containing up to 100 electrons in 100 orbitals. Some of the main developers of quantum chemical DMRG are White,¹⁴⁸ Mitrushenkov,¹⁴⁹ Chan,¹⁵⁰ Legeza¹⁵¹ and Reiher¹⁵². Following a different approach, Martinez and coworkers implemented the CASSCF algorithm on GPUs,^{153, 154} which leads to a significant speed up for electronic structure calculations. This implementation was combined with the ab initio multiple spawning method (AIMS) for the description of the nuclear motion, which allows the solution of the full time-dependent Schrödinger equation.¹⁵⁵

All CASSCF/CASPT2 calculations of this work have been performed with the Molpro¹⁵⁶ program package.

2.1.2 Density-Based Methods

2.1.2.1 DFT Method

In wave function based approaches, the $3N$ -dimensional electronic wavefunction has to be computed, with N being the number of electrons. For large systems, the growing dimensionality of the wavefunction leads to an exponential increase of the computational cost. Density functional theory (DFT) is based on the three-dimensional electronic density for the evaluation of the ground-state energy. For DFT, the scaling of the computational cost is N^3 in straightforward implementations due to the diagonalization of an eigenvalue problem. However, linear scaling DFT algorithms are available.¹⁵⁷ The DFT method is based on the Hohenberg-Kohn theorem,¹⁵⁸ which states that for any system of interacting electrons in an external potential there is a one-to-one correspondence between the potential and the ground-state electron density. Minimizing the energy with the exact energy functional leads to the exact ground-state density of the system. The exact functional, however, is not known.

Formally, the energy functional is written as the sum of the kinetic energy functional, the Hartree functional, the functional of the external (nuclear) potential and the exchange-correlation functional. The latter corrects for all missing terms and has to be approximated. Optimizing the energy leads to the same equations as the Schrödinger equation for a fictitious non-interacting system. The resulting one-particle orbitals are the so-called Kohn-Sham orbitals. Strictly speaking, these orbitals do not have any physical meaning, although usually they resemble the Hartree-Fock orbitals.¹⁵⁹

Different levels of approximation have been introduced to estimate the exchange-correlation functional. The simplest approximation is the local density approximation (LDA), which assumes that the exchange-correlation functional behaves locally like the exchange-correlation functional of a uniform electron gas.¹⁵⁹ The next level of approximation is the generalized gradient approximation (GGA), including the gradient of the local density. The popular Perdew-

Burke-Ernzerhof (PBE) functional is one representative of this group.¹⁶⁰ The next steps on Jacob's ladder are so called meta-GGA functionals, which also include corrections to the non-interacting kinetic energy density, and hybrid GGAs, which introduce the Hartree-Fock exchange interaction, for instance the B3LYP (Becke, three-parameter, Lee-Yang-Parr)^{161, 162} and PBE0^{163, 164} functionals. Within the last 25 years, DFT has become a remarkable success story.¹⁶⁵ Nowadays, DFT is applied in many different areas ranging from large scale applications and screening studies in material science^{166, 167} to simulations of biological systems.^{168, 169}

2.1.2.2 TDDFT Method

Time-dependent density functional theory (TDDFT) has been developed for the calculation of excited-state properties. Runge and Gross proved that there is a one-to-one correspondence between the time-dependent density and an external time-dependent potential.¹⁷⁰ Moreover, an action can be formulated which is stationary around the exact density of the system. In TDDFT the energy cannot simply be optimized, but analogously to DFT, time-dependent Kohn-Sham equations can be derived from the variation of the action, which can be written as a set of fictitious time-dependent one-particle Schrödinger equations.¹⁵⁹ As time evolution is considered, an initial condition is needed and an approximation for the time-dependent exchange-correlation functional is required. In the so-called adiabatic approximation, the time-dependent exchange-correlation functional is approximated by the time-independent exchange-correlation functional from DFT using the time-dependent density.¹⁵⁹ This approximation has been used successfully in many applications.

TDDFT is applicable for large systems and generally produces accurate absorption spectra. However, it usually fails for charge-transfer states¹⁷¹ and descriptions of conical intersections.¹⁷² In this work, DFT and TDDFT calculations were performed for the simulation of the absorption spectrum and excited-state properties of heptazine in an environment of 120 water molecules. The CP2K¹⁷³ and the Quantum Espresso¹⁷⁴ program packages were used for these calculations.

2.2 Photochemical Reaction Paths and Potential-Energy Surfaces

In the Born-Oppenheimer approximation, the wave function of a molecular system factorizes in an electronic wave function and a nuclear wave function.¹⁷⁵ This approximation is the most fundamental approximation in theoretical chemistry. For fixed nuclear positions, the electronic Schrödinger equation is solved to obtain the energies of the electronic states. Electronic potential-energy surfaces are obtained by calculating electronic energies on suitable grids of the relevant nuclear coordinates using one of the electronic-structure methods described above. Vibrational motion and chemical reaction dynamics are theoretically described in the Born-Oppenheimer approximation by the solution of the Schrödinger equation for the nuclear motion on a single electronic potential-energy surface. The Born-Oppenheimer approximation is an excellent approximation if the energy gap between electronic potential-energy surfaces is large compared to the energy of nuclear motion. In the case of degeneracies of electronic potential-energy surfaces, so-called conical intersections, the Born-Oppenheimer approximation breaks down and the nuclear dynamics has to be treated on nonadiabatically coupled potential-energy surfaces.¹⁷⁶

To investigate photochemical reactions, cuts of electronic potential-energy surfaces along so-called reaction paths can be constructed.¹⁷⁷ One possibility is to construct a linearly interpolated continuous path between the educt and product geometries of a reaction. Intermediate geometries are obtained by an interpolation in Cartesian or internal coordinates of the molecule. Linearly interpolated paths are not minimum-energy reaction paths and therefore may exhibit apparent barriers which are higher than the true barriers of minimum-energy reaction paths. Nevertheless, for certain reactions or parts of reactions, the energy profiles of linearly interpolated paths can provide a reasonable description of the energetics of the reaction. The advantage of linearly interpolated reaction paths is that they can always be constructed if the initial

and final geometries are given, since only single-point energy calculations have to be performed.

While nonlinear molecules with N atoms have $3N-6$ internal nuclear degrees of freedom, the nuclear coordinate space relevant for a photochemical reaction can often be reduced to a relatively small number of essential reaction coordinates. Such reaction coordinates have to be selected by chemical intuition or by preliminary explorations of the relevant potential-energy surfaces. In the simplest case, a single internal nuclear coordinate can be identified which connects the nuclear configurations of the educt and product (the so-called driving coordinate). One-dimensional energy profiles along such coordinates are called rigid scans. An approximate minimum-energy reaction path, a so-called relaxed scan, can be constructed by fixing the driving coordinate and optimizing the energy of a given electronic state with respect to all other internal nuclear degrees of freedom.¹⁷⁸ True minimum-energy paths can be obtained by following the direction of maximum gradient from first-order saddle points.¹⁷⁹ Relaxed scans reveal barrier heights and possibly the geometries of conical intersections between potential-energy surfaces, which are crucial for the reaction dynamics. If two internal coordinates are relevant for the characterization of a reaction, relaxed two-dimensional potential-energy surfaces can be constructed by fixing the values of two driving coordinates and relaxing all remaining nuclear degrees of freedom.⁶⁹ Two-dimensional potential-energy surfaces reveal saddle points of the reaction and their topography provides precious information on the reaction mechanism.

Crossings or avoided crossings of potential-energy surfaces along a reaction path may be an indication of conical intersections of the multi-dimensional energy surfaces, at which the Born-Oppenheimer approximation breaks down due to a singularity in the nonadiabatic coupling between adiabatic energy surfaces.¹⁸⁰ The large nonadiabatic coupling in the vicinity of conical intersections gives rise to efficient population transfer between the electronic states. Conical intersections are of particular relevance for the photochemical reaction dynamics, as they open pathways for nonradiative electronic relaxation.¹⁸¹

The topography of potential-energy surfaces reveals the energetically possible reaction pathways. The motion of the nuclei on a given potential-energy surface can be described by solving Newton's equations of motion using the local gradients of the potential-energy surface as forces.^{182, 183} Barriers on the potential-energy surface may be overcome if the total available energy is higher than the top of the barrier. In the case of H-atom transfer or proton-transfer reactions, barrier tunneling effects can be relevant which in general requires a quantum mechanical description of the nuclear motion.¹⁸⁴ At conical intersections, the system may change the electronic energy surface and continue on the potential-energy surface of a lower-lying electronic state. Inspection of the topography of potential-energy surfaces is often sufficient to decide qualitatively whether a certain photochemical reaction may occur for given initial conditions. For a more quantitative description of the dynamics of the system, explicit dynamical studies of the nuclear motion are needed, using either quantum wave-packet propagation methods or quasi-classical trajectory simulations.^{185, 186}

3 Summary of Publications

In this section the four articles, on which the thesis is based, are presented. For each paper a short summary is given and the contributions of the candidate are described. The study of the photochemistry of the triazine-H₂O complex is the most complete and comprehensive investigation of the mechanism of water oxidation with N-heterocycles. The second paper on the photochemistry of the heptazine-H₂O complex provides the link to the experimentally explored carbon-nitride materials. The third contribution focusses on the influence of a liquid aqueous environment on the water-splitting reaction with the heptazine chromophore. These articles are ordered from the most fundamental system (triazine-H₂O complex) via the heptazine-H₂O complex to heptazine in bulk water. The last article is on photoinduced CO₂ reduction with the pyridinyl radical. It is an example of the use of N-heterocyclic hydrogenated radicals for the photoreduction of CO₂ to the hydroxy-formyl radical. The four papers are attached to the thesis.

3.1 Mechanism of Photocatalytic Water Splitting with Triazine-Based Carbon Nitrides: Insights from Ab Initio Calculations for the Triazine-Water Complex

Summary of “*Mechanism of photocatalytic water splitting with triazine-based carbon nitrides: insights from ab initio calculations for the triazine-water complex*“ by Johannes Ehrmaier, Mikotaj J. Janicki, Andrzej L. Sobolewski, and Wolfgang Domcke; *Phys. Chem. Chem. Phys.*, **2018**, *20*, 14420-14430.

In this study, we investigated the photoinduced H-atom transfer reaction from water to triazine in the triazine-H₂O complex using the ADC(2) electronic structure method. ADC(2) was carefully benchmarked for the vertical excitation energies using the equation-of-motion coupled-cluster method with singles and doubles (EOM-CCSD), the second-order approximate coupled-cluster (CC2) method and the CASSCF/CASPT2 methods. Several reaction channels involving the singlet and triplet $\pi\pi^*$ and $n\pi^*$ charge-transfer states were analyzed and minimum-energy paths were constructed for the excited-state reactions. The pathway from the Franck-Condon region to the reactive charge-transfer states has been investigated by relaxed two-dimensional potential-energy surfaces for all four different charge-transfer states ($^1\pi\pi^*$, $^1n\pi^*$, $^3\pi\pi^*$, $^3n\pi^*$). From the potential-energy surfaces, reaction barriers for the excited-state pathways could be estimated. The lowest barrier was found for the $^1A'$ state, which is only 0.2 eV. Additionally, linearly interpolated scans connecting the Franck-Condon region with biradicals were constructed and the topography of the potential-energy surfaces of higher-lying excited states was investigated. Analyzing the energies of the Hartree-Fock orbitals along the linearly interpolated reaction pathways showed that already small OH bond elongations (on the order of about 0.2 Å) lead to a substantial increase of the energy of the highest orbitals of water. When the HOMO of water is above the HOMO of triazine, there is a driving force for a hole transfer from triazine to water. An electron of water may fill the photogenerated hole in the HOMO of triazine, which

induces a subsequent proton transfer. This simple orbital picture is consistent with the computed potential-energy surfaces of the excited state electron-driven proton-transfer.

The photoinduced H-atom detachment reaction from the triaziny radical has been studied using the ADC(2) and CASSCF/CASPT2 methods. Like in the cases of pyrrole,^{187, 188} indole,¹⁸⁹ aniline¹⁹⁰ or phenol,¹⁹¹ a $\pi\sigma^*$ state provides a reaction channel for ultrafast non-statistical detachment of the H-atom after photoexcitation.

Overall, it has been shown that triazine in an aqueous environment can split water into an H-atom and a hydroxyl radical by the sequential absorption of two photons. This work represents a rather complete investigation of the biphotonic water-splitting mechanism in a chromophore-H₂O complex. It serves as reference study for the assessment of the accuracy of the electronic structure methods which have been used in this work for exploration of excited-state H-atom transfer reactions.

Individual contributions of the candidate:

Together with my supervisor Wolfgang Domcke, I designed the research. I performed all electronic-structure calculations (optimizations and single point calculations), except the scans along the linearly interpolated reaction paths, which have been calculated by Mikołaj J. Janicki. Together with him, I tested several electronic-structure methods with respect to their ability to appropriately describe the H-atom detachment reaction. I prepared the figures, analysed and interpreted the data and wrote the manuscript together with Wolfgang Domcke. As corresponding author, I submitted the manuscript took care of the correspondence with the editor and replied to the referees' comments.

3.2 Mechanism of Photocatalytic Water Splitting with Graphitic Carbon Nitride: Photochemistry of the Heptazine-Water Complex

Summary of “*Mechanism of Photocatalytic Water Splitting with Graphitic Carbon Nitride: Photochemistry of the Heptazine-Water Complex*” by Johannes Ehrmaier, Tolga N. V. Karsili, Andrzej L. Sobolewski, and Wolfgang Domcke; *J. Phys. Chem A*, **2018**, *121*, 25

Graphitic carbon-nitride materials consisting of heptazine building blocks have recently attracted vast interest, as they are photostable, consist of earth abundant materials, are non-toxic, easy to synthesize and can split water under visible light. In this publication, we explored the biphotonic water-splitting mechanism in the hydrogen-bonded heptazine-water complex. This complex can be considered as the simplest model system for carbon-nitride materials in aqueous solution. The vertical excitation energies of the hydrogen-bonded heptazine-water complex were calculated at the ADC(2) level and relaxed reaction paths for the H-atom transfer reaction involving the lowest ${}^1\pi\pi^*$ charge-transfer state were constructed. A two-dimensional relaxed potential-energy surface of the lowest singlet excited state was constructed, which reveals the barrier between the Franck-Condon region and the biradical. The barrier is about 0.75 eV. Moreover, a linearly interpolated scan was constructed to characterize the energy profiles of higher-lying excited states. The photoinduced H-atom detachment reaction from the heptazinyl radical was considered and a dissociation threshold energy of about 2.0 eV was determined. The excess H-atom can thus be detached by an ultrafast photo-triggered dissociation reaction.

Individual contributions of the author:

I initiated the idea to investigate the biphotonic water-splitting mechanism for the heptazine-water complex, which represents a model system for water splitting with carbon nitride materials. I performed the electronic-structure calculations, analysed the data and prepared the figures for the manuscript.

3.3 Mechanism of Photocatalytic Water Oxidation by Graphitic Carbon Nitride

Summary of “*Mechanism of Photocatalytic Water Oxidation by Graphitic Carbon Nitride*” by Johannes Ehrmaier, Wolfgang Domcke, and Daniel Opalka; *J. Phys. Chem. Lett.*, **2018**, *9*, 4695-4699

Photocatalytic water-splitting takes place in aqueous environments. Our previous theoretical studies focussed on the basic photochemical reactions in complexes of chromophores with one or a few water molecules. In this study, in contrast, the photochemistry of a heptazine molecule which is solvated in 120 surrounding water molecules was investigated. The environment is explicitly taken into account at the DFT level. In particular, the water molecules are treated at the same level of theory as the heptazine molecule to simulate the fluctuations of the aqueous environment without artefacts. Periodic boundary conditions are applied and the calculations were performed with the DFT and TDDFT methods, using the PBE functional. The system was equilibrated and propagated for 10 ps. At selected time steps, the absorption spectrum, the band structure and the projected density of states were evaluated and finally averaged to simulate environmental effects. Small distortions of the geometry of heptazine in solution break the symmetry and allow the transition to the S_1 state to obtain weak oscillator strength, which explains the faint onset of the experimental absorption spectrum at 2.6 eV. Photoabsorption of the solvated heptazine system creates a hole in the HOMO of heptazine. The H-atom transfer reaction from the water environment to the chromophore was investigated along an averaged reaction coordinate. Along this reaction coordinate, the energy of the HOMO of the hydrogen bonded water molecule rises, as has been shown before for the triazine-water complex. This provides the driving force for an electron transfer from water to heptazine, filling the hole in the HOMO of heptazine. The electron transfer in turn drives the proton transfer from water to heptazine. In summary, this study explains the onset of the absorption spectrum of heptazine in aqueous solution and confirms that the results, which

have been obtained for the hydrogen-bonded heptazine-water complex, are qualitatively representative for a bulk aqueous environment.

Individual contributions of the candidate:

Together with Daniel Opalka, I conceived the research and successfully applied for computational time at the Leibniz Supercomputing Center. During the project I took care of the correspondence with the supercomputing center and prepared all necessary reports. After developing the simulation protocol with Daniel Opalka, I performed all test calculations and the production runs. Finally, I analysed the data, produced the figures, interpreted the results and wrote the manuscript together with Daniel Opalka.

3.4 Role of the Pyridinyl Radical in the Light-Driven Reduction of Carbon Dioxide: A First-Principles Study

Summary of “*Role of the pyridinyl radical in the light-driven reduction of carbon dioxide: A first-principles study*” by Johannes Ehrmaier, Andrzej L. Sobolewski and Wolfgang Domcke; *J. Phys. Chem. A*, **2019**, *123*, 3678-3684

In this work, the photoinduced H-atom transfer reaction in the hydrogen-bonded pyridinyl-CO₂ complex, resulting in the reduction of CO₂ to the OCOH radical, was studied. Vertical excitation energies and orbitals were computed and analysed. The diffuse σ^* orbital of the pyridinyl radical was found to be localized on the CO₂ molecule. The $\pi\sigma^*$ state therefore is a charge-transfer state, in which electronic charge from the pyridinyl radical is transferred to the CO₂ molecule, forming the complex of a pyridinium cation and a CO₂ anion. A two-dimensional relaxed potential-energy surface of the $\pi\sigma^*$ state has been constructed at the UADC(2) level, showing a barrierfree reaction path for the H-atom transfer reaction. The potential-energy profile of the lowest $\pi\sigma^*$ state crosses the potential-energy curves of the lowest $\pi\pi^*$ state and the ground state. The dynamics at these conical intersections is decisive for the branching ratios of the reaction. The two-dimensional $\pi\sigma^*$ potential-energy surface has also been also calculated at the UMP2 and CASSCF/CASPT2 levels. All methods predict qualitatively similar potential-energy surfaces for the reaction. These benchmark calculations serve as reference for future calculations on larger systems, e.g. the heptazinyl-CO₂ complex. The role of the pyridinyl radical for the CO₂ reduction reaction has been extensively and controversially discussed in the literature, considering, however, only the ground-state reaction. With this study we suggest a novel excited-state mechanism for the reduction reaction of CO₂ by pyridinyl radicals. This mechanism is consistent with the experimental observations.

Individual contributions of the candidate:

With Wolfgang Domcke I conceived the research. I performed the electronic-structure calculations and explored the reaction coordinates and the electronic-structure methods. I analysed the data, performed the benchmark calculations, designed the figures and wrote the initial version of the manuscript.

4 Discussion and Summary

In 2007, Schnick and coworkers investigated the molecular structures of carbon-nitride materials and found that graphitic carbon-nitride materials are two-dimensional frameworks of one-dimensional chains of heptazine units.³⁸ This material is better described as a polymer than a two-dimensional crystalline material. Later on, Merschjann et al. investigated the luminescence of heptazine polymers and pointed out that the polymers behave like monomers in their luminescence properties.¹⁹² It was also found that an amorphous carbon-nitride material had a higher photocatalytic hydrogen evolution rate than a crystalline one, which is contrary to expectation in the picture based on semiconducting materials.¹⁹³ Moreover, small carbon-nitride oligomers, specifically heptazine dimers and trimers, perform as well as polymers for hydrogen evolution, revealing that long-range charge separation is not the limiting factor. Nor is absorption a decisive factor, as the polymers of this experiment were stronger absorbers of visible light than the small oligomers.¹⁹⁴ Large exciton binding energies of the order of electron volts render electron hole separation unfavorable^{62, 195, 196} and reorganization energies of polarons are also substantial.^{197, 198} Together, large exciton dissociation energies and large polaron stabilization energies may reduce the oxidation potential of holes below the threshold for water oxidation if the electron-hole pair is generated by a visible photon. These findings suggest that an alternative description of the photocatalytic water-splitting reaction with carbon-nitrides may be appropriate.

Moreover, there are several experimental results which strongly support that carbon nitrides oxidize water according to the biphotonic mechanism described herein. Hydroxyl radical generation by irradiated carbon-nitride materials in pure water has been reported in several studies. These radicals are not expected to be formed in the photoelectrochemical scenario, but are predicted by the biphotonic water-splitting cycle. Photogenerated OH radicals have been detected by EPR measurements using DMPO as spin trap,^{199, 200} or with organic

OH-radical scavengers, e.g. terephthalic acid, which is converted to fluorescent 2-hydroxyterephthalic acid by OH radicals.^{201, 202}

In 2018, the group of Schlenker at the University of Washington synthesized a substituted heptazine molecule, tri-anisole-heptazine (TAHz), and investigated its spectroscopy and photoreactivity.²⁰³ In toluene, an exceptionally long lifetime of the S_1 state of almost 300 ns has been observed. In contrast, the fluorescence was substantially quenched in water due to a proton-coupled electron-transfer reaction from water to TAHz. An H/D kinetic isotope effect of 2.9 was reported in H_2O/D_2O , confirming the H-atom transfer reaction from water to TAHz.²⁰³ The H-atom transfer reaction produces hydroxyl radicals, which have been detected using terephthalic acid as OH radical scavenger. It is worth to mention it has unequivocally been shown in these experiments that a heptazine-based molecule can oxidize water. This proves that long-range charge separation processes are not necessarily involved in the water-splitting reaction with carbon nitrides, nor is it necessary to replace water by sacrificial electron donors.

The combination of our theoretical studies on heptazine-water complexes with the recent experimental results for TAHz in aqueous solution provides insight into the mechanistic details of the water oxidation reaction. After photoexcitation to the second $^1\pi\pi^*$ state, the chromophore relaxes to the S_1 state according to Kasha's rule. The long lifetime of the S_1 state allows the H-atom to tunnel through the barrier separating the Franck-Condon region of the S_1 state from the biradical. The decisive molecular property which controls the efficiency of the water-splitting reaction is the height of the barrier for the proton-coupled electron-transfer reaction from water to the chromophore. As will be shown in future work, this barrier may be tuned by substitution of the heptazine chromophore. The mechanistic insights of the present work provide the basis for a systematic search for highly efficient water-splitting photocatalysts.

The mechanism of CO_2 reduction in the pyridinyl- CO_2 complex proposed herein is a new concept for the CO_2 reduction reaction with carbon nitride materials. From the investigations of the H-atom detachment reactions from

pyridine, triazine and heptazine, we can infer that the mechanism revealed for the pyridinyl-CO₂ complex can be transferred to the hydrogen-bonded triazinyl-CO₂ and heptazinyl-CO₂ complexes. These findings provide the basis for a new scenario of integrated water oxidation and carbon dioxide reduction with visible light. The so obtained OCOH radical can be further reduced to methanol by subsequent H-atom transfer reactions from hydrogenated chromophores, as found by Bocarsly and coworkers.¹⁰⁴ Since the first H-atom transfer reaction, creating the OCOH radical, is the rate-determining step, the following steps are not investigated in this work.

Future work should focus on first-principles studies of the dynamics of the reactions to obtain further mechanistic insights. Pang et al. have shown in a preliminary nonadiabatic trajectory surface-hopping simulation of the photoinduced dynamics of pyridine-water complexes with up to four water molecules that H-atom transfer reactions occur in these systems with a low quantum yield. Different reaction channels have been identified²⁰⁴ and it has been shown that the quantum yield for water oxidation increases with the size of the water complex.^{204, 205} It is straightforward, although computationally highly demanding, to apply this simulation protocol to the H-atom transfer reaction in heptazine-water and triazine-water complexes. The dynamics at the conical intersections along the H-atom transfer reaction path from hydrogenated chromophores to CO₂ also has to be examined in detail with trajectory surface-hopping simulations.

Finally, novel descriptors, in particular the barrier for the H-atom transfer reaction from water to the chromophore on the S₁ potential-energy surface, have been identified in the present work. These descriptors can be used for extensive computational screening studies to identify the best materials for the water oxidation and CO₂ reduction reactions. Because precise reaction mechanisms and mechanistically relevant descriptors were lacking so far, the development of improved carbon nitride photocatalysts has been based on experimental trial-and-error studies.²⁰⁶ Computational screening studies based on detailed mechanistic insights could lead to a dramatic acceleration of progress in H₂O oxidation and CO₂ reduction photocatalysis.

In summary, this work provides a blueprint for a novel scenario of artificial photosynthesis with carbon-nitride catalysts. Fig. 4 illustrates schematically the photocatalytic cycle of artificial photosynthesis with carbon nitrides. With the first photon, an H-atom is transferred from a hydrogen-bonded water molecule to the chromophore, creating the hydrogenated chromophore and an OH radical. With the second photon, the excess H-atom is transferred from the hydrogenated chromophore to a hydrogen-bonded CO₂ molecule. Overall the energy of two photons is used to transfer an H-atom from water to CO₂. The hydrogenated chromophore, which is formed in the first step, plays a key role in the cycle. It is a long-lived stable intermediate that stores the energy of the first photon until a second photon completes the reaction. The carbon-nitride molecule serves as chromophore, H-atom shuttle and catalyst, which allows a one-pot reaction design for water oxidation and CO₂ reduction with a single photoreactive material.

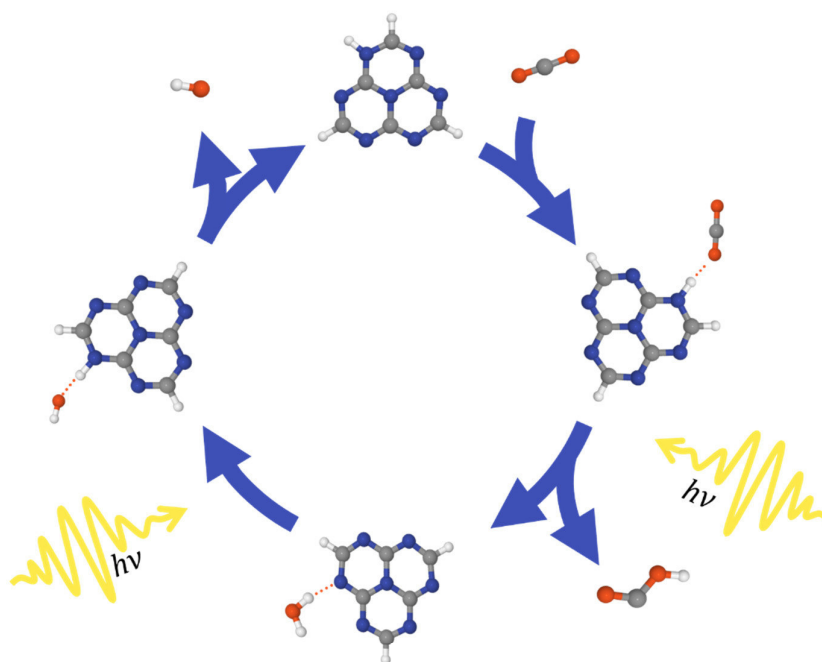


Fig. 4: Scheme for the artificial photosynthesis cycle with the heptazine chromophore, yielding the HOCO radical from H₂O, CO₂ and light. With the first photon, an H-atom is transferred from water to the chromophore, generating a hydroxyl radical and the hydrogenated chromophore. With the second photon, a hydrogen atom is transferred from the reduced chromophore to a hydrogen-bonded CO₂ molecule, generating the HOCO radical.

Bibliography

- (1) I. E. Agency, Global Energy & CO2 Status Report. 2018.
- (2) Pieter Tans, NOAA/ESRL (www.esrl.noaa.gov/gmd/ccgg/trends/) and Ralph Keeling, Scripps Institution of Oceanography (scrippsco2.ucsd.edu/) (accessed April 3rd, 2019).
- (3) A. Fujishima; K. Honda, Electrochemical Photolysis of Water at a Semiconductor Electrode. *Nature* **1972**, *238*, 37-38.
- (4) Y. Tachibana; L. Vayssieres; J. R. Durrant, Artificial photosynthesis for solar water-splitting. *Nat. Photonics* **2012**, *6*, 511.
- (5) R. Singh; S. Dutta, A review on H2 production through photocatalytic reactions using TiO2/TiO2-assisted catalysts. *Fuel* **2018**, *220*, 607-620.
- (6) M. Ge; J. Cai; J. Iocozzia; C. Cao; J. Huang; X. Zhang; J. Shen; S. Wang; S. Zhang; K.-Q. Zhang, A review of TiO2 nanostructured catalysts for sustainable H2 generation. *Int. J. Hydrogen Energy* **2017**, *42*, 8418-8449.
- (7) J. Low; B. Cheng; J. Yu, Surface modification and enhanced photocatalytic CO2 reduction performance of TiO2: a review. *Appl. Surf. Sci.* **2017**, *392*, 658-686.
- (8) M. Ni; M. K. Leung; D. Y. Leung; K. Sumathy, A review and recent developments in photocatalytic water-splitting using TiO2 for hydrogen production. *Renewable Sustainable Energy Rev.* **2007**, *11*, 401-425.
- (9) M. Ashokkumar, An overview on semiconductor particulate systems for photoproduction of hydrogen. *Int. J. Hydrogen Energy* **1998**, *23*, 427-438.
- (10) A. Fujishima; T. N. Rao; D. A. Tryk, Titanium dioxide photocatalysis. *J. Photochem. Photobiol., C* **2000**, *1*, 1-21.
- (11) S. W. Gersten; G. J. Samuels; T. J. Meyer, Catalytic oxidation of water by an oxo-bridged ruthenium dimer. *J. Am. Chem. Soc.* **1982**, *104*, 4029-4030.
- (12) K. A. Grice, Carbon dioxide reduction with homogenous early transition metal complexes: Opportunities and challenges for developing CO2 catalysis. *Coord. Chem. Rev.* **2017**, *336*, 78-95.

- (13) H. Takeda; O. Ishitani, Development of efficient photocatalytic systems for CO₂ reduction using mononuclear and multinuclear metal complexes based on mechanistic studies. *Coord. Chem. Rev.* **2010**, *254*, 346-354.
- (14) B. Kumar; M. Llorente; J. Froehlich; T. Dang; A. Sathrum; C. P. Kubiak, Photochemical and Photoelectrochemical Reduction of CO₂. *Annu. Rev. Phys. Chem.* **2012**, *63*, 541-569.
- (15) A. J. Morris; G. J. Meyer; E. Fujita, Molecular Approaches to the Photocatalytic Reduction of Carbon Dioxide for Solar Fuels. *Acc. Chem. Res.* **2009**, *42*, 1983-1994.
- (16) J. D. Blakemore; R. H. Crabtree; G. W. Brudvig, Molecular Catalysts for Water Oxidation. *Chem. Rev.* **2015**, *115*, 12974-13005.
- (17) M. Yagi; M. Kaneko, Molecular Catalysts for Water Oxidation. *Chem. Rev.* **2001**, *101*, 21-36.
- (18) J. K. McCusker, Electronic structure in the transition metal block and its implications for light harvesting. *Science* **2019**, *363*, 484-488.
- (19) W. Iqbal; B. Yang; X. Zhao; M. Rauf; M. Waqas; Y. Gong; J. Zhang; Y. Mao; Technology, Controllable synthesis of graphitic carbon nitride nanomaterials for solar energy conversion and environmental remediation: the road travelled and the way forward. *Catal. Sci. Technol.* **2018**, *8*, 4576-4599.
- (20) W.-J. Ong; L.-L. Tan; Y. H. Ng; S.-T. Yong; S.-P. Chai, Graphitic carbon nitride (g-C₃N₄)-based photocatalysts for artificial photosynthesis and environmental remediation: are we a step closer to achieving sustainability? *Chem. Rev.* **2016**, *116*, 7159-7329.
- (21) J. Liebig, Über einige Stickstoff-Verbindungen. *J. Ann. Pharm.* **1834**, *10*, 1-47.
- (22) T. Shibata; A. Kabumoto; T. Shiragami; O. Ishitani; C. Pac; S. Yanagida, Novel visible-light-driven photocatalyst. Poly (p-phenylene)-catalyzed photoreductions of water, carbonyl compounds, and olefins. *J. Phys. Chem.* **1990**, *94*, 2068-2076.
- (23) S. Matsuoka; T. Kohzuki; Y. Kuwana; A. Nakamura; S. Yanagida, Visible-light-induced photocatalysis of poly (pyridine-2, 5-diyl). Photoreduction of water, carbonyl compounds and alkenes with triethylamine. *J. Chem. Soc., Perkin Trans. 2* **1992**, 679-685.
- (24) X. Wang; K. Maeda; A. Thomas; K. Takanabe; G. Xin; J. M. Carlsson; K. Domen; M. Antonietti, A metal-free polymeric photocatalyst for hydrogen production from water under visible light. *Nature Mater.* **2009**, *8*, 76-80.

-
- (25) K. Schwinghammer; B. Tuffy; M. B. Mesch; E. Wirnhier; C. Martineau; F. Taulelle; W. Schnick; J. Senker; B. V. Lotsch, Triazine-based Carbon Nitrides for Visible-Light-Driven Hydrogen Evolution. *Angew. Chem. Int. Ed.* **2013**, *52*, 2435-2439.
- (26) K. Schwinghammer; M. B. Mesch; V. Duppel; C. Ziegler; J. r. Senker; B. V. Lotsch, Crystalline Carbon Nitride Nanosheets for Improved Visible-Light Hydrogen Evolution. *J. Am. Chem. Soc.* **2014**, *136*, 1730-1733.
- (27) J. Bi; W. Fang; L. Li; J. Wang; S. Liang; Y. He; M. Liu; L. Wu, Covalent Triazine-Based Frameworks as Visible Light Photocatalysts for the Splitting of Water. *Macromol. Rapid Commun.* **2015**, *36*, 1799-1805.
- (28) L. Lin; C. Wang; W. Ren; H. Ou; Y. Zhang; X. Wang, Photocatalytic overall water splitting by conjugated semiconductors with crystalline poly (triazine imide) frameworks. *Chem. Sci.* **2017**, *8*, 5506-5511.
- (29) M. J. Bojdys; J. Jeromenok; A. Thomas; M. Antonietti, Rational Extension of the Family of Layered, Covalent, Triazine-Based Frameworks with Regular Porosity. *Adv. Mater.* **2010**, *22*, 2202-2205.
- (30) P. Kuhn; M. Antonietti; A. Thomas, Porous, Covalent Triazine-Based Frameworks Prepared by Ionothermal Synthesis. *Angew. Chem. Int. Ed.* **2008**, *47*, 3450-3453.
- (31) S. Ren; M. J. Bojdys; R. Dawson; A. Laybourn; Y. Z. Khimyak; D. J. Adams; A. I. Cooper, Porous, Fluorescent, Covalent Triazine-Based Frameworks Via Room-Temperature and Microwave-Assisted Synthesis. *Adv. Mater.* **2012**, *24*, 2357-2361.
- (32) V. S. Vyas; F. Haase; L. Stegbauer; G. Savasci; F. Podjaski; C. Ochsenfeld; B. V. Lotsch, A tunable azine covalent organic framework platform for visible light-induced hydrogen generation. *Nat. Commun.* **2015**, *6*, 8508.
- (33) S. Kuecken; A. Acharjya; L. Zhi; M. Schwarze; R. Schomäcker; A. Thomas, Fast tuning of covalent triazine frameworks for photocatalytic hydrogen evolution. *Chem. Commun.* **2017**, *53*, 5854-5857.
- (34) C. B. Meier; R. S. Sprick; A. Monti; P. Guiglion; J.-S. M. Lee; M. A. Zwijnenburg; A. I. Cooper, Structure-property relationships for covalent triazine-based frameworks: The effect of spacer length on photocatalytic hydrogen evolution from water. *Polymer* **2017**, *126*, 283-290.
- (35) K. Schwinghammer; S. Hug; M. Mesch; J. Senker; B. V. Lotsch, Phenyl-triazine oligomers for light-driven hydrogen evolution. *Energy Environ. Sci.* **2015**, *8*, 3345-3353.

- (36) Y. Zheng; L. Lin; B. Wang; X. Wang, Graphitic Carbon Nitride Polymers toward Sustainable Photoredox Catalysis. *Angew. Chem. Int. Ed.* **2015**, *54*, 12868-12884.
- (37) S. Cao; J. Low; J. Yu; M. Jaroniec, Polymeric Photocatalysts Based on Graphitic Carbon Nitride. *Adv. Mater.* **2015**, *27*, 2150-2176.
- (38) B. V. Lotsch; M. Döblinger; J. Sehnert; L. Seyfarth; J. Senker; O. Oeckler; W. Schnick, Unmasking Melon by a Complementary Approach Employing Electron Diffraction, Solid-State NMR Spectroscopy, and Theoretical Calculations—Structural Characterization of a Carbon Nitride Polymer. *Chem. - Eur. J.* **2007**, *13*, 4969-4980.
- (39) L. Zhou; H. Zhang; H. Sun; S. Liu; M. O. Tade; S. Wang; W. Jin, Recent advances in non-metal modification of graphitic carbon nitride for photocatalysis: a historic review. *Catal. Sci. Technol.* **2016**, *6*, 7002-7023.
- (40) Z. Zhao; Y. Sun; F. Dong, Graphitic carbon nitride based nanocomposites: a review. *Nanoscale* **2015**, *7*, 15-37.
- (41) M. Mousavi; A. Habibi-Yangjeh; S. R. Pouran, Review on magnetically separable graphitic carbon nitride-based nanocomposites as promising visible-light-driven photocatalysts. *J. Mater. Sci.: Mater. Electron.* **2018**, *29*, 1719-1747.
- (42) Y. Wang; X. Wang; M. Antonietti, Polymeric Graphitic Carbon Nitride as a Heterogeneous Organocatalyst: From Photochemistry to Multipurpose Catalysis to Sustainable Chemistry. *Angew. Chem. Int. Ed.* **2012**, *51*, 68-89.
- (43) L. Jiang; X. Yuan; Y. Pan; J. Liang; G. Zeng; Z. Wu; H. Wang, Doping of graphitic carbon nitride for photocatalysis: A review. *Appl. Catal. B* **2017**, *217*, 388-406.
- (44) J. Zhu; P. Xiao; H. Li; S. A. Carabineiro, Graphitic Carbon Nitride: Synthesis, Properties, and Applications in Catalysis. *ACS Appl. Mater. Interfaces.* **2014**, *6*, 16449-16465.
- (45) Z. Lin; X. Wang, Nanostructure Engineering and Doping of Conjugated Carbon Nitride Semiconductors for Hydrogen Photosynthesis. *Angew. Chem. Int. Ed.* **2013**, *52*, 1735-1738.
- (46) X. Wang; S. Blechert; M. Antonietti, Polymeric Graphitic Carbon Nitride for Heterogeneous Photocatalysis. *ACS Catal.* **2012**, *2*, 1596-1606.
- (47) S. Chu; Y. Wang; Y. Guo; J. Feng; C. Wang; W. Luo; X. Fan; Z. Zou, Band Structure Engineering of Carbon Nitride: In Search of a Polymer Photocatalyst with High Photooxidation Property. *ACS Catal.* **2013**, *3*, 912-919.

-
- (48) D. J. Martin; K. Qiu; S. A. Shevlin; A. D. Handoko; X. Chen; Z. Guo; J. Tang, Highly Efficient Photocatalytic H₂ Evolution from Water using Visible Light and Structure-Controlled Graphitic Carbon Nitride. *Angew. Chem. Int. Ed.* **2014**, *53*, 9240-9245.
- (49) C. A. Caputo; M. A. Gross; V. W. Lau; C. Cavazza; B. V. Lotsch; E. Reisner, Photocatalytic Hydrogen Production using Polymeric Carbon Nitride with a Hydrogenase and a Bioinspired Synthetic Ni Catalyst. *Angew. Chem. Int. Ed.* **2014**, *53*, 11538-11542.
- (50) Y. Gong; M. Li; Y. Wang, Carbon Nitride in Energy Conversion and Storage: Recent Advances and Future Prospects. *ChemSusChem* **2015**, *8*, 931-946.
- (51) J. Liu; Y. Liu; N. Liu; Y. Han; X. Zhang; H. Huang; Y. Lifshitz; S.-T. Lee; J. Zhong; Z. Kang, Metal-free efficient photocatalyst for stable visible water splitting via a two-electron pathway. *Science* **2015**, *347*, 970-974.
- (52) G. Zhang; Z.-A. Lan; L. Lin; S. Lin; X. Wang, Overall water splitting by Pt/gC₃N₄ photocatalysts without using sacrificial agents. *Chem. Sci.* **2016**, *7*, 3062-3066.
- (53) J. Liu; N. Liu; H. Li; L. Wang; X. Wu; H. Huang; Y. Liu; F. Bao; Y. Lifshitz; S.-T. Lee, A critical study of the generality of the two step two electron pathway for water splitting by application of a C₃N₄/MnO₂ photocatalyst. *Nanoscale* **2016**, *8*, 11956-11961.
- (54) T. Botari; W. P. Huhn; V. W.-h. Lau; B. V. Lotsch; V. Blum, Thermodynamic equilibria in carbon nitride photocatalyst materials and conditions for the existence of graphitic carbon nitride g-C₃N₄. *Chem. Mater.* **2017**, *29*, 4445-4453.
- (55) S. T. A. G. Melissen; S. N. Steinmann; T. Le Bahers; P. Sautet, DFT Perspective on the Thermochemistry of Carbon Nitride Synthesis. *J. Phys. Chem. C* **2016**, *120*, 24542-24550.
- (56) M. Deifallah; P. F. McMillan; F. Corà, Electronic and Structural Properties of Two-Dimensional Carbon Nitride Graphenes. *J. Phys. Chem. C* **2008**, *112*, 5447-5453.
- (57) K. Srinivasu; B. Modak; S. K. Ghosh, Porous Graphitic Carbon Nitride: A Possible Metal-Free Photocatalyst for Water Splitting. *J. Phys. Chem. C* **2014**, *118*, 26479-26484.
- (58) F. Wu; Y. Liu; G. Yu; D. Shen; Y. Wang; E. Kan, Visible-Light-Absorption in Graphitic C₃N₄ Bilayer: Enhanced by Interlayer Coupling. *J. Phys. Chem. Lett.* **2012**, *3*, 3330-3334.
- (59) D. Liang; T. Jing; Y. Ma; J. Hao; G. Sun; M. Deng, Photocatalytic Properties of g-C₆N₆/g-C₃N₄ Heterostructure: A Theoretical Study. *J. Phys. Chem. C* **2016**, *120*, 24023-24029.

- (60) J. Feng; G. Liu; S. Yuan; Y. Ma, Influence of functional groups on water splitting in carbon nanodot and graphitic carbon nitride composites: a theoretical mechanism study. *Phys. Chem. Chem. Phys.* **2017**, *19*, 4997-5003.
- (61) K. Srinivasu; B. Modak; S. K. Ghosh, Improving the photocatalytic activity of s-triazine based graphitic carbon nitride through metal decoration: an ab initio investigation. *Phys. Chem. Chem. Phys.* **2016**, *18*, 26466-26474.
- (62) S. Melissen; T. Le Bahers; S. N. Steinmann; P. Sautet, Relationship between Carbon Nitride Structure and Exciton Binding Energies: A DFT Perspective. *J. Phys. Chem. C* **2015**, *119*, 25188-25196.
- (63) C. Butchosa; P. Guiglion; M. A. Zwijnenburg, Carbon Nitride Photocatalysts for Water Splitting: A Computational Perspective. *J. Phys. Chem. C* **2014**, *118*, 24833-24842.
- (64) C. Butchosa; T. O. McDonald; A. I. Cooper; D. J. Adams; M. A. Zwijnenburg, Shining a Light on s-Triazine-Based Polymers. *J. Phys. Chem. C* **2014**, *118*, 4314-4324.
- (65) G. Gao; Y. Jiao; F. Ma; Y. Jiao; E. Waclawik; A. Du, Metal-free graphitic carbon nitride as mechano-catalyst for hydrogen evolution reaction. *J. Catal.* **2015**, *332*, 149-155.
- (66) S. M. Aspera; M. David; H. Kasai, First-Principles Study of the Adsorption of Water on Tri-s-triazine-based Graphitic Carbon Nitride. *Jpn. J. Appl. Phys.* **2010**, *49*, 115703.
- (67) H.-Z. Wu; L.-M. Liu; S.-J. Zhao, The effect of water on the structural, electronic and photocatalytic properties of graphitic carbon nitride. *Phys. Chem. Chem. Phys.* **2014**, *16*, 3299-3304.
- (68) J. Wirth; R. Neumann; M. Antonietti; P. Saalfrank, Adsorption and photocatalytic splitting of water on graphitic carbon nitride: a combined first principles and semiempirical study. *Phys. Chem. Chem. Phys.* **2014**, *16*, 15917-15926.
- (69) X. Liu; A. L. Sobolewski; R. Borrelli; W. Domcke, Computational investigation of the photoinduced homolytic dissociation of water in the pyridine-water complex. *Phys. Chem. Chem. Phys.* **2013**, *15*, 5957-5966.
- (70) X. Liu; A. L. Sobolewski; W. Domcke, Photoinduced Oxidation of Water in the Pyridine-Water Complex: Comparison of the Singlet and Triplet Photochemistries. *J. Phys. Chem. A* **2014**, *118*, 7788-7795.
- (71) X. Liu; T. N. V. Karsili; A. L. Sobolewski; W. Domcke, Photocatalytic Water Splitting with the Acridine Chromophore: A Computational Study. *J. Phys. Chem. B* **2015**, *119*, 10664-10672.

-
- (72) X. Liu; T. N. V. Karsili; A. L. Sobolewski; W. Domcke, Photocatalytic water splitting with acridine dyes: Guidelines from computational chemistry. *Chem. Phys.* **2016**, *464*, 78-85.
- (73) T. N. V. Karsili; D. Tuna; J. Ehrmaier; W. Domcke, Photoinduced water splitting via benzoquinone and semiquinone sensitisation. *Phys. Chem. Chem. Phys.* **2015**, *17*, 32183-32193.
- (74) N. Esteves-López; S. Coussan; C. Dedonder-Lardeux; C. Juvet, Photoinduced water splitting in pyridine water clusters. *Phys. Chem. Chem. Phys.* **2016**, *18*, 25637-25644.
- (75) M. D. Porosoff; B. Yan; J. G. Chen, Catalytic reduction of CO₂ by H₂ for synthesis of CO, methanol and hydrocarbons: challenges and opportunities. *Energy Environ. Sci.* **2016**, *9*, 62-73.
- (76) P. Kaiser; R. B. Unde; C. Kern; A. Jess, Production of Liquid Hydrocarbons with CO₂ as Carbon Source Based on Reverse Water-Gas Shift and Fischer-Tropsch Synthesis. *Chem. Ing. Tech.* **2013**, *85*, 489-499.
- (77) E. T. Kho; T. H. Tan; E. Lovell; R. J. Wong; J. Scott; R. Amal, A review on photo-thermal catalytic conversion of carbon dioxide. *Green Energy & Environment* **2017**, *2*, 204-217.
- (78) K. Sordakis; C. Tang; L. K. Vogt; H. Junge; P. J. Dyson; M. Beller; G. Laurencyzy, Homogeneous Catalysis for Sustainable Hydrogen Storage in Formic Acid and Alcohols. *Chem. Rev.* **2017**, *118*, 372-433.
- (79) W. Li; H. Wang; X. Jiang; J. Zhu; Z. Liu; X. Guo; C. Song, A short review of recent advances in CO₂ hydrogenation to hydrocarbons over heterogeneous catalysts. *RSC Adv.* **2018**, *8*, 7651-7669.
- (80) J. Artz; T. E. Müller; K. Thenert; J. Kleinekorte; R. Meys; A. Sternberg; A. Bardow; W. Leitner, Sustainable Conversion of Carbon Dioxide: An Integrated Review of Catalysis and Life Cycle Assessment. *Chem. Rev.* **2017**, *118*, 434-504.
- (81) B. Hu; C. Guild; S. L. Suib, Thermal, electrochemical, and photochemical conversion of CO₂ to fuels and value-added products. *J. CO₂ Util.* **2013**, *1*, 18-27.
- (82) S. Rönisch; J. Schneider; S. Matthischke; M. Schlüter; M. Götz; J. Lefebvre; P. Prabhakaran; S. Bajohr, Review on methanation – From fundamentals to current projects. *Fuel* **2016**, *166*, 276-296.

- (83) M. Younas; L. Loong Kong; M. J. K. Bashir; H. Nadeem; A. Shehzad; S. Sethupathi, Recent Advancements, Fundamental Challenges, and Opportunities in Catalytic Methanation of CO₂. *Energy Fuels* **2016**, *30*, 8815-8831.
- (84) D. T. Whipple; P. J. A. Kenis, Prospects of CO₂ Utilization via Direct Heterogeneous Electrochemical Reduction. *J. Phys. Chem. Lett.* **2010**, *1*, 3451-3458.
- (85) B. Khezri; A. C. Fisher; M. Pumera, CO₂ reduction: the quest for electrocatalytic materials. *J. Mater. Chem. A* **2017**, *5*, 8230-8246.
- (86) Z. Sun; T. Ma; H. Tao; Q. Fan; B. Han, Fundamentals and Challenges of Electrochemical CO₂ Reduction Using Two-Dimensional Materials. *Chem* **2017**, *3*, 560-587.
- (87) C. Costentin; M. Robert; J.-M. Savéant, Catalysis of the electrochemical reduction of carbon dioxide. *Chem. Soc. Rev.* **2013**, *42*, 2423-2436.
- (88) M. Gattrell; N. Gupta; A. Co, A review of the aqueous electrochemical reduction of CO₂ to hydrocarbons at copper. *J. Electroanal. Chem.* **2006**, *594*, 1-19.
- (89) J. Zhao; X. Wang; Z. Xu; J. S. Loo, Hybrid catalysts for photoelectrochemical reduction of carbon dioxide: a prospective review on semiconductor/metal complex co-catalyst systems. *J. Mater. Chem. A* **2014**, *2*, 15228-15233.
- (90) F. Goettmann; A. Thomas; M. Antonietti, Metal-Free Activation of CO₂ by Mesoporous Graphitic Carbon Nitride. *Angew. Chem. Int. Ed.* **2007**, *46*, 2717-2720.
- (91) G. Dong; L. Zhang, Porous structure dependent photoreactivity of graphitic carbon nitride under visible light. *J. Mater. Chem.* **2012**, *22*, 1160-1166.
- (92) J. Yu; K. Wang; W. Xiao; B. Cheng, Photocatalytic reduction of CO₂ into hydrocarbon solar fuels over gC₃N₄-Pt nanocomposite photocatalysts. *Phys. Chem. Chem. Phys.* **2014**, *16*, 11492-11501.
- (93) K. Wang; Q. Li; B. Liu; B. Cheng; W. Ho; J. Yu, Sulfur-doped g-C₃N₄ with enhanced photocatalytic CO₂-reduction performance. *App. Catal. B* **2015**, *176*, 44-52.
- (94) W.-J. Ong; L.-L. Tan; S.-P. Chai; S.-T. Yong, Heterojunction engineering of graphitic carbon nitride (gC₃N₄) via Pt loading with improved daylight-induced photocatalytic reduction of carbon dioxide to methane. *Dalton Trans.* **2015**, *44*, 1249-1257.
- (95) W.-J. Ong; L.-L. Tan; S.-P. Chai; S.-T. Yong; A. R. Mohamed, Surface charge modification via protonation of graphitic carbon nitride (g-C₃N₄) for electrostatic self-assembly construction of 2D/2D reduced graphene oxide (rGO)/g-C₃N₄ nanostructures

toward enhanced photocatalytic reduction of carbon dioxide to methane. *Nano Energy* **2015**, *13*, 757-770.

(96) J. Lin; Z. Pan; X. Wang, Photochemical reduction of CO₂ by graphitic carbon nitride polymers. *ACS Sustainable Chem. Eng.* **2014**, *2*, 353-358.

(97) S. Wang; J. Lin; X. Wang, Semiconductor–redox catalysis promoted by metal–organic frameworks for CO₂ reduction. *Phys. Chem. Chem. Phys.* **2014**, *16*, 14656-14660.

(98) Y. He; Y. Wang; L. Zhang; B. Teng; M. Fan, High-efficiency conversion of CO₂ to fuel over ZnO/g-C₃N₄ photocatalyst. *Appl. Catal., B* **2015**, *168*, 1-8.

(99) S.-W. Cao; X.-F. Liu; Y.-P. Yuan; Z.-Y. Zhang; Y.-S. Liao; J. Fang; S. C. J. Loo; T. C. Sum; C. Xue, Solar-to-fuels conversion over In₂O₃/g-C₃N₄ hybrid photocatalysts. *Appl. Catal., B* **2014**, *147*, 940-946.

(100) J. Qin; S. Wang; H. Ren; Y. Hou; X. Wang, Photocatalytic reduction of CO₂ by graphitic carbon nitride polymers derived from urea and barbituric acid. *Appl. Catal., B* **2015**, *179*, 1-8.

(101) W. Tu; Y. Xu; J. Wang; B. Zhang; T. Zhou; S. Yin; S. Wu; C. Li; Y. Huang; Y. Zhou, Investigating the Role of Tunable Nitrogen Vacancies in Graphitic Carbon Nitride Nanosheets for Efficient Visible-Light-Driven H₂ Evolution and CO₂ Reduction. *ACS Sustainable Chem. Eng.* **2017**, *5*, 7260-7268.

(102) E. E. Barton; D. M. Rampulla; A. B. Bocarsly, Selective Solar-Driven Reduction of CO₂ to Methanol Using a Catalyzed p-GaP Based Photoelectrochemical Cell. *J. Am. Chem. Soc.* **2008**, *130*, 6342-6344.

(103) G. Seshadri; C. Lin; A. B. Bocarsly, A new homogeneous electrocatalyst for the reduction of carbon dioxide to methanol at low overpotential. *J. Electroanal. Chem.* **1994**, *372*, 145-150.

(104) E. B. Cole; P. S. Lakkaraju; D. M. Rampulla; A. J. Morris; E. Abelev; A. B. Bocarsly, Using a One-Electron Shuttle for the Multielectron Reduction of CO₂ to Methanol: Kinetic, Mechanistic, and Structural Insights. *J. Am. Chem. Soc.* **2010**, *132*, 11539-11551.

(105) A. J. Morris; R. T. McGibbon; A. B. Bocarsly, Electrocatalytic Carbon Dioxide Activation: The Rate-Determining Step of Pyridinium-Catalyzed CO₂ Reduction. *ChemSusChem* **2011**, *4*, 191-196.

- (106) K. A. Keets; E. B. Cole; A. J. Morris; N. Sivasankar; K. Teamey; P. S. Lakkaraju; A. B. Bocarsly, Analysis of pyridinium catalyzed electrochemical and photoelectrochemical reduction of CO₂: Chemistry and economic impact. *Indian J. Chem.* **2012**, *51A*, 1284-1297.
- (107) Y. Yan; E. L. Zeitler; J. Gu; Y. Hu; A. B. Bocarsly, Electrochemistry of Aqueous Pyridinium: Exploration of a Key Aspect of Electrocatalytic Reduction of CO₂ to Methanol. *J. Am. Chem. Soc.* **2013**, *135*, 14020-14023.
- (108) Y. Yan; J. Gu; A. B. Bocarsly, Hydrogen Bonded Pyridine Dimer: A Possible Intermediate in the Electrocatalytic Reduction of Carbon Dioxide to Methanol. *Aerosol Air Qual. Res.* **2014**, *14*, 515-521.
- (109) J. White; M. Baruch; J. Pander; Y. Hu; I. Fortmeyer; J. Park; T. Zhang; K. Liao; J. Gu; Y. Yan; T. W. Shaw; E. Abelev; A. B. Bocarsly, Light-Driven Heterogeneous Reduction of Carbon Dioxide: Photocatalysts and Photoelectrodes. *Chem. Rev.* **2015**, *115*, 12888-12935.
- (110) F. Riboni; E. Selli; M. Hoffmann; A. Colussi, Homogeneous Reduction of CO₂ by Photogenerated Pyridinyl Radicals. *J. Phys. Chem. A* **2015**, *119*, 4433-4438.
- (111) J. A. Keith; E. A. Carter, Theoretical Insights into Pyridinium-Based Photoelectrocatalytic Reduction of CO₂. *J. Am. Chem. Soc.* **2012**, *134*, 7580-7583.
- (112) J. A. Keith; E. A. Carter, Electrochemical reactivities of pyridinium in solution: consequences for CO₂ reduction mechanisms. *Chem. Sci.* **2013**, *4*, 1490-1496.
- (113) A. B. Muñoz-García; E. A. Carter, Non-Innocent Dissociation of H₂O on GaP(110): Implications for Electrochemical Reduction of CO₂. *J. Am. Chem. Soc.* **2012**, *134*, 13600-13603.
- (114) J. A. Keith; A. B. Muñoz-García; M. Lessio; E. A. Carter, Cluster Models for Studying CO₂ Reduction on Semiconductor Photoelectrodes. *Top. Catal.* **2015**, *58*, 46-56.
- (115) M. Lessio; E. A. Carter, What Is the Role of Pyridinium in Pyridine-Catalyzed CO₂ Reduction on p-GaP Photocathodes? *J. Am. Chem. Soc.* **2015**, *137*, 13248-13251.
- (116) T. P. Senftle; M. Lessio; E. A. Carter, Interaction of Pyridine and Water with the Reconstructed Surfaces of GaP(111) and CdTe(111) Photoelectrodes: Implications for CO₂ Reduction. *Chem. Mater.* **2016**, *28*, 5799-5810.
- (117) M. Lessio; C. Riplinger; E. A. Carter, Stability of surface protons in pyridine-catalyzed CO₂ reduction at p-GaP photoelectrodes. *Phys. Chem. Chem. Phys.* **2016**, *18*, 26434-26443.

-
- (118) M. Lessio; T. P. Senftle; E. A. Carter, Is the Surface Playing a Role during Pyridine-Catalyzed CO₂ Reduction on p-GaP Photoelectrodes? *ACS Energy Lett.* **2016**, *1*, 464-468.
- (119) T. P. Senftle; M. Lessio; E. A. Carter, The Role of Surface-Bound Dihydropyridine Analogues in Pyridine-Catalyzed CO₂ Reduction over Semiconductor Photoelectrodes. *ACS Cent. Sci.* **2017**, *3*, 968-974.
- (120) M. Lessio; J. M. Dieterich; E. A. Carter, Hydride Transfer at the GaP(110)/Solution Interface: Mechanistic Implications for CO₂ Reduction Catalyzed by Pyridine. *J. Phys. Chem. C* **2017**, *121*, 17321-17331.
- (121) S. Xu; L. Li; E. A. Carter, Why and How Carbon Dioxide Conversion to Methanol Happens on Functionalized Semiconductor Photoelectrodes. *J. Am. Chem. Soc.* **2018**, *140*, 16749-16757.
- (122) C.-H. Lim; A. M. Holder; C. B. Musgrave, Mechanism of Homogeneous Reduction of CO₂ by Pyridine: Proton Relay in Aqueous Solvent and Aromatic Stabilization. *J. Am. Chem. Soc.* **2013**, *135*, 142-154.
- (123) P. Puthiaraj; Y.-R. Lee; S. Zhang; W.-S. Ahn, Triazine-based covalent organic polymers: design, synthesis and applications in heterogeneous catalysis. *J. Mater. Chem. A* **2016**, *4*, 16288-16311.
- (124) P. Pulay, Localizability of dynamic electron correlation. *Chem. Phys. Lett.* **1983**, *100*, 151-154.
- (125) S. Sæbø; P. Pulay, Local configuration interaction: An efficient approach for larger molecules. *Chem. Phys. Lett.* **1985**, *113*, 13-18.
- (126) P. Pulay; S. Sæbø, Orbital-invariant formulation and second-order gradient evaluation in Møller-Plesset perturbation theory. *Theor. Chim. Acta* **1986**, *69*, 357-368.
- (127) M. Feyereisen; G. Fitzgerald; A. Komornicki, Use of approximate integrals in ab initio theory. An application in MP2 energy calculations. *Chem. Phys. Lett.* **1993**, *208*, 359-363.
- (128) F. Weigend; M. Häser; H. Patzelt; R. Ahlrichs, RI-MP2: optimized auxiliary basis sets and demonstration of efficiency. *Chem. Phys. Lett.* **1998**, *294*, 143-152.
- (129) H.-J. Werner; F. R. Manby; P. J. Knowles, Fast linear scaling second-order Møller-Plesset perturbation theory (MP2) using local and density fitting approximations. *J. Chem. Phys.* **2003**, *118*, 8149-8160.

- (130) S. A. Maurer; D. S. Lambrecht; J. Kussmann; C. Ochsenfeld, Efficient distance-including integral screening in linear-scaling Møller-Plesset perturbation theory. *J. Chem. Phys.* **2013**, *138*, 014101.
- (131) D. Danovich, Green's function methods for calculating ionization potentials, electron affinities, and excitation energies. *WIREs: Comput. Mol. Sci.* **2011**, *1*, 377-387.
- (132) P. H. Harbach; M. Wormit; A. Dreuw, The third-order algebraic diagrammatic construction method (ADC(3)) for the polarization propagator for closed-shell molecules: Efficient implementation and benchmarking. *J. Chem. Phys.* **2014**, *141*, 064113.
- (133) C. Hättig, Structure Optimizations for Excited States with Correlated Second-Order Methods: CC2 and ADC(2). *Adv. Quantum Chem.* **2005**, *50*, 37-60.
- (134) J. H. Starcke; M. Wormit; A. Dreuw, Unrestricted algebraic diagrammatic construction scheme of second order for the calculation of excited states of medium-sized and large molecules. *J. Chem. Phys.* **2009**, *130*, 024104.
- (135) D. Lefrancois; M. Wormit; A. Dreuw, Adapting algebraic diagrammatic construction schemes for the polarization propagator to problems with multi-reference electronic ground states exploiting the spin-flip ansatz. *J. Chem. Phys.* **2015**, *143*, 124107.
- (136) D. Lefrancois; D. R. Rehn; A. Dreuw, Accurate adiabatic singlet-triplet gaps in atoms and molecules employing the third-order spin-flip algebraic diagrammatic construction scheme for the polarization propagator. *J. Chem. Phys.* **2016**, *145*, 084102.
- (137) D. Lefrancois; D. Tuna; T. J. Martínez; A. Dreuw, The Spin-Flip Variant of the Algebraic-Diagrammatic Construction Yields the Correct Topology of S1/S0 Conical Intersections. *J. Chem. Theory Comput.* **2017**, *13*, 4436-4441.
- (138) J. Olsen; B. O. Roos; P. Jørgensen; H. J. r. A. Jensen, Determinant based configuration interaction algorithms for complete and restricted configuration interaction spaces. *J. Chem. Phys.* **1988**, *89*, 2185-2192.
- (139) P. Å. Malmqvist; A. Rendell; B. O. Roos, The restricted active space self-consistent-field method, implemented with a split graph unitary group approach. *J. Phys. Chem.* **1990**, *94*, 5477-5482.
- (140) D. Ma; G. Li Manni; L. Gagliardi, The generalized active space concept in multiconfigurational self-consistent field methods. *J. Chem. Phys.* **2011**, *135*, 044128.
- (141) B. O. Roos; K. Andersson, Multiconfigurational perturbation theory with level shift—the Cr2 potential revisited. *Chem. Phys. Lett.* **1995**, *245*, 215-223.

-
- (142) D. Roca-Sanjuán; F. Aquilante; R. Lindh, Multiconfiguration second-order perturbation theory approach to strong electron correlation in chemistry and photochemistry. *WIREs: Comput. Mol. Sci.* **2012**, *2*, 585-603.
- (143) G. Li Manni; S. D. Smart; A. Alavi, Combining the Complete Active Space Self-Consistent Field Method and the Full Configuration Interaction Quantum Monte Carlo within a Super-CI Framework, with Application to Challenging Metal-Porphyrins. *J. Chem. Theory Comput.* **2016**, *12*, 1245-1258.
- (144) R. E. Thomas; Q. Sun; A. Alavi; G. H. Booth, Stochastic Multiconfigurational Self-Consistent Field Theory. *J. Chem. Theory Comput.* **2015**, *11*, 5316-5325.
- (145) G. Li Manni; A. Alavi, Understanding the Mechanism Stabilizing Intermediate Spin States in Fe(II)-Porphyrin. *J. Phys. Chem. A* **2018**, *122*, 4935-4947.
- (146) G. K.-L. Chan; J. J. Dorando; D. Ghosh; J. Hachmann; E. Neuscamman; H. Wang; T. Yanai, An introduction to the density matrix renormalization group ansatz in quantum chemistry. In *Frontiers in quantum systems in chemistry and physics*, Springer: **2008**; pp 49-65.
- (147) S. Wouters; D. Van Neck, The density matrix renormalization group for ab initio quantum chemistry. *Eur. Phys. J. D* **2014**, *68*, 272.
- (148) S. R. White; R. L. Martin, Ab initio quantum chemistry using the density matrix renormalization group. *J. Chem. Phys.* **1999**, *110*, 4127-4130.
- (149) A. O. Mitrushenkov; G. Fano; F. Ortolani; R. Linguerri; P. Palmieri, Quantum chemistry using the density matrix renormalization group. *J. Chem. Phys.* **2001**, *115*, 6815-6821.
- (150) G. K.-L. Chan; M. Head-Gordon, Highly correlated calculations with a polynomial cost algorithm: A study of the density matrix renormalization group. *J. Chem. Phys.* **2002**, *116*, 4462-4476.
- (151) Ö. Legeza; J. Röder; B. Hess, Controlling the accuracy of the density-matrix renormalization-group method: The dynamical block state selection approach. *Phys. Rev. B* **2003**, *67*, 125114.
- (152) G. Moritz; M. Reiher, Decomposition of density matrix renormalization group states into a Slater determinant basis. *J. Chem. Phys.* **2007**, *126*, 244109.

- (153) E. G. Hohenstein; N. Luehr; I. S. Ufimtsev; T. J. Martínez, An atomic orbital-based formulation of the complete active space self-consistent field method on graphical processing units. *J. Chem. Phys.* **2015**, *142*, 224103.
- (154) J. W. Snyder Jr; E. G. Hohenstein; N. Luehr; T. J. Martínez, An atomic orbital-based formulation of analytical gradients and nonadiabatic coupling vector elements for the state-averaged complete active space self-consistent field method on graphical processing units. *J. Chem. Phys.* **2015**, *143*, 154107.
- (155) J. W. Snyder Jr; B. F. Curchod; T. J. Martínez, GPU-Accelerated State-Averaged Complete Active Space Self-Consistent Field Interfaced with Ab Initio Multiple Spawning Unravels the Photodynamics of Provitamin D3. *J. Phys. Chem. Lett.* **2016**, *7*, 2444-2449.
- (156) H. Werner; P. Knowles; G. Knizia; F. Manby; M. Schütz; P. Celani; W. Györfly; D. Kats; T. Korona; R. Lindh, *MOLPRO, 2012.1, a package of ab initio programs, 2012*, see <http://www.molpro.net>.
- (157) S. Goedecker, Linear scaling electronic structure methods. *Rev. Mod. Phys.* **1999**, *71*, 1085.
- (158) P. Hohenberg; W. Kohn, Inhomogeneous Electron Gas. *Phys. Rev.* **1964**, *136*, B864.
- (159) D. Rocca. Time-Dependent Density Functional Perturbation Theory: New algorithms with applications to molecular spectra. 2007.
- (160) J. P. Perdew; K. Burke; M. Ernzerhof, Generalized Gradient Approximation Made Simple. *Phys. Rev. Lett.* **1996**, *77*, 3865.
- (161) A. D. Becke, Density-functional thermochemistry. III. The role of exact exchange. *J. Chem. Phys.* **1993**, *98*, 5648-5652.
- (162) C. Lee; W. Yang; R. G. Parr, Development of the Colle-Salvetti correlation-energy formula into a functional of the electron density. *Phys. Rev. B* **1988**, *37*, 785.
- (163) J. P. Perdew; M. Ernzerhof; K. Burke, Rationale for mixing exact exchange with density functional approximations. *J. Chem. Phys.* **1996**, *105*, 9982-9985.
- (164) C. Adamo; V. Barone, Toward reliable density functional methods without adjustable parameters: The PBE0 model. *J. Chem. Phys.* **1999**, *110*, 6158-6170.
- (165) R. O. Jones, Density functional theory: Its origins, rise to prominence, and future. *Rev. Mod. Phys.* **2015**, *87*, 897.

-
- (166) J. Kalikka; J. Akola; R. Jones, Simulation of crystallization in Ge₂Sb₂Te₅: A memory effect in the canonical phase-change material. *Phys. Rev. B* **2014**, *90*, 184109.
- (167) C. Kunkel; C. Schober; J. T. Margraf; K. Reuter; H. Oberhofer, Finding the Right Bricks for Molecular Lego: A Data Mining Approach to Organic Semiconductor Design. *Chem. Mater.* **2019**, *31*, 969-978.
- (168) E. Schreiner; N. N. Nair; C. Wittekindt; D. Marx, Peptide Synthesis in Aqueous Environments: The Role of Extreme Conditions and Pyrite Mineral Surfaces on Formation and Hydrolysis of Peptides. *J. Am. Chem. Soc.* **2011**, *133*, 8216-8226.
- (169) I. Ugur; A. W. Rutherford; V. R. I. Kaila, Redox-coupled substrate water reorganization in the active site of photosystem II—the role of calcium in substrate water delivery. *Biochim. Biophys. Acta, Bioenerg.* **2016**, *1857*, 740-748.
- (170) E. Runge; E. K. U. Gross, Density-Functional Theory for Time-Dependent Systems. *Phys. Rev. Lett.* **1984**, *52*, 997.
- (171) L. González; D. Escudero; L. Serrano-Andrés, Progress and Challenges in the Calculation of Electronic Excited States. *ChemPhysChem* **2012**, *13*, 28-51.
- (172) M. E. Casida; M. Huix-Rotllant, Progress in time-dependent density-functional theory. *Ann. Rev. Phys. Chem.* **2012**, *63*, 287-323.
- (173) J. Hutter; M. Iannuzzi; F. Schiffmann; J. VandeVondele, CP2K: atomistic simulations of condensed matter systems. *WIREs Comput. Mol. Sci.* **2014**, *4*, 15-25.
- (174) S. Baroni; A. Dal Corso; S. De Gironcoli; P. Giannozzi; C. Cavazzoni; G. Ballabio; S. Scandolo; G. Chiarotti; P. Focher; A. Pasquarello, Quantum ESPRESSO: open-source package for research in electronic structure, simulation, and optimization. *Code available from <http://www.quantum-espresso.org>.*
- (175) M. Born; K. Huang, *Dynamical Theory of Crystal Lattices*. Oxford University Press: **1954**.
- (176) W. Domcke; D. R. Yarkony; H. Köppel (Eds.), *Conical Intersections: Electronic Structure, Dynamics and Spectroscopy*. World Scientific, Singapore: **2004**.
- (177) D. Heidrich (Ed.), *The Reaction Path in Chemistry: Current Approaches and Perspectives*. Kluwer Academic Publishers: Amsterdam, **1995**.

- (178) A. L. Sobolewski; W. Domcke, Ab Initio Studies of Reaction Paths in Excited-State Hydrogen-Transfer Processes. In *The Reaction Path in Chemistry: Current Approaches and Perspectives*, Heidrich, D., Ed. Kluwer Academic Publishers: Amsterdam, **1995**; pp 257-282.
- (179) W. Quapp, The Invariance of the Reaction Path Description in any Coordinate System. In *The Reaction Path in Chemistry: Current Approaches and Perspectives*, Heidrich, D., Ed. Kluwer Academic Publishers: Amsterdam, **1995**; pp 95-107.
- (180) D. R. Yarkony, Conical Intersections: Their Description and Consequences. In *Conical Intersections: Electronic Structure, Dynamics and Spectroscopy*, Domcke, W.; Yarkony, D. R.; Köppel, H., Eds. World Scientific: Singapore, **2004**; pp 41-127.
- (181) M. Olivucci, *Computational Photochemistry*. Elsevier: Amsterdam, **2005**.
- (182) M. Barbatti, Nonadiabatic dynamics with trajectory surface hopping method. *WIREs Comput. Mol. Sci.* **2011**, *1*, 620-633.
- (183) D. G. Truhlar; M. S. Gordon, From Force Fields to Dynamics: Classical and Quantal Paths. *Science* **1990**, *249*, 491-498.
- (184) J. Meisner; J. Kästner, Atom Tunneling in Chemistry. *Angew. Chem. Int. Ed.* **2016**, *55*, 5400-5413.
- (185) G. Worth; H. Meyer; L. Cederbaum, Multidimensional Dynamics Involving a Conical Intersection: Wavepacket Calculations Using the MCTDH Method. In *Conical Intersections: Electronic Structure, Dynamics and Spectroscopy*, Domcke, W.; Yarkony, D.; Köppel, H., Eds. World Scientific: Singapore, **2004**; pp 583-617.
- (186) G. Stock; M. Thoss, Mixed Quantum-Classical Description of the Dynamics at Conical Intersections. In *Conical Intersections: Electronic Structure, Dynamics and Spectroscopy*, Domcke, W.; Yarkony, D. R.; Köppel, H., Eds. World Scientific: Singapore, **2004**; pp 619-695.
- (187) M. Sapunar; A. Ponzi; S. Chaiwongwattana; M. Mališ; A. Prlj; P. Decleva; N. Došlić, Timescales of N-H bond dissociation in pyrrole: a nonadiabatic dynamics study. *Phys. Chem. Chem. Phys.* **2015**, *17*, 19012-19020.
- (188) V. Vallet; Z. Lan; S. Mahapatra; A. L. Sobolewski; W. Domcke, Photochemistry of pyrrole: Time-dependent quantum wave-packet description of the dynamics at the $1\pi\sigma^*$ -S0 conical intersections. *J. Chem. Phys.* **2005**, *123*, 144307.
- (189) A. Iqbal; V. G. Stavros, Exploring the Time Scales of H-atom Elimination from Photoexcited Indole. *J. Phys. Chem. A* **2009**, *114*, 68-72.

-
- (190) G. A. King; T. A. A. Oliver; M. N. R. Ashfold, Dynamical insights into $1\pi\sigma^*$ state mediated photodissociation of aniline. *J. Chem. Phys.* **2010**, *132*, 214307.
- (191) A. Iqbal; L.-J. Pegg; V. G. Stavros, Direct versus Indirect H atom Elimination from Photoexcited Phenol Molecules. *J. Phys. Chem. A* **2008**, *112*, 9531-9534.
- (192) C. Merschjann; T. Tyborski; S. Orthmann; F. Yang; K. Schwarzburg; M. Lublow; M.-C. Lux-Steiner; T. Schedel-Niedrig, Photophysics of polymeric carbon nitride: An optical quasimonomer. *Phys. Rev. B* **2013**, *87*, 205204.
- (193) Y. Kang; Y. Yang; L. C. Yin; X. Kang; G. Liu; H. M. Cheng, An Amorphous Carbon Nitride Photocatalyst with Greatly Extended Visible-Light-Responsive Range for Photocatalytic Hydrogen Generation. *Adv. Mater.* **2015**, *27*, 4572-4577.
- (194) V. W.-h. Lau; M. B. Mesch; V. Duppel; V. Blum; J. r. Senker; B. V. Lotsch, Low-Molecular-Weight Carbon Nitrides for Solar Hydrogen Evolution. *J. Am. Chem. Soc.* **2015**, *137*, 1064-1072.
- (195) W. Wei; T. Jacob, Strong excitonic effects in the optical properties of graphitic carbon nitride g-C₃N₄ from first principles. *Phys. Rev. B* **2013**, *87*, 085202.
- (196) M. N. Huda; J. A. Turner, Morphology-dependent optical absorption and conduction properties of photoelectrochemical photocatalysts for H₂ production: A case study. *J. Appl. Phys.* **2010**, *107*, 123703.
- (197) C. Merschjann; S. Tschierlei; T. Tyborski; K. Kailasam; S. Orthmann; D. Hollmann; T. Schedel-Niedrig; A. Thomas; S. Lochbrunner, Complementing Graphenes: 1D Interplanar Charge Transport in Polymeric Graphitic Carbon Nitrides. *Adv. Mater.* **2015**, *27*, 7993-7999.
- (198) G. A. Meek; A. D. Baczewski; D. J. Little; B. G. Levine, Polaronic Relaxation by Three-Electron Bond Formation in Graphitic Carbon Nitrides. *J. Phys. Chem. C* **2014**, *118*, 4023-4032.
- (199) K. Huang; Y. Hong; X. Yan; C. Huang; J. Chen; M. Chen; W. Shi; C. Liu, Hydrothermal synthesis of gC₃N₄/CdWO₄ nanocomposite and enhanced photocatalytic activity for tetracycline degradation under visible light. *CrystEngComm* **2016**, *18*, 6453-6463.
- (200) X. She; L. Liu; H. Ji; Z. Mo; Y. Li; L. Huang; D. Du; H. Xu; H. Li, Template-free synthesis of 2D porous ultrathin nonmetal-doped g-C₃N₄ nanosheets with highly efficient photocatalytic H₂ evolution from water under visible light. *Appl. Catal., B* **2016**, *187*, 144-153.

-
- (201) P. Niu; L. C. Yin; Y. Q. Yang; G. Liu; H. M. Cheng, Increasing the Visible Light Absorption of Graphitic Carbon Nitride (Melon) Photocatalysts by Homogeneous Self-Modification with Nitrogen Vacancies. *Adv. Mater.* **2014**, *26*, 8046-8052.
- (202) G. Liu; P. Niu; C. Sun; S. C. Smith; Z. Chen; G. Q. Lu; H.-M. Cheng, Unique Electronic Structure Induced High Photoreactivity of Sulfur-Doped Graphitic C₃N₄. *J. Am. Chem. Soc.* **2010**, *132*, 11642-11648.
- (203) E. J. Rabe; K. L. Corp; A. L. Sobolewski; W. Domcke; C. W. Schlenker, Proton-Coupled Electron Transfer from Water to a Model Heptazine-Based Molecular Photocatalyst. *J. Phys. Chem. Lett.* **2018**, *9*, 6257-6261.
- (204) X. Pang; C. Jiang; W. Domcke, Photoinduced electron-driven proton transfer from water to an N-heterocyclic chromophore: nonadiabatic dynamics studies for pyridine-water clusters. *Phys. Chem. Chem. Phys.* **2019**, Advance Article.
- (205) X. Pang; J. Ehrmaier; X. Wu; C. Jiang; W. Xie; A. L. Sobolewski; W. Domcke, Photoinduced hydrogen-transfer reactions in pyridine-water clusters: Insights from excited-state electronic-structure calculations. *Chem. Phys.* **2018**, *515*, 550-556.
- (206) Y. Zhu; D. Zhang; L. Gong; L. Zhang; Z. Xia, Catalytic Activity Origin and Design principles of Graphitic Carbon Nitride Electrocatalysts for Hydrogen Evolution. *Front. Mater.* **2019**, *6*, 16.

Appendix: Publications

(1) J. Ehrmaier; M. J. Janicki; A. L. Sobolewski; W. Domcke, Mechanism of photocatalytic water splitting with triazine-based carbon nitrides: insights from ab initio calculations for the triazine-water complex. *Phys. Chem. Chem. Phys.* **2018**, *20*, 14420-14430

(2) J. Ehrmaier; T. N. V. Karsili; A. L. Sobolewski; W. Domcke, Mechanism of Photocatalytic Water Splitting with Graphitic Carbon Nitride: Photochemistry of the Heptazine–Water Complex. *J. Phys. Chem. A* **2017**, *121*, 4754-4764.

(3) J. Ehrmaier; W. Domcke; D. Opalka, Mechanism of Photocatalytic Water Oxidation by Graphitic Carbon Nitride. *J. Phys. Chem. Lett.* **2018**, *9*, 4695-4699.

(4) J. Ehrmaier; A. L. Sobolewski; W. Domcke, Role of the Pyridinyl Radical in the Light-Driven Reduction of Carbon Dioxide: A First-Principles Study. *J. Phys. Chem. A* **2019**, *123*, 3678-3684.



Cite this: *Phys. Chem. Chem. Phys.*,
2018, 20, 14420

Mechanism of photocatalytic water splitting with triazine-based carbon nitrides: insights from *ab initio* calculations for the triazine–water complex†

Johannes Ehrmaier,^{id}*^a Mikołaj J. Janicki,^{id}‡^a Andrzej L. Sobolewski^{id}^b and Wolfgang Domcke^{id}^a

Polymeric carbon-nitride materials consisting of triazine or heptazine units have recently attracted vast interest as photocatalysts for water splitting with visible light. Adopting the hydrogen-bonded triazine–water complex as a model system, we explored the photochemical reaction mechanisms involved in the water splitting reaction in this system, using wavefunction-based *ab initio* electronic-structure methods. It is shown that photoexcited triazine can abstract a hydrogen atom from the water molecule by the sequential transfer of an electron and a proton from water to triazine, resulting in the triazinyl-hydroxyl biradical in the electronic ground state. It is furthermore shown that the excess hydrogen atom of the triazinyl radical can be photodetached by a second photon, which regenerates the triazine molecule. The hydrogen-bonded water molecule is thus decomposed into hydrogen and hydroxyl radicals in a biphotonic photochemical reaction. These results shed light on the molecular mechanisms of the water-oxidation reaction catalyzed by triazine-based organic polymers.

Received 28th March 2018,
Accepted 8th May 2018

DOI: 10.1039/c8cp01998c

rsc.li/pccp

1. Introduction

Polymeric or partially crystalline materials consisting of *s*-triazine or heptazine (tri-*s*-triazine) units connected by imide groups or nitrogen atoms and collectively referred to as graphitic carbon nitrides (g-C₃N₄) have received enormous attention since the discovery of their photocatalytic activity for hydrogen evolution with visible ($\lambda > 400$ nm) light,¹ see ref. 2–7 for reviews. Most of these materials are closely related to Liebig's "melon"⁸ and are composed of imide-linked heptazine building blocks. Polymeric carbon nitrides consisting of triazine building blocks have also been synthesized^{9–12} and their ability to catalyze hydrogen evolution under irradiation with visible light was demonstrated.^{9,10,12–14} A colloidal Pt co-catalyst and a sacrificial electron donor (usually triethanolamine (TEA)) are required for efficient water photolysis.

In pioneering work in the 1980s and early 1990s, Yamagida and coworkers demonstrated (sacrificial) hydrogen evolution with π -conjugated linear polymers, such as polyphenylene (PP)

or polypyridine (PPy), in the presence of colloidal noble metals.^{15,16} More recently, two-dimensional covalent organic frameworks consisting of N-heterocycles connected by aromatic linkers were synthesized and tested for visible-light-induced hydrogen evolution.^{17–24} Both for the polymers^{15,16} as well as for the covalent organic frameworks,^{20,22} the hydrogen evolution efficiency was found to scale systematically with the nitrogen content of the heterocycles. These findings indicate that the heterocyclic nitrogen atoms play an essential role in the photocatalysis.²⁰

The generally accepted mechanistic picture of photocatalysis with carbon nitrides is inspired by earlier interpretations of photoelectrochemical water splitting with transition-metal oxides and invokes the photogeneration of excitons, followed by exciton dissociation and migration of charge carriers (electrons and holes) in the semiconducting material. The electrons and holes are assumed to drive the reduction of protons and the oxidation of water, respectively, at the interfaces of the semiconductor with the aqueous environment. However, exciton dissociation energies of organic polymers are of the order of electron volts^{6,25–27} and polaron stabilization energies also are substantial.^{28,29} It seems therefore unlikely that the scenario devised for photocatalysis with three-dimensional transition-metal-oxide semiconductors is appropriate for one-dimensional or two-dimensional organic polymers. Indeed, it has been shown that small oligomers of pyridine or triazine are as efficient as photocatalysts as linear polymers or two-dimensional covalent organic frameworks.^{30,31} These findings provide strong evidence for a molecular photochemical mechanism

^a Department of Chemistry, Technical University of Munich, D-85747 Garching, Germany. E-mail: johannes.ehrmaier@tum.de, domcke@ch.tum.de

^b Institute of Physics, Polish Academy of Sciences, PL-02-668 Warsaw, Poland

† Electronic supplementary information (ESI) available: Description of the computational methods, vertical excitation energies of triazine, the triazine–H₂O complex and the triazinyl radical. See DOI: 10.1039/c8cp01998c

‡ Present address: Department of Physical and Quantum Chemistry, Faculty of Chemistry, Wrocław University of Science and Technology, PL-50-370, Wrocław, Poland.

of the hydrogen evolution reaction at single catalytically active units of these organic materials.

In previous theoretical studies, the band structures of periodic triazine-based materials were investigated with density functional theory (DFT).^{32–34} Butchosa *et al.* computed the optical properties of triphenyl-triazine oligomers and clusters thereof with time-dependent DFT (TDDFT) and coupled-cluster (CC2) methods.³⁵ Srinivasu and Ghosh also studied the adsorption of water molecules and radicals on periodic triazine-based systems and calculated the energy profile for the dissociation of an adsorbed water molecule, which exhibits the expected high barrier (>2.0 eV).³⁶

A photochemical reaction mechanism for water splitting which focusses on the specific properties of the electron-deficient N-atoms in aromatic heterocycles was recently proposed for the hydrogen-bonded complexes of pyridine,^{37,38} acridine³⁹ and heptazine⁴⁰ with water molecules. The mechanism of hydrogen bonding, the topographies of the excited-state potential-energy (PE) surfaces and the excited-state reaction paths for electron/proton transfer were characterized with *ab initio* electronic-structure calculations. These calculations indicate that the N-atoms of the aromatic heterocycles are the active sites for the photoinduced water splitting reaction. The primary photochemical reaction mechanism was shown to be the transfer of an electron from the hydrogen-bonded water molecule to the photoexcited chromophore, where the electron fills the vacancy in the π orbital generated by the photoexcitation. The electron transfer is followed by the transfer of a proton from the hydrogen-bonded water molecule to the chromophore (the proton follows the electron), which results in the formation of a neutral hypervalent heterocyclic radical and an OH radical in their electronic ground states. The excess hydrogen atom of the heterocyclic radical can be photodetached by a second photon, which regenerates the heterocycle. Alternatively to the photodetachment reaction, two heterocyclic radicals can recombine in an exothermic dark reaction to form molecular hydrogen.^{37–40}

In the present work, we explored the details of this biphotonic photochemical water-splitting mechanism for the triazine–H₂O complex, complementing earlier studies for the pyridine–H₂O, acridine–H₂O and heptazine–H₂O complexes. Due to the localization of the water-splitting reaction on a single N-atom of the chromophore, the essence of the photochemical reactions can be revealed for the hydrogen-bonded complex of triazine with a single water molecule. The small size of the model system allows us to explore the excited electronic states and their PE surfaces with accurate wave-function based electronic-structure methods. Because the intermediate and final products are neutral radicals rather than ions, dielectric screening effects of the aqueous environment are of minor importance and can be taken into account, if necessary, by a polarizable continuum model. Calculations for clusters of heterocycles with several water molecules are in progress and the results will be presented elsewhere.

In the recent investigation of the photochemistry of the heptazine–H₂O complex,⁴⁰ only selected excited electronic states were considered due to the high cost of excited-state electronic-structure calculations for this system. For the smaller triazine–H₂O system, we were able to perform a more comprehensive

computational investigation which includes all photophysically and photochemically relevant singlet and triplet excited states. This rather complete data set may serve as a reference for future computational studies of photochemical reactions of heterocycles with water molecules.

II. Results and discussion

A. Photoinduced H-atom transfer from water to triazine

The optimized geometry of the lowest-energy conformer of the hydrogen-bonded triazine–water complex, obtained with the MP2 method and the aug-cc-pVDZ basis set (see Section I of the ESI† for the description of the computational methods) is shown in Fig. 1(a). The geometry is planar (C_s symmetry). The length of the hydrogen bond is 2.033 Å. The distance between the O-atom of water and the H-atom of the closest CH group of triazine is 2.602 Å. This very weak hydrogen bond with the CH group may be the reason why the search for a second energy minimum with a perpendicular orientation of the water molecule was not successful.

The Hartree–Fock (HF) molecular orbitals which are relevant for the lowest excited electronic states of the triazine–water complex are shown in Fig. 2. The occupied nonbonding orbitals are the three n orbitals of the three nitrogen atoms of triazine (19a', 21a', 22a') and the p_x/p_y orbitals on the oxygen atom of water (16a', 20a'). The orbitals 3a'' and 4a'' are the highest two π orbitals of triazine, while the orbital 2a'' is the p_z orbital on the oxygen atom of water. The orbitals 5a'', 6a'', 7a'' are the π^* orbitals of triazine. Excited states which involve electronic transitions only among the orbitals of triazine are referred to as locally excited states and are denoted as $\pi\pi^*(LE)$ and $n\pi^*(LE)$. Excited states which involve electronic transitions from occupied p_z or $p_{x,y}$ orbitals of water to π^* orbitals of triazine are referred to as charge-transfer excited states and are denoted as $p_z\pi^*(CT)$ or $p_{x,y}\pi^*(CT)$.

A complete survey of the vertical excitation energies and transition dipole moments of isolated triazine and the triazine–water complex, including a comparison of the results of different electronic-structure methods, is given in Section II of the ESI.† For the convenience of the reader, a summary of the vertical excitation energies and their oscillator strengths for the triazine–water complex, calculated at the ADC(2)/aug-cc-pVDZ level, is given in Table 1. The lowest four locally excited singlet states of the triazine–water complex with calculated excitation energies of 4.48–4.77 eV correspond to the $^1A_2''$, $^1A_1''$ and $^1E''$ $n\pi^*$ excited states of triazine. The next four locally excited singlet states with

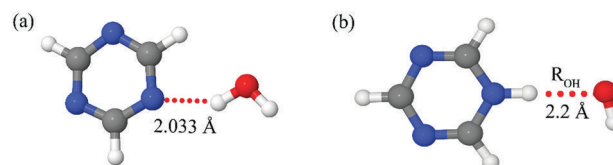


Fig. 1 (a) Geometry of the triazine water complex at the ground-state equilibrium geometry; (b) geometry of the triazinyl-OH biradical. The energy has been optimized for the lowest $^1p_z\pi^*(CT)$ state at $R_{OH} = 2.2$ Å.

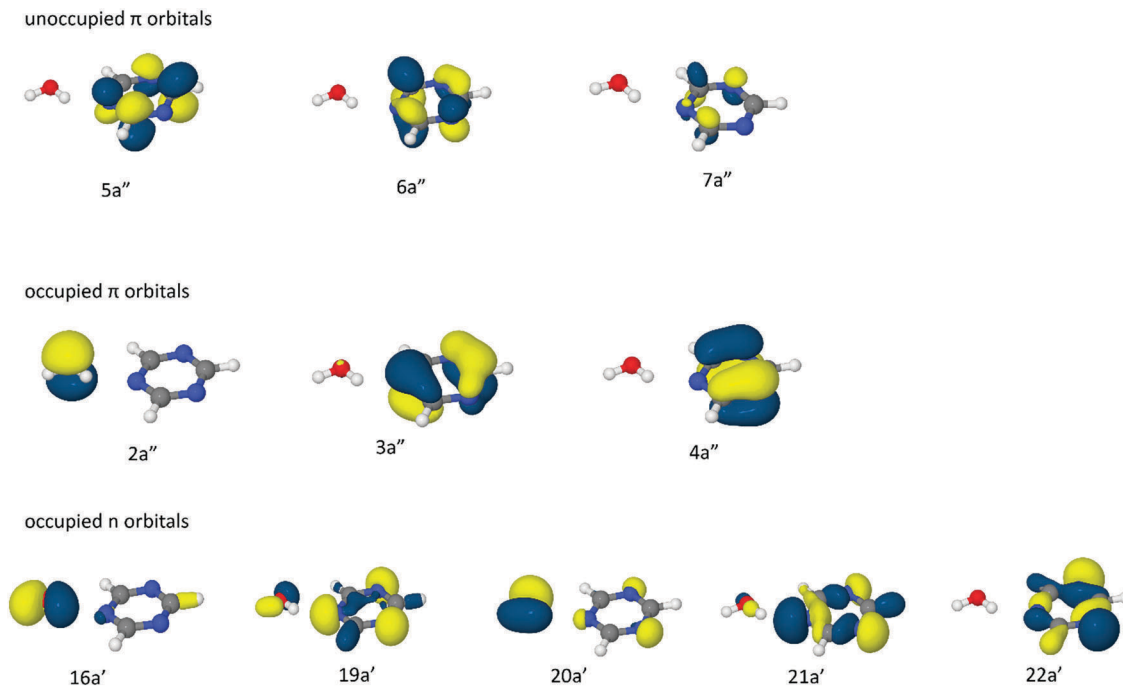


Fig. 2 Selected Hartree-Fock orbitals of the triazine-water complex at the ground-state equilibrium geometry.

Table 1 Vertical excitation energies E (in eV) and oscillator strengths f (multiplied by 10) of the triazine-water complex, calculated with the ADC(2) method

State	Symmetry	Character	Orbital transitions	E	$f (\times 10)$
S ₁	A''	$n\pi^*$	$22a' \rightarrow 5a''$	4.48	0.00
S ₂	A''	$n\pi^*$	$22a' \rightarrow 6a''$	4.60	0.05
S ₃	A''	$n\pi^*$	$21a' \rightarrow 5a''$	4.73	0.03
S ₄	A''	$n\pi^*$	$21a' \rightarrow 6a''$	4.77	0.00
S ₅	A'	$\pi\pi^*$	$4a'' \rightarrow 5a''$	5.70	0.00
			$3a'' \rightarrow 6a''$		
S ₆	A'	$\pi\pi^*$	$3a'' \rightarrow 5a''$	7.08	0.02
			$4a'' \rightarrow 6a''$		
S ₇	A'	$\pi\pi^*$	$4a'' \rightarrow 5a''$	7.65	3.32
			$3a'' \rightarrow 6a''$		
S ₈	A'	$\pi\pi^*$	$3a'' \rightarrow 5a''$	7.66	3.60
			$4a'' \rightarrow 6a''$		
S ₉	A''	$n\pi^*$	$22a' \rightarrow 7a''$	7.73	0.00
S ₁₀	A''	$n\pi^*$	$21a' \rightarrow 7a''$	7.87	0.00
CT	A'	$\pi\pi^*$	$2a'' \rightarrow 6a''$	7.84	0.91
CT	A'	$\pi\pi^*$	$2a'' \rightarrow 5a''$	7.93	0.47

calculated excitation energies of 5.70–7.66 eV arise from the ${}^1A_2'$, ${}^1A_1'$ and ${}^1E'$ $\pi\pi^*$ excited states of triazine. The water molecule does not absorb in this energy range. The ${}^1n\pi^*$ states and the lowest ${}^1\pi\pi^*$ states have rather low oscillator strengths (most of them are symmetry-forbidden in isolated triazine). The lowest strongly absorbing states are the nearly degenerate states S₇ and S₈, derived from the ${}^1E'$ ($\pi\pi^*$) excited state of triazine with vertical excitation energies of 7.65 and 7.66 eV and a cumulative oscillator strength of 0.69. These results are in qualitative agreement with the experimental absorption spectrum of triazine which exhibits weak absorption bands of the ${}^1n\pi^*$ and ${}^1\pi\pi^*$ valence states up to about 6.0 eV and a very strong absorption band at about 7.8 eV.^{41,42} In the present context, photoexcitation of the ${}^1E'$ ($\pi\pi^*$)

state of triazine is not of relevance, since its absorption band is far outside of the spectral window of interest for solar water splitting. However, the low-lying weak or nominally forbidden $S_0 \rightarrow {}^1\pi\pi^*$ and $S_0 \rightarrow {}^1n\pi^*$ transitions can borrow intensity from the strongly allowed $S_0 \rightarrow {}^1E'$ ($\pi\pi^*$) transition *via* vibronic coupling. In oligomers, polymers and in covalent organic frameworks, the lowest ${}^1n\pi^*$ and ${}^1\pi\pi^*$ states are red-shifted, which results in the observed absorption edge near 400 nm (3.1 eV) of these materials.³⁵ The lowest singlet state of charge-transfer character, corresponding to the transition from the p_z orbital of water ($2a''$) to the second π^* orbital of triazine ($6a''$) has a vertical excitation energy of 7.84 eV, lying only slightly higher than the bright S₇, S₈ states (see Table 1).

The energies of the four lowest ${}^3n\pi^*$ states are 4.23–4.62 eV, while the four lowest ${}^3\pi\pi^*$ states are found at 4.97–5.63 eV at the ADC(2) level. The lowest triplet state of charge-transfer character has a vertical excitation energy of 7.80 eV. For more details on the vertical excitation energies we refer to Tables SI–SIV of the ESI.†

To render the following discussion of the H-atom transfer reaction in the triazine-water complex as clear as possible, we refer to diabatic electronic states in terms of their spin multiplicity (superscript), their orbital character (orbital transitions with respect to the electronic ground state) and their locally excited (LE) or charge-transfer (CT) character; for example, ${}^1p_z\pi^*(CT)$ stands for a singlet charge-transfer state, in which an electron is transferred from the p_z orbital of water to a π^* orbital of triazine. When we refer to electronic states of ${}^1,3n\pi^*$ or ${}^1,3\pi\pi^*$ character in general (that is, both locally excited and charge-transfer states), it is convenient to use the symmetry labels ${}^1,3A''$ and ${}^1,3A'$, respectively. The $\pi\pi^*(LE)$ and $p_z\pi^*(CT)$ excited states are of A' symmetry,

while the $n\pi^*(LE)$ and $p_{xy}\pi^*(CT)$ excited states are of A'' symmetry. Adiabatic electronic states are labeled, as usual, by their energetic ordering, that is, S_0, S_1, S_2, \dots and T_1, T_2, \dots

To characterize the energetics of the excited-state H-atom transfer reaction from water to triazine in the triazine–water complex, minimum-energy reaction paths (relaxed scans) were computed with the ADC(2) method along the reaction coordinate for H-atom transfer as described in Section I of the ESI.† The driving coordinate of the relaxed scan is chosen as the OH bond length R_{OH} of the OH group of the water molecule which is involved in the hydrogen bonding (see Fig. 1(a)). Small values of R_{OH} (≈ 1.0 Å) correspond to the triazine–water complex (Fig. 1(a)), while large values of R_{OH} (≈ 2.2 Å) represent a triazinyl radical (*N*-hydrogenated triazine) which is hydrogen bonded to a hydroxyl radical (Fig. 1(b)).

Fig. 3 shows the PE profiles of the $^1A'$ (a), $^1A''$ (b), $^3A'$ (c) and $^3A''$ (d) states of the triazine–water complex along the minimum-energy reaction path for H-atom transfer. Full dots indicate that the energy has been minimized for this electronic state, while open circles show energies calculated at geometries optimized for a different electronic state. The dashed vertical line separates, for clarity, the energies calculated for different reaction paths. In the left part of Fig. 3(a)–(d), the energy was optimized for the electronic ground state (black dots) and the excitation energies of the locally excited $^1\pi\pi^*$, $^1n\pi^*$, $^3\pi\pi^*$ and $^3n\pi^*$ states were calculated for these geometries (open circles). The PE functions of all these excited states exhibit minima as a function of the

reaction coordinate R_{OH} which are very close to the minimum of the electronic ground state. There exists thus no driving force for proton transfer in the locally excited electronic states. In the right part of Fig. 3(a)–(d), the energy was optimized for the lowest charge-transfer state of the corresponding symmetry (blue dots for $^1,3p_z\pi^*(CT)$ states, purple dots for $^1,3p_{xy}\pi^*(CT)$ states). The energy of the next higher CT state and the energy of the closed-shell state (corresponding to the electronic ground-state in the FC region) calculated at these geometries are given by the open circles. The discontinuities of the PE profiles at $R_{OH} = 1.2$ Å (dashed vertical line) reflect the fact that the energy profiles were computed along different reaction paths.

As Fig. 3(a) shows, the transfer of a proton from water to triazine stabilizes the $^1p_z\pi^*(CT)$ state by more than 2.0 eV. The crossing of the PE function of the $^1p_z\pi^*(CT)$ state with the PE function of the closed-shell S_0 state occurs at 1.80 Å. After the transfer of the proton (that is, at $R_{OH} \approx 2.2$ Å), the lowest $^1p_z\pi^*(CT)$ state is the most stable electronic state and represents a (hydrogen-bonded) triazinyl-hydroxyl biradical. The biradical is thus a photophysically stable species. The geometric structure of the biradical is shown in Fig. 1(b). The energy minimum of the biradical is 2.8 eV above the energy minimum of the S_0 state. Therefore, 2.8 eV of the energy of the absorbed photon have been stored as chemical energy in the biradical.

Fig. 3(b) shows the corresponding energy profiles along the H-atom transfer coordinate for the $^1n\pi^*(LE)$ and $^1p_{xy}\pi^*(CT)$ states. The purple curve with dots in Fig. 3(b) represents the

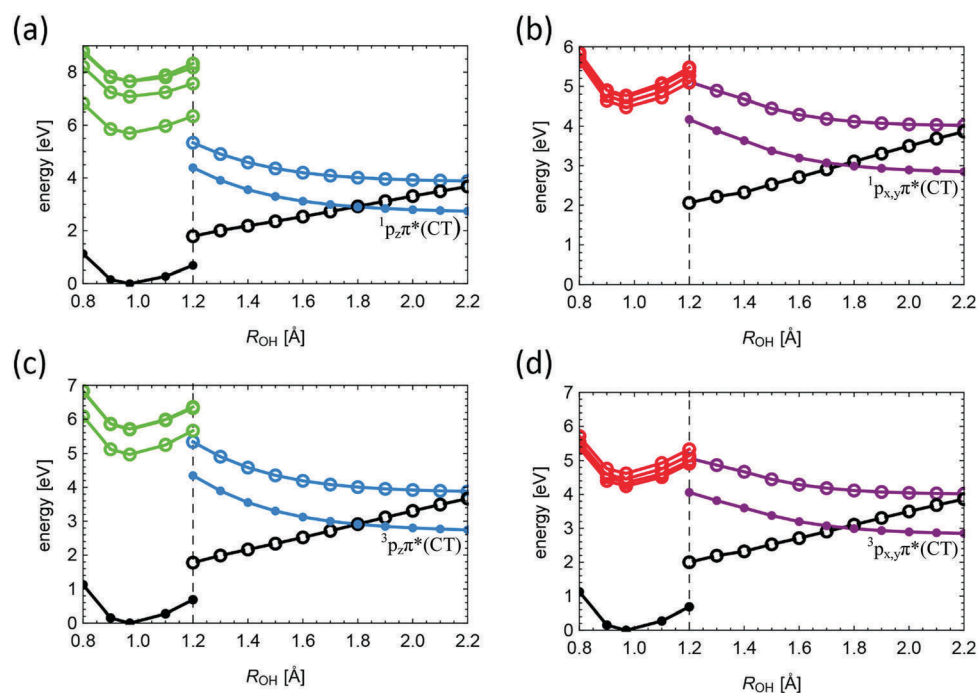


Fig. 3 Energy profiles for the H-atom transfer reaction from water to triazine calculated with the ADC(2) method. Full dots indicate that the energy of this electronic state was optimized. Circles represent energies that were calculated at the optimized geometry of another electronic state. In the left part ($R_{OH} < 1.2$ Å), the energy has been optimized for the electronic ground state (black). In the right part ($R_{OH} > 1.2$ Å), the energy of the (a) $^1p_z\pi^*(CT)$ state (blue dots), (b) $^1p_{xy}\pi^*(CT)$ state (purple dots), (c) $^3p_z\pi^*(CT)$ state (blue dots) and (d) $^3p_{xy}\pi^*(CT)$ state (purple dots) has been optimized. The blue and purple open circles represent the energy of the next CT state of the corresponding symmetry. Black: S_0 state, green (a): $^1\pi\pi^*(LE)$ states, green (c): $^3\pi\pi^*(LE)$ states, red (b): $^1n\pi^*(LE)$ states, red (d): $^3n\pi^*(LE)$ states.

optimized energy of the lowest ${}^1p_{x,y}\pi^*(CT)$ state, corresponding to the electronic transition from the highest $p_{x,y}$ orbital of water (20a') to the lowest π^* orbital of triazine (5a''). The crossing of the PE function of the ${}^1p_{x,y}\pi^*(CT)$ state with the PE function of the closed-shell S_0 state occurs at 1.75 Å. The energy of the biradicalic minimum is 2.9 eV above the ground-state minimum, see Fig. 3(b). Overall, the PE functions of the ${}^1p_z\pi^*(CT)$ and ${}^1p_{x,y}\pi^*(CT)$ states are very similar, the ${}^1p_z\pi^*$ biradical being slightly lower in energy than the ${}^1p_{x,y}\pi^*$ biradical.

The PE functions of the triplet states of A' and A'' symmetry as functions of the proton transfer coordinate are displayed in Fig. 3(c) and (d), respectively. For the $p_z\pi^*(CT)$ and $p_{x,y}\pi^*(CT)$ biradicals, singlet and triplet spin couplings are degenerate, since the exchange integral vanishes for non-overlapping orbitals. The locally excited ${}^3\pi\pi^*$ states, on the other hand, are significantly lower in energy than their ${}^1\pi\pi^*$ counterparts, see Fig. 3(a) and (c).

Thus there exist low-lying charge-transfer states of the four types ${}^1p_z\pi^*(CT)$, ${}^1p_{x,y}\pi^*(CT)$, ${}^3p_z\pi^*(CT)$ and ${}^3p_{x,y}\pi^*(CT)$ along the minimum-energy reaction path for proton transfer from water to triazine. At an OH distance of 1.2 Å (which corresponds to a ≈ 0.2 Å extension of the bond length of the hydrogen-bonded water molecule from equilibrium), all these charge-transfer states are located at an energy of ≈ 4.5 eV, which is about the

same as the vertical excitation energy of the locally excited ${}^1n\pi^*$ and ${}^3n\pi^*$ states, while the vertical excitation energy of the lowest ${}^1\pi\pi^*$ state is higher, see Fig. 3.

To explore the connection of the PE surfaces between the region of small R_{OH} (triazine–water complex) and large R_{OH} (triazinyl–OH biradical), we calculated two-dimensional relaxed PE surfaces of the triazine–water complex. The two fixed coordinates are the OH distance of water (R_{OH}) and the distance R_{ON} between the oxygen atom of water (the H-atom donor) and the nitrogen atom of triazine (the H-atom acceptor). The energies of the lowest adiabatic excited states of ${}^1A'$, ${}^1A''$, ${}^3A'$ and ${}^3A''$ symmetry, respectively, were minimized with respect to all remaining internal nuclear coordinates, except the CH bond lengths. The latter had to be constrained to suppress unwanted side reactions. These two-dimensional relaxed energy surfaces are shown in Fig. 4(a)–(d).

All four PE surfaces exhibit two minima which are separated by a saddle point (marked by the circle). The upper left minimum is located in the Franck–Condon (FC) region of the triazine–water complex (small R_{OH} , large R_{ON}) and represents the equilibrium geometry of the corresponding locally excited state. The lower right minimum (large R_{OH} , small R_{ON}) represents the equilibrium geometry of the corresponding biradical, in

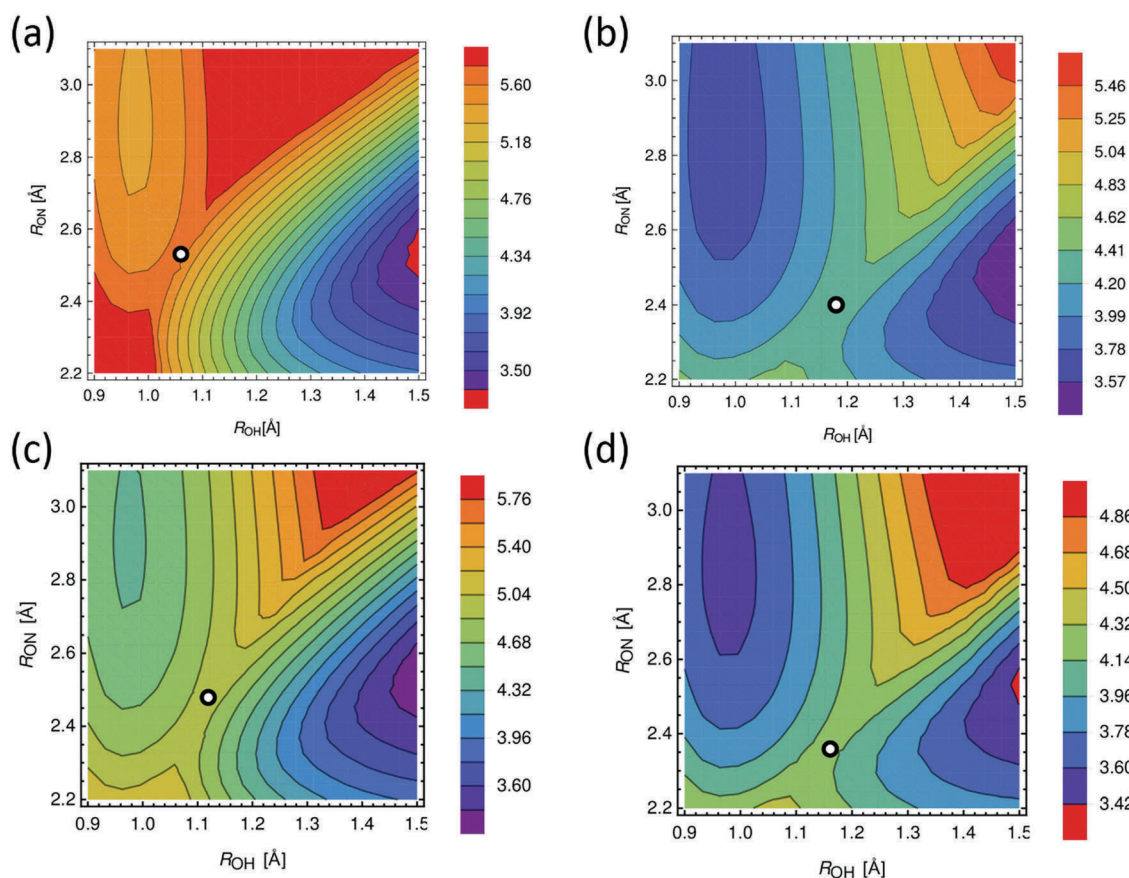


Fig. 4 Relaxed PE surfaces of the lowest excited states of the triazine–water complex, calculated with the ADC(2) method. (a) ${}^1A'$ surface, (b) ${}^1A''$ surface, (c) ${}^3A'$ surface, (d) ${}^3A''$ surface. The minimum for small R_{OH} represents the FC minimum of the (a) ${}^1\pi\pi^*(LE)$ state, (b) ${}^1n\pi^*(LE)$ state, (c) ${}^3\pi\pi^*(LE)$ state and (d) ${}^3n\pi^*(LE)$ state. The minimum for large R_{OH} represents the biradical of the corresponding symmetry. The circle indicates the saddle point. Energies with respect to the ground-state equilibrium energy are given in eV (see color code).

which both electron and proton are transferred from water to triazine. The FC minimum corresponds to the PE functions in the left part of Fig. 3 ($R_{\text{OH}} < 1.2 \text{ \AA}$), while the biradicalic minimum corresponds to the PE functions in the right part of Fig. 3 ($R_{\text{OH}} > 1.2 \text{ \AA}$). At the saddle point, the character of the electronic state changes from locally excited (left) to charge transfer (right). The electronic energies (see color code) are given with respect to the ground-state (S_0) energy minimum. It should be noted that the saddle points shown in Fig. 4 reflect the existence of nearby conical intersections. Since the locally excited states and the charge-transfer states have the same symmetry in each of the four figures, these are so-called no-symmetry conical intersections. Their existence is not due to symmetry, but due to the fact that the dimension of the branching space, $d = 2$, is small compared to the number of internal nuclear degrees of freedom of the system.

The $1^1A'$ energy surface (Fig. 4(a)) exhibits a minimum of the locally excited $1^1\pi\pi^*$ state at 5.4 eV, a saddle point at 5.6 eV and a minimum of the biradical at 3.3 eV. The saddle point is 0.2 eV above the minimum of the $1^1\pi\pi^*(\text{LE})$ state, but slightly (0.1 eV) below the vertical excitation energy of the $1^1\pi\pi^*(\text{LE})$ state. The corresponding relaxed PE surface of the lowest $1^1A''$ state is shown in Fig. 4(b). The saddle point separating the two minima is 4.31 eV above the S_0 minimum, 0.64 eV above the energy minimum of the $1^1\pi\pi^*(\text{LE})$ state and 0.17 eV below the vertical excitation energy of the $1^1\pi\pi^*(\text{LE})$ state. The H-atom transfer reaction in the triazine–water complex is thus nominally barrierless with respect to the vertical excitation energies of the lowest $1^1\pi\pi^*(\text{LE})$ and $1^1n\pi^*(\text{LE})$ states, although there are barriers with respect to the minima of the PE surfaces of the locally excited states. The higher

barrier with respect to the $1^1n\pi^*(\text{LE})$ minimum in Fig. 4(b) reflects the larger vibrational stabilization energy of the locally excited $1^1n\pi^*$ state.

The corresponding relaxed PE surfaces of the lowest $3^1A'$ and $3^1A''$ states are displayed in Fig. 4(c) and (d), respectively. Their topography is similar to that of the corresponding singlet states. On the $3^1A'$ surface (Fig. 4(c)), the barrier for H-atom transfer with respect to the $1^1\pi\pi^*(\text{LE})$ minimum is 0.4 eV, about twice the barrier on the $1^1A'$ surface. The reason for the higher barrier of the triplet surface is the lower energy of the locally excited triplet states compared to the locally excited singlet states, whereas singlets and triplets are approximately degenerate for the charge-transfer states. The $3^1A''$ PE surface (Fig. 4(d)) has the lowest energy minimum in the FC zone (3.6 eV). The energy of the saddle point is 4.2 eV, which results in a substantial barrier for H-atom transfer of 0.6 eV, comparable to the barrier of the $1^1A''$ surface.

It is hardly possible to compute two-dimensional relaxed scans for the higher excited states of the complex. To nevertheless obtain information on energy crossings involving higher excited states, we constructed a linearly interpolated reaction path (LIRP) labeled by the coordinate X between the ground-state equilibrium geometry ($R_{\text{OH}} = 1.0 \text{ \AA}$, $X = 0.0$) and the optimized geometry of the lowest charge-transfer state of each symmetry at fixed $R_{\text{OH}} = 1.2 \text{ \AA}$ ($X = 1.0$). We performed single-point energy calculations along this path for the states of the four symmetries $1A'$, $1A''$, $3A'$ and $3A''$. The resulting energy profiles are displayed in Fig. 5.

Fig. 5(a) shows the energy profiles of the four locally excited $1^1\pi\pi^*$ states (green) and the two lowest $1^1p_z\pi^*(\text{CT})$ states (blue). These two charge-transfer states arise from transitions from the

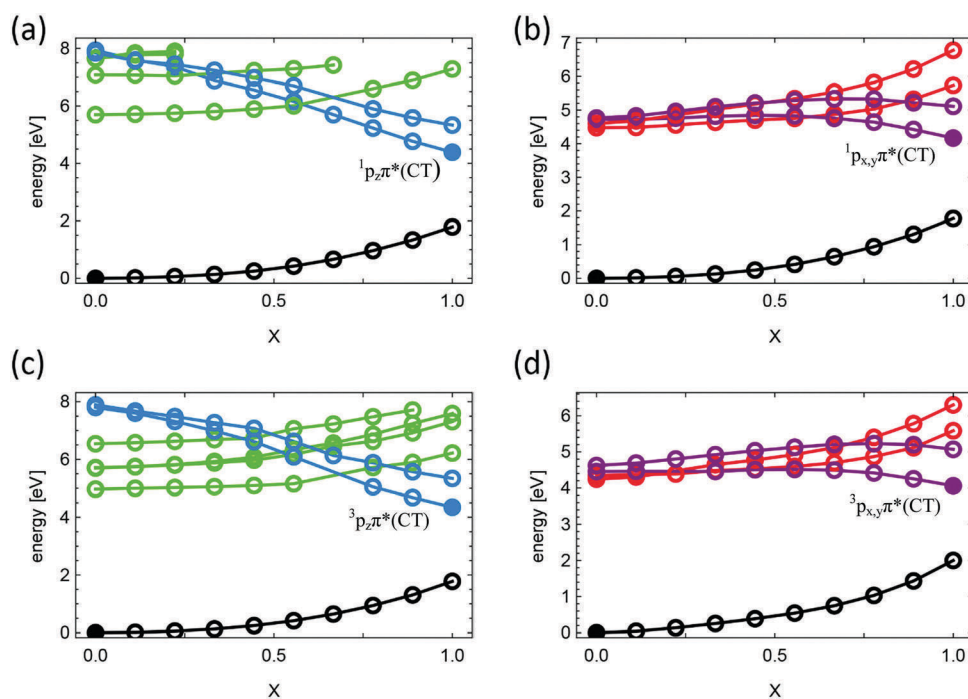


Fig. 5 Energy profiles along the linearly interpolated reaction path (LIRP) labeled by the coordinate X between the ground-state equilibrium geometry ($X = 0.0$) and the optimized geometry of the lowest CT state of the corresponding symmetry at $R_{\text{OH}} = 1.2 \text{ \AA}$. (a) $1A'$ states, (b) $1A''$ states, (c) $3A'$ states, (d) $3A''$ states. Green: $\pi\pi^*(\text{LE})$ states, blue: $p_z\pi^*(\text{CT})$ states, red: $n\pi^*(\text{LE})$ states, purple: $p_{x,y}\pi^*(\text{CT})$ states, black: S_0 state.

p_z orbital of water ($2a''$) to the $5a''$ and $6a''$ π^* orbitals of triazine, respectively. While the charge-transfer states are quasi-degenerate with the highest LE $^1\pi\pi^*$ states in the FC region, they are strongly stabilized in energy along the reaction path. As a result, the energy curves of the two charge-transfer states cross the energy profiles of the locally excited $^1\pi\pi^*$ states along the linearly interpolated reaction path (Fig. 5(a)). The PE profiles for the triplet manifold are similar, except that the locally excited triplet states are lower in energy than the locally excited $^1\pi\pi^*$ states (Fig. 5(c)).

The picture is different for the singlet and triplet states of $n\pi^*(LE)$ and $p_{x,y}\pi^*(CT)$ character, see Fig. 5(b) and (d). Here, the energies of the $p_{x,y}\pi^*(CT)$ states (purple) decrease much less steeply with X than in the $\pi\pi^*$ and $p_z\pi^*$ manifold. Quite different from the curve crossings in Fig. 5(a) and (c), one observes in Fig. 5(b) and (d) a quasi-adiabatic separation of the energies of the locally excited and charge-transfer states along the LIRP.

To understand the reason for the different energy profiles of the $^1,^3p_z\pi^*$ and $^1,^3p_{x,y}\pi^*$ states along the LIRP, it is useful to consider the dependence of the relevant HF orbital energies on the LIRP coordinate X . A survey reveals that the energies of selected occupied π -type orbitals ($2a''$, $3a''$) and n -type orbitals ($21a'$, $22a'$) of triazine and H_2O (see Fig. 2) are particularly sensitive to the reaction coordinate, whereas the energies of the π^* orbitals of triazine ($5a''$, $6a''$) are hardly affected. Fig. 6(a) displays the energies of the second highest π orbital of triazine ($3a''$) and the p_z orbital of water ($2a''$) along the LIRP coordinate X . At $X = 0$ (ground-state equilibrium geometry), the $2a''$ orbital (blue curve in Fig. 6(a)) is located on the water molecule and the $3a''$ orbital (black curve) is the second highest π orbital of triazine. At $X = 1.0$ (equilibrium geometry of the $^1A'$ state at $R_{OH} = 1.2$ Å), the $2a''$ orbital is located on triazine, while the $3a''$ orbital has become the p_z orbital of water. At $X = 0.45$, corresponding to $R_{OH} = 1.09$ Å, the two orbital energies exhibit an avoided crossing, where the character of the adiabatic orbitals switches. The splitting of the $2a''$ and $3a''$ orbital energies at the geometry of closest approach ($X = 0.45$) is a measure of the coupling matrix element of the diabatic orbitals. This coupling is responsible for the electron transfer (from water to triazine) which occurs when the OH bond length of the water molecule is extended by about 0.1 Å. In the $^1,^3p_z\pi^*(CT)$ states the p_z orbital is only singly occupied, as an electron has been transferred to the π^* orbital of triazine. There is thus a hole in the p_z orbital. The increase of the energy of the hole in the p_z orbital from -13.4 eV to -10.1 eV along the LIRP (see Fig. 6(a)) stabilizes the $^1,^3p_z\pi^*(CT)$ state. The reason for the steep decrease of the energy of the $^1,^3p_z\pi^*(CT)$ states along the LIRP in Fig. 5(a) and (c) is thus the increase of orbital energy of the p_z orbital of water.

Among the nonbonding orbitals of the complex, the energies of the orbitals $21a'$ and $22a'$ are most sensitive to the LIRP coordinate X and their energies are shown in Fig. 6(b). The orbital energy curves and the redistribution of the orbital character are different from those of the π orbitals for two reasons. First, there are three nonbonding orbitals of triazine ($19a'$, $21a'$, $22a'$) and there occurs some mixing among these orbitals as a function of X . Second, the $21a'$ nonbonding orbital of triazine already has some density on the oxygen atom of water

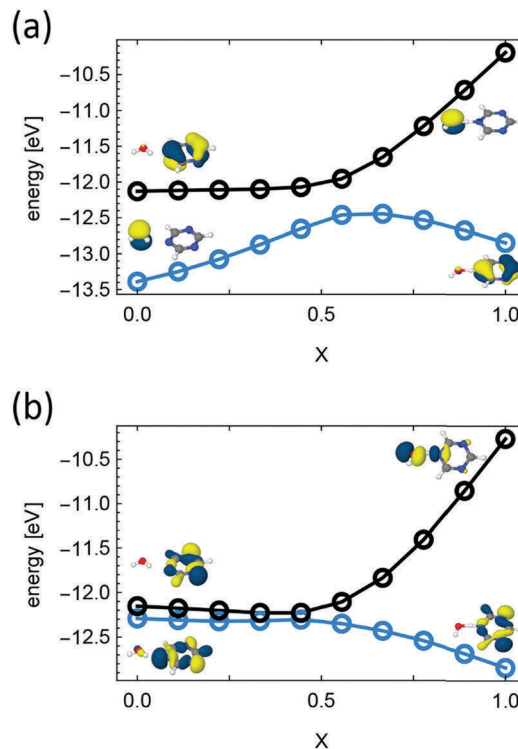


Fig. 6 (a) Orbital energies of the $2a''$ and the $3a''$ orbitals of the triazine water complex along the LIRP between the ground-state equilibrium geometry and the optimized geometry of the $^1p_z\pi^*(CT)$ state at $R_{OH} = 1.2$ Å. (b) Orbital energies of the $21a'$ and the $22a'$ orbitals of the triazine water complex along the LIRP between the ground-state equilibrium geometry and the optimized geometry of the $^1p_{x,y}\pi^*(CT)$ state at $R_{OH} = 1.2$ Å.

at the ground-state equilibrium geometry, see Fig. 2. This partial delocalization of the $21a'$ orbital (which is the nonbonding orbital localized on the N-atom of triazine which is involved in the hydrogen bonding) is responsible for the strong hydrogen bond between triazine and water. When X increases beyond 0.5 (and thus the OH bond length of water increases beyond 1.1 Å), the $21a'$ orbital adiabatically develops into an in-plane p orbital of water, while the $22a'$ orbital remains a nonbonding orbital on triazine, see Fig. 6(b). The higher initial (at $X = 0$) energy of the $p_{x,y}$ orbital of water and the smooth transformation to an n orbital of triazine cause the smooth behavior of the $^1,^3p_{x,y}\pi^*(CT)$ states (Fig. 5(b) and (d)). The different behavior of the orbitals and orbital energies in Fig. 6(a) and (b) is thus the origin of the qualitatively different energy profiles of the $^1,^3p_z\pi^*$ and $^1,^3p_{x,y}\pi^*$ states displayed in Fig. 5.

While a quantitative description of the reaction dynamics of the photoinduced H-atom transfer reaction in the triazine-water complex requires nonadiabatic nuclear dynamics simulations, a qualitative discussion of the photoinduced dynamics can be given on the basis of Fig. 3–6. When higher-lying bright singlet electronic states are excited by absorption of light, it is, according to Kasha's rule, likely that these states relax very rapidly *via* conical intersections to the lowest excited singlet state. Therefore, we will discuss qualitative features of the photoinduced dynamics in terms of the PE surfaces of the lowest excited singlet and triplet states. Fig. 3 confirms that reactive charge-transfer states

exist in all four symmetries ($^1A'$, $^1A''$, $^3A'$ and $^3A''$). While the singlet states can be directly excited by absorption of light, the triplet states can only be indirectly populated by spin-orbit induced intersystem crossing processes. Typical intersystem-crossing rates in N-heterocycles are of the order of hundreds of picoseconds to nanoseconds. When hydrogen-transfer barriers on singlet PE surfaces are low, intersystem crossing cannot compete and the H-atom transfer reaction will occur on the singlet PE surface. When the H-atom transfer barrier is substantial, on the other hand, as for the $^1A''$ surface of the triazine-water complex, intersystem crossing may compete effectively with the H-atom transfer reaction on the singlet surface. Therefore, it is important to know that low-barrier reaction paths for H-atom transfer exist also on the triplet surfaces.

The energy curve of the lowest charge-transfer state of A' symmetry ($^1p_z\pi^*(CT)$) crosses the energy curve of the closed-shell S_0 state along the H-atom transfer coordinate near $R_{OH} = 1.8 \text{ \AA}$ (Fig. 3(a)). This crossing is nominally an avoided crossing, whereas the crossing is a symmetry-allowed crossing for the $^1p_{x,y}\pi^*(CT)$ state of $^1A''$ symmetry. In both cases, there exists a conical intersection of the PE surface of the lowest charge-transfer state with the PE surface of the S_0 state. The nonadiabatic dynamics at this conical intersection controls whether a biradical is formed (successful H-atom transfer) or radiationless relaxation to the electronic ground state of the triazine-H₂O complex occurs (aborted H-atom transfer). For the $^3p_z\pi^*(CT)$ and $^3p_{x,y}\pi^*(CT)$ PE surfaces, the crossings with the PE surface of the S_0 state are allowed crossings when spin-orbit (SO) coupling can be neglected. Wave packets on the triplet PE surfaces will thus cross the intersection with the S_0 surface essentially without perturbation, while wave packets on the singlet surfaces may bifurcate into a reactive component (yielding free radicals) and a nonreactive component (yielding the original complex in the S_0 state).

The bright states of triazine are too high in energy to be relevant for solar applications, but the lower-lying excited states can borrow intensity from the former and thus can be populated by the absorption of near-UV photons. The ensuing excited-state dynamics can qualitatively be discussed by reference to the two-dimensional PE surfaces of the lowest excited states of each symmetry which are shown in Fig. 4. The lowest barrier between the minimum of the locally excited state and the corresponding charge-transfer minimum is found for the $^1A'$ surface (0.2 eV, Fig. 4(a)). For the singlet and triplet A'' surfaces, the barriers are highest ($\approx 0.6 \text{ eV}$) due to the larger vibrational stabilization energies of the locally excited $n\pi^*$ states (Fig. 4(b) and (d)). On the other hand, the energies of the saddle points of the A'' states are more than 1.0 eV lower than those of the A' states. For the singlet states, the barriers for H-atom transfer are below the vertical excitation energies. The photoinduced H-atom transfer reaction is thus nominally barrierless in the singlet excited states, in sharp contrast to the H-atom transfer reaction in the electronic ground state of the complex, which exhibits a barrier of more than two electron volts.

It should be mentioned that triazine, like benzene,^{43,44} pyridine,⁴⁵ pyrazine,⁴⁴ pyrimidine⁴⁶ and other six-membered heterocycles, *e.g.* DNA/RNA pyrimidine bases,⁴⁷ is generically

labile with respect to out-of-plane deformation in the $^1\pi\pi^*$ excited states. As is well known,⁴³⁻⁴⁷ low-barrier reaction paths for out-of-plane deformation of the six-membered aromatic rings exist which lead to conical intersections of the $^1\pi\pi^*$ states with lower $^1n\pi^*$ states and the S_0 state. The conical intersections promote rapid radiationless deactivation of the $^1\pi\pi^*$ states on femtosecond to picosecond time scales. These intrinsic excited-state deactivation processes of triazine were not investigated in the present work. Due to the rapid excited-state quenching mechanisms, triazine cannot be expected to be an efficient photocatalyst for water splitting. On the other hand, excited-state quenching by out-of-plane deformation is strongly suppressed in fused heterocycles, such as, *e.g.*, heptazine. It has indeed been shown that melamine (triaminotriazine) has an excited state lifetime of just 13 ps⁴⁸ and is nonfluorescent, while melem (triaminoheptazine) is fluorescent with a nanosecond excited-state lifetime.⁴⁹ Melem is thus clearly a better chromophore for photochemical water splitting than melamin.⁴⁹ The rather good water-splitting efficiencies found with triazine-based covalent organic frameworks¹⁴⁻²⁴ indicate that the intrinsic excited-state deactivation mechanisms of triazine are suppressed in these supramolecular structures.

B. H-Atom photodetachment from the triazinyl radical

The ground-state equilibrium geometry of the triazinyl radical is planar and its NH distance is $R_{NH} = 1.012 \text{ \AA}$ at the unrestricted MP2 (UMP2) level with the aug-cc-pVDZ basis set. The frontier canonical unrestricted HF (UHF) orbitals of the triazinyl radical are shown in Fig. 7. The highest doubly occupied orbital is a nonbonding orbital ($18a'$) and the singly occupied orbital is a π orbital ($4a''$). Orbital $5a''$ is the lowest unoccupied π orbital. The lowest unoccupied orbital ($19a'$) is a so-called σ^* orbital of the NH bond. Like the σ^* orbitals of the NH bonds of pyrrole or indole,⁵⁰ it is diffuse (Rydberg like), antibonding with respect to the NH bond and localized mostly outside the aromatic ring. The occupation of this orbital provides the driving force for the dissociation of the NH bond.⁵⁰

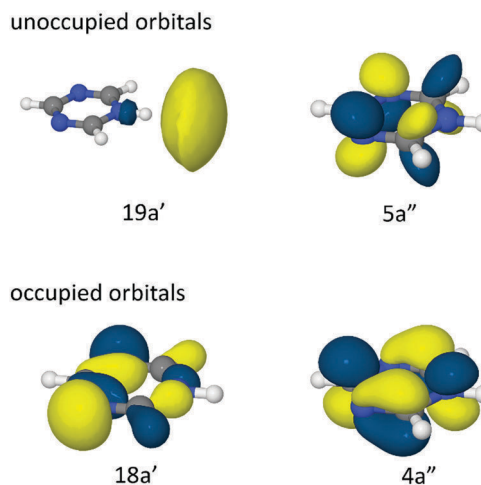


Fig. 7 Frontier Hartree-Fock orbitals of the triazinyl radical at the ground-state equilibrium geometry.

The triazinyl radical has a dense set of excited states. The vertical excitation energies of the ten lowest excited states are given in Table SV of the ESI.† They are all dark states or have very low oscillator strengths. The lowest ${}^2\pi\pi^*$ excited state is found at 1.81 eV at the unrestricted ADC(2) (UADC(2)) level with an oscillator strength of 0.003. The lowest ${}^2\pi\sigma^*$ excited state is found about 1.0 eV higher in energy with zero oscillator strength. The lowest excited state with significant oscillator strength is at 5.75 eV with $f = 0.033$, from which the lower states can borrow intensity by vibronic coupling.

We calculated the energy profiles of the ground state and the lowest excited states of the triazinyl radical by a rigid scan along the NH stretching coordinate. Optimization of the energy with respect to the other internal nuclear coordinates is of minor importance in this case. The PE functions obtained with the UADC(2) method are shown in Fig. 8(a) for the ground state (black), the lowest ${}^2\pi\pi^*$ state (green) and the lowest ${}^2\pi\sigma^*$ state (blue). While the PE functions of the ${}^2\pi\pi^*$ states and the ${}^2n\pi^*$ states (the latter are not included in Fig. 8 for clarity) are bound with respect to the NH stretching coordinate, the PE function of the ${}^2\pi\sigma^*$ state is dissociative with a very low dissociation energy of 2.7 eV at the UADC(2) level. The PE curve of the ${}^2\pi\sigma^*$ state crosses the PE curve of the electronic ground state at an NH distance of 1.6 Å, see Fig. 8(a), and dissociates towards triazine and an H-atom in their electronic ground states.

Because the single-reference UADC(2) method has not yet been extensively tested for dissociation reactions of open-shell

systems, we recalculated the PE functions of the triazinyl radical with the CASPT2 method. Details of the CASSCF and CASPT2 calculations are given in Section I of the ESI.† Fig. 8(b) shows the PE profiles of the ground state (black), the lowest ${}^2\pi\pi^*$ state (green) and the reactive ${}^2\pi\sigma^*$ state (blue) calculated with the CASPT2 method. The crossing of the energy curve of the reactive ${}^2\pi\sigma^*$ state with the energy curve of the D_0 state occurs at 1.54 Å. The dissociation energy is 2.0 eV, which is about 0.7 eV lower than the dissociation energy calculated with the UADC(2) method. Due to the multi-configurational character of the electronic wave functions for large OH distances, we adopt the CASPT2 data for further discussion (see Section VI of the ESI† for more details).

The ${}^2\pi\sigma^*$ state of the triazinyl radical is dark and therefore cannot be excited directly with light from the electronic ground state. It can be populated either by vibronic intensity borrowing from higher allowed ${}^2\pi\pi^*$ states or by optical excitation of these higher allowed states, followed by internal conversion to the reactive ${}^2\pi\sigma^*$ state. The radical can then dissociate on the ${}^2\pi\sigma^*$ PE surface through two conical intersections involving the lowest ${}^2\pi\pi^*$ state and the D_0 state, see Fig. 8. This mechanism opens a channel for fast and non-statistical H-atom photodissociation, analogous to the well-known photodissociation reactions of pyrrole, indole or aniline.^{51–55} By this photodetachment reaction, the triazine molecule is recovered and, thus, becomes a photocatalyst.

As discussed previously for the pyridinyl radical³⁷ and the heptazinyl radical,⁴⁰ there exists an alternative scenario for the harvesting of the H-atoms which have been abstracted from water by the photoexcited chromophore. Due to the exceptionally low dissociation energy of the triazinyl radical (2.0 eV), two triazinyl radicals can recombine in a dark reaction to yield H_2 (formation energy 4.6 eV), thereby regenerating two triazine molecules. In this scenario, two water molecules are decomposed into H_2 and two OH radicals by the absorption of two photons. This second scenario requires that the chromophores are mobile and may apply when small oligomers of triazine or other heterocycles are used as photocatalysts.^{30,31}

III. Conclusions

The hydrogen-bonded complex of triazine with a single water molecule was chosen as a model system for the exploration of the photochemistry of the triazine chromophore in an aqueous environment. The nitrogen atoms of triazine are H-atom acceptors in the hydrogen-bonding with water. The hydrogen bond between triazine and the H_2O molecule plays an important role in the photochemistry of the complex. Essential features of the multi-dimensional excited-state PE surfaces of the triazine–water complex were characterized by the computation of the PE profiles of minimum-energy paths as well as by the computation of two-dimensional relaxed PE surfaces for the lowest A'' and A' excited states in the singlet and triplet manifolds. The results provide evidence that photoexcited triazine can abstract a hydrogen atom from the water molecule *via* an electron-driven

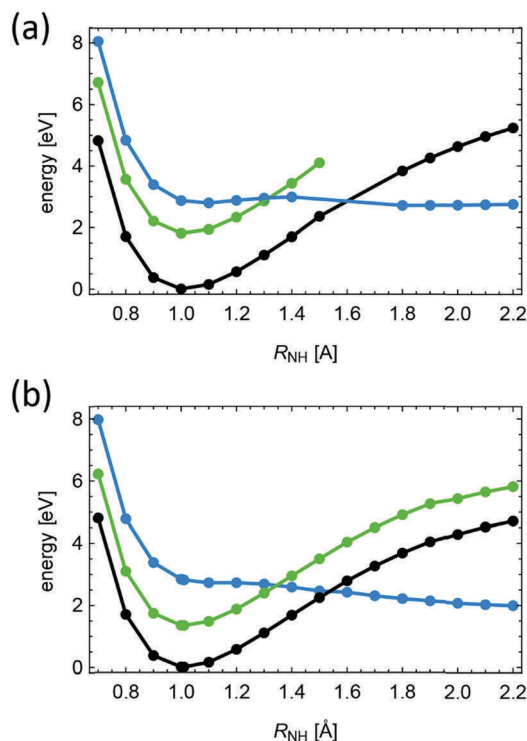


Fig. 8 PE functions of the triazinyl radical along the NH-stretching coordinate calculated with (a) the unrestricted ADC(2) method and (b) the CASPT2 method. Black: ground state (D_0), green: ${}^2\pi\pi^*$ state, blue: ${}^2\pi\sigma^*$ state.

proton-transfer process. In contrast to the H-atom transfer reaction in the electronic ground state, which involves a barrier of more than 2 eV, the barriers on the excited-state PE surfaces are of the order of a few tenths of an electron volt. For the $1^1A'$ and $1^1A''$ excited-state PE surfaces of the triazine–H₂O complex, the saddle points of the H-atom transfer reaction are below the vertical electronic excitation energies. The yield of the reaction thus depends on the competition of intramolecular vibrational relaxation (IVR) in the locally excited states with H-atom transfer. Due to the low mass of the H-atom compared to the effective masses of most other vibrational degrees of freedom, there is a good chance that H-atom transfer competes efficiently with energy dissipation by IVR. The photoreaction yields triazinyl and OH radicals in their electronic ground states, which therefore are photophysically stable species. About 2.8 eV of the energy of the absorbed photon are stored as chemical energy in the radical pair.

Insight into the detailed mechanism of the excited-state H-atom transfer reaction has been obtained by the investigation of the wave functions and energies of the relevant molecular orbitals of the complex. It is found that fluctuations of the OH bond length of the hydrogen-bonded water molecule of the order of 0.1 Å are sufficient to trigger a hole transfer from the second-highest (N-centered) π orbital of triazine to the p_z orbital on the oxygen atom of water, which oxidizes the water molecule. The resulting $^1p_z\pi^*$ CT state is strongly stabilized in energy by the transfer of the proton from the water molecule to triazine. The excess energy of about 2 eV is sufficient to break the hydrogen bond of the radical pair, yielding free triazinyl and hydroxyl radicals. In the $^1n\pi^*$ excited states, a similar hole transfer from triazine to water happens, but the transformation of the orbitals is more gradual (adiabatic) than in the $^1\pi\pi^*$ states.

The photoreactivity of the triazinyl radical was explored by the computation of the vertical excitation energies and excited-state energy profiles for the dissociation of the NH bond. The second-lowest excited state of the triazinyl radical is a so-called $\pi\sigma^*$ state which is dissociative with respect to the NH bond, giving rise to an exceptionally low dissociation energy (2.0 eV) of the triazinyl radical. The predissociation of the bound $^2\pi\pi^*$ and $^2n\pi^*$ excited states of the triazinyl radical opens a channel for fast (non-statistical) photodissociation. The photodetachment of the H-atom from the triazinyl radical regenerates the triazine chromophore and thus closes the catalytic cycle. Overall, the hydrogen-bonded water molecule is decomposed into H and OH radicals in a biphotonic photochemical reaction. In this scenario, two photons are absorbed by a single chromophore and each photon promotes a fast (femtosecond) H-atom transfer or H-atom detachment reaction.

The catalytic cycle can alternatively be closed by the exothermic recombination of two triazinyl radicals to yield molecular hydrogen in a dark reaction, thereby regenerating two triazine molecules. In this second scenario, two different chromophores absorb a photon and each of them abstracts an H-atom from a hydrogen-bonded water molecule, yielding two triazinyl radicals and two OH radicals. While free H radicals are generated in the first scenario, H₂ molecules are produced in the second scenario.

The *in situ* detection of free H radicals could thus discriminate between the two scenarios.

In both scenarios free OH radicals are produced. Free OH radicals have already been detected in hydrogen evolution experiments with graphitic carbon-nitride materials, either with ESR spectroscopy using DMPO as a spin-trap,⁵⁶ or *via* fluorescence detection of hydroxylated OH radical scavengers, *e.g.* terephthalic acid.⁵⁷ The free OH radicals can recombine and form H₂O₂ in an exothermic reaction when colloidal platinum is present as a catalyst. H₂O₂ is the stable waste product of the water-splitting reaction. It can be decomposed into O₂ and H₂O in an exothermic reaction using manganese-oxide as a catalyst.

The mechanism of photoinduced water splitting described herein for the triazine–water complex is basically the same as described previously for the pyridine–water complex.^{37,38} However, triazine possesses a denser spectrum of excited states and these states are at lower energies than in pyridine. Although the low-lying $^1n\pi^*$ states of triazine have low electronic transition dipole moments, the absorption intensities induced by vibronic coupling with higher lying bright $^1\pi\pi^*$ states should be sufficient for effective light absorption in condensed materials, such as linear polymers or two-dimensional organic frameworks. We suggest that the photochemical mechanism proposed herein provides an explanation of the experimentally observed significant increase of the photocatalytic activity for H₂ evolution with increasing nitrogen content of carbon nitride materials.^{20,22}

Conflicts of interest

There are no conflicts to declare.

Acknowledgements

J. E. has been supported by the DFG cluster of Excellence “Munich Centre for Advanced Photonics” and the International Max Planck Research School of Advanced Photon Science (IMPRS-APS). M. J. J. acknowledges support within the “Diamond Grant” (0144/DIA/2017/46) from the Polish Ministry of Science and Higher Education. A. L. S. acknowledges support by the Alexander von Humboldt Research Award.

References

- X. Wang, K. Maeda, A. Thomas, K. Takanabe, G. Xin, J. M. Carlsson, K. Domen and M. Antonietti, *Nat. Mater.*, 2009, **8**, 76–80.
- Y. Wang, X. Wang and M. Antonietti, *Angew. Chem., Int. Ed.*, 2012, **51**, 68–89.
- A. Schwarzer, T. Saplinova and E. Kroke, *Coord. Chem. Rev.*, 2013, **257**, 2032–2062.
- S. Cao, J. Low, J. Yu and M. Jaroniec, *Adv. Mater.*, 2015, **27**, 2150–2176.
- T. S. Miller, A. B. Jorge, T. M. Suter, A. Sella, F. Cora and P. F. McMillan, *Phys. Chem. Chem. Phys.*, 2017, **19**, 15613–15638.

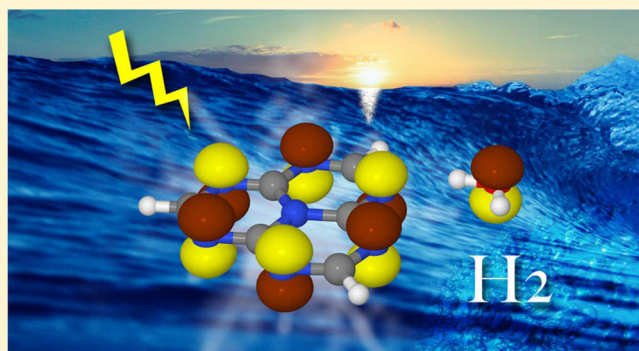
- 6 S. Ilic, M. R. Zoric, U. P. Kadel, Y. Huang and K. D. Glusac, *Annu. Rev. Phys. Chem.*, 2017, **68**, 305–331.
- 7 J. Wen, J. Xie, X. Chen and X. Li, *Appl. Surf. Sci.*, 2017, **391**, 72–123.
- 8 J. von Liebig, *Ann. Pharm.*, 1834, **10**, 1–47.
- 9 K. Schwinghammer, B. Tuffy, M. B. Mesch, E. Wirnhier, C. Martineau, F. Taulelle, W. Schnick, J. Senker and B. V. Lotsch, *Angew. Chem., Int. Ed.*, 2013, **52**, 2435–2439.
- 10 K. Schwinghammer, M. B. Mesch, V. Duppel, C. Ziegler, J. Senker and B. V. Lotsch, *J. Am. Chem. Soc.*, 2014, **136**, 1730–1733.
- 11 G. Algara-Siller, N. Severin, S. Y. Chong, T. Björkman, R. G. Palgrave, A. Laybourn, M. Antonietti, Y. Z. Khimiyak, A. V. Krashennnikov, J. P. Rabe, U. Kaiser, A. I. Cooper, A. Thomas and M. J. Bojdys, *Angew. Chem., Int. Ed.*, 2014, **53**, 7450–7455.
- 12 J. Bi, W. Fang, L. Li, J. Wang, S. Liang, Y. He, M. Liu and L. Wu, *Macromol. Rapid Commun.*, 2015, **36**, 1799–1805.
- 13 M. K. Bhunia, S. Melissen, M. R. Parida, P. Sarawade, J.-M. Basset, D. H. Anjum, O. F. Mohammed, P. Sautet, T. L. Bahers and K. Takane, *Chem. Mater.*, 2015, **27**, 8237–8247.
- 14 L. Lin, C. Wang, W. Ren, H. Ou, Y. Zhang and X. Wang, *Chem. Sci.*, 2017, **8**, 5506–5511.
- 15 T. Shibata, A. Kabumoto, T. Shiragami, O. Ishitani, C. Pac and S. Yanagida, *J. Phys. Chem.*, 1990, **94**, 2068–2076.
- 16 S. Matsuoka, T. Kohzuki, Y. Kuwana, A. Nakamura and S. Yanagida, *J. Chem. Soc., Perkin Trans. 2*, 1992, 679–685.
- 17 P. Kuhn, M. Antonietti and A. Thomas, *Angew. Chem., Int. Ed.*, 2008, **47**, 3450–3453.
- 18 M. J. Bojdys, J. Jeromenok, A. Thomas and M. Antonietti, *Adv. Mater.*, 2010, **22**, 2202–2205.
- 19 S. Ren, M. J. Bojdys, R. Dawson, A. Laybourn, Y. Z. Khimiyak, D. J. Adams and A. I. Cooper, *Adv. Mater.*, 2012, **24**, 2357–2361.
- 20 V. S. Vyas, F. Haas, L. Stegbauer, G. Savasci, F. Podjaski, C. Ochsenfeld and B. V. Lotsch, *Nat. Commun.*, 2015, **6**, 8508.
- 21 L. Li, W. Fang, P. Zhang, J. Bi, Y. He, J. Wang and W. Su, *J. Mater. Chem. A*, 2016, **4**, 12402–12406.
- 22 V. S. Vyas, V. W. Lau and B. V. Lotsch, *Chem. Mater.*, 2016, **28**, 5191–5204.
- 23 S. Kuecken, A. Acharjya, L. Zhi, M. Schwarze, R. Schomäcker and A. Thomas, *Chem. Commun.*, 2017, **53**, 5854–5857.
- 24 C. B. Meier, R. S. Sprick, A. Monti, P. Guiglion, J.-S. M. Lee, M. A. Zwijnenburg and A. I. Cooper, *Polymer*, 2017, **126**, 283–290.
- 25 W. Wei and T. Jacob, *Phys. Rev. B: Condens. Matter Mater. Phys.*, 2013, **87**, 085202.
- 26 C. Merschjann, T. Tyborski, S. Orthmann, F. Yang, K. Schwarzburg, M. Lublow, M.-C. Lux-Steiner and T. Schedel-Niedrig, *Phys. Rev. B: Condens. Matter Mater. Phys.*, 2013, **87**, 205204.
- 27 S. Melissen, T. Le Bahers, S. N. Steinmann and P. Sautet, *J. Phys. Chem. C*, 2015, **119**, 251188.
- 28 G. A. Meek, A. D. Baczewski, D. J. Little and B. G. Levine, *J. Phys. Chem. C*, 2014, **118**, 4023–4032.
- 29 C. Merschjann, S. Tschierlei, T. Tyborski, K. Kailasam, S. Orthmann, D. Hollmann, T. Schedel-Niedrig, A. Thomas and S. Lochbrunner, *Adv. Mater.*, 2015, **27**, 7993–7999.
- 30 S. Yanagida, T. Ogata, Y. Kuwana, Y. Wada, K. Murakoshi, A. Ishida, S. Takamuku, M. Kusaba and N. Nakashima, *J. Chem. Soc., Perkin Trans. 2*, 1996, 1963–1969.
- 31 K. Schwinghammer, S. Hug, M. B. Mesch, J. Senker and B. V. Lotsch, *Energy Environ. Sci.*, 2015, **8**, 3345–3353.
- 32 K. Srinivasu, B. Modak and S. K. Ghosh, *J. Phys. Chem. C*, 2014, **118**, 26479–26484.
- 33 X. Jiang, P. Wang and J. Zhao, *J. Mater. Chem. A*, 2015, **3**, 7750–7758.
- 34 K. Srinivasu, B. Modak and S. K. Ghosh, *Phys. Chem. Chem. Phys.*, 2016, **18**, 26466–26474.
- 35 C. Butchosa, T. O. McDonald, A. I. Cooper, D. J. Adams and M. A. Zwijnenburg, *J. Phys. Chem. C*, 2014, **118**, 4314–4324.
- 36 K. Srinivasu and S. K. Ghosh, *J. Mater. Chem. A*, 2015, **3**, 23011–23016.
- 37 X. Liu, A. L. Sobolewski, R. Borrelli and W. Domcke, *Phys. Chem. Chem. Phys.*, 2013, **15**, 5957–5966.
- 38 X. Liu, A. L. Sobolewski and W. Domcke, *J. Phys. Chem. A*, 2014, **118**, 7788–7795.
- 39 X. Liu, T. N. V. Karsili, A. L. Sobolewski and W. Domcke, *J. Phys. Chem. B*, 2015, **119**, 10664–10672.
- 40 J. Ehrmaier, T. N. V. Karsili, A. L. Sobolewski and W. Domcke, *J. Phys. Chem. A*, 2017, **121**, 4754–4764.
- 41 I. C. Walker, M. H. Palmer and C. C. Ballard, *Chem. Phys.*, 1992, **167**, 61–75.
- 42 D. M. P. Holland, D. A. Shaw, M. Stener, P. Decleva and S. Coriani, *Chem. Phys.*, 2016, **477**, 96–104.
- 43 I. J. Palmer, I. N. Ragazos, F. Bernardi, M. Olivucci and M. A. Robb, *J. Am. Chem. Soc.*, 1993, **115**, 673–682.
- 44 A. L. Sobolewski, C. Woywod and W. Domcke, *J. Chem. Phys.*, 1993, **98**, 5627–5641.
- 45 P. C. Varras, P. S. Gritzapis and K. C. Fylaktakidou, *Mol. Phys.*, 2018, **116**, 154–170.
- 46 S. Franzen, B. Skalski, L. Bartolotti and C. Delley, *Phys. Chem. Chem. Phys.*, 2014, **16**, 20164–20174.
- 47 R. Improta, F. Santoro and L. Blancafort, *Chem. Rev.*, 2016, **116**, 3540–3593.
- 48 Y. Zhang, A. A. Beckstead, Y. Hu, X. Piao, D. Bong and B. Kohler, *Molecules*, 2016, **21**, 1645.
- 49 J. Wen, R. Li, R. Lu and A. Yu, *Chem. – Asian J.*, 2018, **13**, 1060–1066.
- 50 A. L. Sobolewski, W. Domcke, C. Dedonder-Lardeux and C. Jouvet, *Phys. Chem. Chem. Phys.*, 2002, **4**, 1093–1100.
- 51 M. N. R. Ashfold, B. Cronin, A. L. Devine, R. N. Dixon and M. G. D. Nix, *Science*, 2006, **312**, 1637–1640.
- 52 M. N. R. Ashfold, G. A. King, D. Murdock, M. G. D. Nix, T. A. A. Oliver and A. Sage, *Phys. Chem. Chem. Phys.*, 2010, **12**, 1218–1238.
- 53 G. M. Roberts and V. G. Stavros, *Chem. Sci.*, 2014, **5**, 1698–1722.
- 54 R. Spesyvtsev, O. M. Kirkby and H. H. Fielding, *Faraday Discuss.*, 2012, **157**, 165–179.
- 55 G. M. Roberts, C. A. Williams, J. D. Young, S. Ullrich, M. J. Paterson and V. G. Stavros, *J. Am. Chem. Soc.*, 2012, **134**, 12578–12589.
- 56 K. Huang, Y. Hong, X. Yan, C. Huang, J. Chen, M. Chen, W. Shi and C. Liu, *CrystEngComm*, 2016, **18**, 6453–6463.
- 57 P. Niu, L. Zhang, G. Liu and H.-M. Cheng, *Adv. Funct. Mater.*, 2012, **22**, 4763–4770.

Mechanism of Photocatalytic Water Splitting with Graphitic Carbon Nitride: Photochemistry of the Heptazine–Water Complex

Johannes Ehrmaier,^{*,†} Tolga N. V. Karsili,^{†,§} Andrzej L. Sobolewski,[‡] and Wolfgang Domcke^{*,†}[†]Department of Chemistry, Technical University of Munich, Garching, Germany[‡]Institute of Physics, Polish Academy of Sciences, Warsaw, Poland[§]Department of Chemistry, Temple University, Philadelphia, Pennsylvania 19122, United States

S Supporting Information

ABSTRACT: Impressive progress has recently been achieved in photocatalytic hydrogen evolution with polymeric carbon nitride materials consisting of heptazine building blocks. However, the fundamental mechanistic principles of the catalytic cycle are as yet poorly understood. Here, we provide first-principles computational evidence that water splitting with heptazine-based materials can be understood as a molecular excited-state reaction taking place in hydrogen-bonded heptazine–water complexes. The oxidation of water occurs homolytically via an electron/proton transfer from water to heptazine, resulting in ground-state heptazinyl and OH radicals. It is shown that the excess hydrogen atom of the heptazinyl radical can be photodetached by a second photon, which regenerates the heptazine molecule. Alternatively to the photodetachment reaction, two heptazinyl radicals can recombine in a dark reaction to form H₂, thereby regenerating two heptazine molecules. The proposed molecular photochemical reaction scheme within hydrogen-bonded chromophore–water complexes is complementary to the traditional paradigm of photocatalytic water splitting, which assumes the separation of electrons and holes over substantial time scales and distances.



1. INTRODUCTION

Melon, first reported by Justus von Liebig in 1834, is a polymer of nominal composition C₆N₉H₃ which is easily prepared from inexpensive precursors.¹ In 2009, Antonietti, Domen and co-workers reported hydrogen evolution from water with visible light, using melon as photocatalyst together with a sacrificial electron donor.² In recent years, photocatalytic water splitting with melon or related polymers, collectively referred to as polymeric or graphitic carbon nitrides and schematically abbreviated as C₃N₄, has become a remarkably vibrant field of research (see, for example, refs 3–13 and references therein). The chemical compositions and molecular structures of the carbon nitride materials depend on the details of their preparation and are therefore not precisely defined. It is generally agreed that C₃N₄ materials are amorphous or partially crystalline polymers consisting of *s*-triazine¹⁴ or heptazine (tri-*s*-triazine)¹ building blocks connected by N atoms or NH groups. Melon and related triazine or heptazine based polymeric materials are in general not pure carbon nitrides but may contain varying amounts of hydrogen.

The mechanism of the photoinduced water-splitting reaction catalyzed by polymeric C₃N₄ materials is currently not fully understood. In the framework of the widely accepted paradigms of photoelectrochemical water splitting,^{15–19} C₃N₄ is generally considered as a semiconductor, and the photoinduced water-splitting reaction is described in terms of exciton generation by

UV/vis light absorption, followed by exciton dissociation, migration of charge carriers (electrons and holes) to solid/liquid interfaces, where the neutralization of protons and the oxidation of water take place with suitable catalysts.^{1–13} The thermodynamic stability of various forms of g-C₃N₄ has been characterized with density functional theory (DFT) calculations.^{20,21} The band structures of monolayer and few-layer graphitic C₃N₄ (g-C₃N₄) materials have been calculated with periodic DFT calculations.^{22–25} Cluster models of triazine and heptazine oligomers also have been considered, and the effects of corrugation on the electronic structure and the optical spectra have been explored.^{26–30} The effects of chemical modifications of the monomers and doping of the polymers have been modeled with DFT calculations.^{31,32} The redox potentials of electrons and holes in heptazine oligomers were estimated within a continuum model of aqueous solvation by Zwijnenburg and co-workers.²⁸ In a few studies, the adsorption of water molecules on heptazine units and possible (endothermic) reactions of water molecules with heptazine in the electronic ground state were investigated.^{33–35} To the knowledge of the authors, no computational studies of the reactivity of photoexcited C₃N₄ with water molecules exist.

Received: May 12, 2017

Revised: June 7, 2017

Published: June 7, 2017

There are a number of indications that the optical and the photocatalytic properties of heptazine-based polymeric materials may be determined more by the properties of single heptazine units than the mesoscopic structure of the materials. Heptazine-based polymeric C_3N_4 materials exhibit, for example, strong photoluminescence upon near-UV excitation which has all the characteristics of molecular fluorescence. As pointed out by Merschjann et al., the material seems to behave as a monomer as far as its optical properties are concerned.³⁶ It has also been reported that amorphous forms of carbon nitride materials exhibit a higher hydrogen evolution activity than more crystalline polymers,³⁷ which is a clear indication that long-range mobility of charge carriers is not a decisive factor for the catalytic activity. Recently, Lotsch and co-workers investigated the photocatalytic hydrogen-evolution activity of heptazine polymers of different chain lengths, using nanoscale platinum as cocatalyzer and methanol as sacrificial electron donor. It was shown that fractions of low molecular weight, containing mainly small heptazine oligomers, were considerably more efficient photocatalysts than polymeric melon.³⁸ Moreover, chemically modified heptazine units and oligomers thereof were shown to exhibit up to 16 times higher H_2 evolution rates than standard melon.³⁹ These findings strongly suggest that photoinduced hydrogen evolution by $g-C_3N_4$ materials may be better described as a photochemical reaction of single heptazine units or small heptazine oligomers with water than as a charge-separation process on mesoscopic scales followed by multielectron redox reactions at solid/liquid interfaces.

Herein, we provide first-principles computational evidence that photoinduced water splitting by heptazine-based molecular or polymeric materials indeed is a molecular photochemical reaction in hydrogen-bonded complexes of the heptazine ($C_6N_7H_3$) chromophore with water molecules. Our results reveal that the peripheral N-heteroatoms of heptazine are the active sites for the photochemical reaction of heptazine with water. It is shown that the primary photochemical reaction is initiated by an electron transfer from a hydrogen-bonded water molecule to the photoexcited heptazine molecule. The partially vacant highest occupied molecular orbital (HOMO) in the lowest $^1\pi\pi^*$ excited state of heptazine is able to suck an electron from the lone pair p-orbital on the oxygen atom of the hydrogen-bonded water molecule. This electron transfer in turn triggers an ultrafast proton transfer from the water molecule to the acceptor N atom of heptazine (the proton follows the electron). The result of this electron-driven proton transfer (EDPT) reaction,⁴⁰ also known as proton-coupled electron transfer (PCET) reaction in the literature,⁴¹ are two neutral radicals, $C_6N_7H_4$ and OH, in their electronic ground states. The hydrogen-bonded water molecule is thus oxidized to an OH radical.

Because of the localization of the water-oxidation reaction on a single N atom, the essence of the photochemical reaction can be revealed by considering, in a first approximation, the hydrogen-bonded complex of a single heptazine molecule with a single water molecule. While solvation of the heptazine–water complex and the $C_6N_7H_4$ –OH radical pair by an aqueous environment may lead to quantitative modifications of the electronic excitation spectra and the excited-state reactivity, the basic principles of the reaction can be explored for this most simple model system. In particular, the small size of this system allows us to employ accurate ab initio wave function methods for the characterization of the excited-state potential-energy

(PE) surfaces, which have not been explored so far for any model of photoinduced $g-C_3N_4$ reactivity with water. The ambiguities of DFT concerning the fundamental band gap and the optical band gap⁴² can thus be avoided. The ab initio single-reference electronic-structure method (ADC(2)) employed in the present work has been benchmarked in earlier work against more accurate multiconfiguration self-consistent field (MCSCF) and multireference perturbation theory (MRPT) data for a computationally more amenable model system, the pyridine–water complex.^{43,44} The dielectric screening effects of an aqueous environment are estimated in the present work by a polarized continuum model.

2. COMPUTATIONAL METHODS

The ground-state equilibrium geometry of the heptazine– H_2O complex was determined with the second-order Møller–Plesset (MP2) method. Dunning's augmented correlation-consistent split-valence double- ζ basis set with polarization functions on all atoms (aug-cc-pVDZ)⁴⁵ was employed in the MP2 calculations.

Excitation energies, excited-state reaction paths, and energy profiles were calculated with the second-order algebraic-diagrammatic-construction (ADC(2)) method.^{46,47} ADC(2) is a variant of propagator theory and is closely related to the approximate second-order singles-and-doubles coupled-cluster (CC2) method, which is a widely used computationally efficient variant of coupled-cluster theory for excited states.⁴⁸ An advantage of the ADC(2) method compared to the CC2 method is the feature that the excitation energies are calculated as the eigenvalues of a Hermitian matrix. While the vertical excitation energies obtained with the CC2 and ADC(2) methods are generally very similar, the ADC(2) method is more stable in the vicinity of excited-state energy crossings and is able to describe the topography of conically intersecting potential energy surfaces of excited states physically correctly.^{49,50} The accuracy of ADC(2) excitation energies has been benchmarked for a large set of aromatic organic molecules.^{51–53} The excitation energies of $^1\pi\pi^*$ states calculated with the ADC(2) method and the cc-pVDZ basis set are expected to be systematically too high by a few tenths of an electronvolt. For the heptazynyl radical, the unrestricted version of ADC(2)⁵⁴ was employed. A recent investigation of the performance of the unrestricted ADC(2) method for a representative test set of organic radicals has shown that the unrestricted ADC(2) method is a reliable alternative to coupled-cluster-based approaches for the calculation of excited states of medium-size open-shell molecules.⁵⁴ The ADC(2) calculations also yield reliable electronic transition dipole moments and oscillator strengths.

For the pyridine–water complex and the pyridinyl radical, the PE surfaces obtained with the ADC(2) method have been benchmarked against accurate complete-active-space self-consistent-field (CASSCF) and CASPT2 (second-order perturbation theory with respect to the CASSCF reference) calculations.^{43,44} For the heptazine–water complex and the heptazynyl radical, the calculation of accurate CASSCF/CASPT2 excitation energies is not possible, since the size of the active orbital space cannot be extended as would be required for these larger systems. The aug-cc-pVDZ basis set was employed in all calculations of excited states. The augmentation is necessary for the description of the $^2\pi\sigma^*$ excited states of the heptazine radicals which exhibit diffuse Rydberg character at the ground-state equilibrium geometry.

The reaction path for the transfer of a proton from the water molecule to heptazine along the pre-existing hydrogen bond was constructed as a so-called relaxed scan; that is, for a fixed value of the driving coordinate (the OH distance of H₂O involved in the hydrogen bonding with heptazine) all other internal coordinates of the complex were relaxed in the respective electronic state. When the construction of a relaxed scan was not technically feasible, an approximate reaction path leading from the ground-state equilibrium geometry to the final geometry was constructed as a linear interpolation in Cartesian nuclear coordinates between the initial and final geometries. The energy profiles of this reaction path were obtained as single-point energy calculations along the interpolated path. The reaction path for the photodetachment of the hydrogen atom from the heptazinyl radical was constructed as a rigid scan, since the relaxation of the internal coordinates of heptazine is of less importance in this case. We refer to ref 43 for a more detailed explanation of the methods for the construction of the reaction paths and energy profiles.

The MP2 and ADC(2) calculations were carried out with the TURBOMOLE program package,⁵⁵ making use of the resolution-of-the-identity (RI) approximation⁵⁶ for the evaluation of the electron-repulsion integrals. Solvent effects on the electronic excitation energies were taken into account with the conductor-like screening model (COSMO) as described by Lunkenheimer and Köhn⁵⁷ and implemented in the Turbomole package.⁵⁵ To simulate a macroscopic water environment, the dielectric constant was set to $\epsilon = 80$ and the refractive index to 1.33. Vertical excitation energies were calculated with a continuum solvation shell which was relaxed for the electronic ground state.

3. RESULTS

3.1. Photoinduced Water Oxidation in the Heptazine–Water Complex. The structure of the heptazine–H₂O hydrogen-bonded complex in the electronic ground state is shown in Figure 1. This minimum-energy structure has been optimized with the MP2 method. The heptazine molecule is planar, and the hydrogen-bonded water molecule is found to be coplanar with the heptazine molecule. The complex thus has C_s symmetry. The water molecule attaches as H atom donor to one of the peripheral N atoms of heptazine. The bond length of

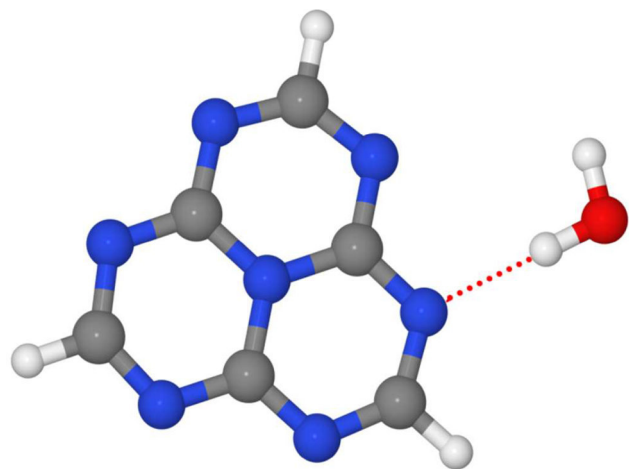


Figure 1. Ground-state equilibrium geometry of the heptazine–H₂O complex. The hydrogen bond is indicated by the dotted line.

the hydrogen bond (dotted line in Figure 1) is 2.046 Å, indicating a moderately strong hydrogen bond. Recent DFT calculations predicted that the planar C₆N₈ primitive unit cell of g-C₃N₄ becomes out-of-plane distorted (“buckled”) upon hydrogen bonding with one or several water molecules.^{34,35} We do not confirm this finding with ab initio methods for clusters of water with the heptazine molecule.

The vertical electronic excitation spectrum of the heptazine–H₂O complex below 6.0 eV is essentially identical with that of isolated heptazine, since water does not absorb in this energy range. The vertical excitation energies and oscillator strengths of the heptazine–H₂O complex up to 5.0 eV are given in Table 1. The excitation spectrum consists of a low-lying dark ¹ππ* state

Table 1. Vertical Electronic Excitation Energies (in eV) and Oscillator Strengths (*f*) of the Heptazine–H₂O Complex up to 5.0 eV

state	energy	<i>f</i>
S ₁ A' (ππ*)	2.60	0.000
S ₂ A'' (nπ*)	3.72	0.000
S ₃ A'' (nπ*)	3.80	0.000
S ₄ A'' (nπ*)	3.89	0.000
S ₅ A' (ππ*)	4.20	0.256
S ₆ A' (ππ*)	4.22	0.252
S ₇ A'' (nπ*)	4.75	0.002
S ₈ A'' (nπ*)	4.80	0.001

state at 2.6 eV (S₁), three nearly degenerate dark ¹nπ* states at 3.8 eV (S₂–S₄), and two quasi-degenerate bright ¹ππ* states (S₅, S₆) at 4.2 eV (300 nm). Two of the three ¹nπ* states and the two ¹ππ* states are exactly degenerate in isolated heptazine due to D_{3h} symmetry. The two ¹ππ* states at 4.2 eV are strongly absorbing states with a remarkably large cumulative oscillator strength of 0.5. The next higher states are two dark ¹nπ* states near 4.8 eV (S₇, S₈). It is noteworthy that the four lowest singlet states are dark in absorption from the ground state. The first bright state is 1.6 eV above the lowest excited singlet state. It seems that this generic feature of the absorption spectrum of the heptazine molecule is not taken into account in the interpretation of periodic DFT calculations, in which the energy gap between the ground state and the lowest excited state is associated with the optical gap.^{22–24,26,31}

The Hartree–Fock molecular orbitals involved in the excitation of the lowest ¹ππ* states of the heptazine–H₂O complex are displayed in Figure 2. The excitation from the highest molecular orbital (HOMO, 8a'') to the lowest unoccupied molecular orbital (LUMO, 9a'') gives rise to the lowest excited singlet state at 2.6 eV. Inspection of Figure 2 reveals that the HOMO is exclusively located on the N atoms, while the LUMO is exclusively located on the C atoms. The HOMO → LUMO excitation thus shifts electron density from the N atoms to the C atoms, rendering the N atoms highly electron deficient. The nearly zero overlap of the HOMO and LUMO orbitals explains the lack of oscillator strength of the lowest ¹ππ* state. The higher π* orbitals (10a'', 11a'') exhibit better overlap with the HOMO, which gives rise to their substantial oscillator strengths.

The effect of the macroscopic polarization response of an aqueous environment on the vertical excitation energies was estimated at the ADC(2) level with the COSMO continuum model. The vertical excitation energies of the heptazine–H₂O complex calculated with ADC(2) and the COSMO continuum

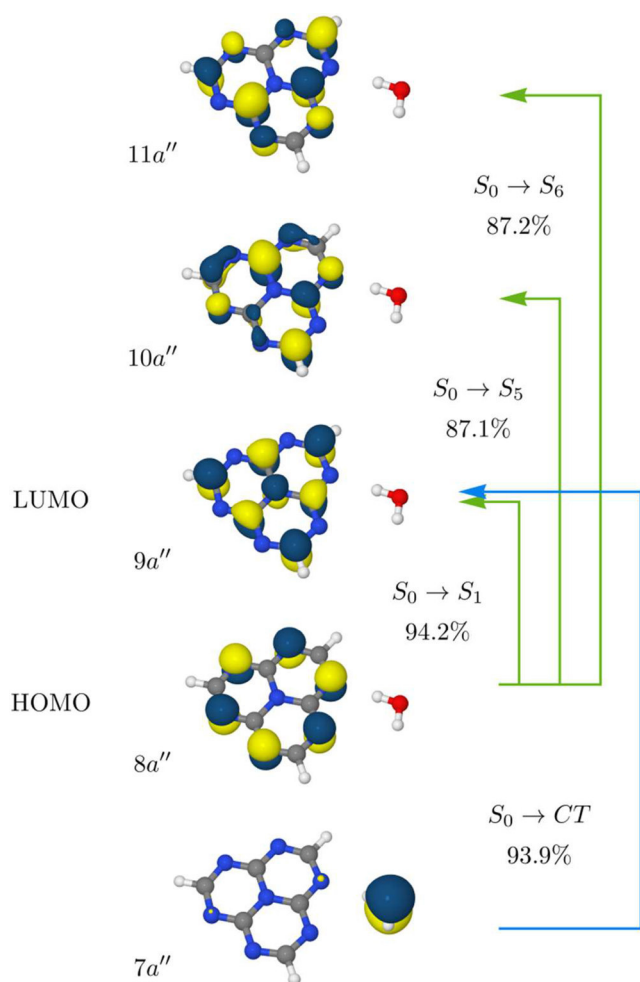


Figure 2. Molecular orbitals involved in the lowest excited states of the heptazine–H₂O complex at the ground-state equilibrium geometry. Green arrows indicate $\pi \rightarrow \pi^*$ excitations; the blue arrow indicates the charge-transfer (CT) excitation from the $7a''$ orbital localized on the oxygen atom of the water molecule to the lowest π^* orbital of heptazine ($9a''$). The numbers give the percentage of the leading configuration state function in the excited-state electronic wave function.

model are given in Table S1 of the [Supporting Information](#). With the exception of the lowest $^1\pi\pi^*$ state, which is blue-shifted by 0.2 eV, the solvation effects are small (less than 0.1 eV) for the vertical excitation energies of the $^1\pi\pi^*$ states. As expected, the excitation energies of the $^1n\pi^*$ states are blue-shifted by the aqueous environment (up to 0.3 eV).

In addition to the locally excited states of the heptazine chromophore, there exist charge-transfer excited states in which an electron is transferred from an occupied molecular orbital localized on water ($7a''$, see [Figure 2](#)) to low-lying π^* orbitals of heptazine. In the $7a'' \rightarrow 9a''$ excited state, the density of one electron has been transferred from the p_z orbital on the oxygen atom of water to the carbon atoms of the heptazine ring (see [Figure 2](#)). This electronic charge transfer occurs essentially instantaneously when, by a fluctuation of the distance of the donor (O) and acceptor (N) atoms of the hydrogen bond, the $7a''$ (HOMO–1) and $8a''$ (HOMO) orbitals become nearly degenerate. After the hole transfer from heptazine to water, the electronic charge separation exerts a strong force on the proton left with the positively charged water molecule. This force

drives the transfer of the proton from H₂O to heptazine along the intermolecular hydrogen bond. To reveal this effect, which is generic for hydrogen-bonded clusters of N-heterocycles with water,^{40,43,58} we constructed the minimum-energy reaction path for H atom transfer from water to heptazine as a relaxed scan. The driving coordinate for the reaction path is the OH bond stretching coordinate R_{OH} of the OH group of H₂O involved in the hydrogen bonding with heptazine (for $R_{\text{OH}} \approx 1.0$ Å, the H atom is covalently bonded to the oxygen atom of water, while for $R_{\text{OH}} \approx 2.0$ Å the H atom is covalently bonded to the nitrogen atom of heptazine). We have constructed this relaxed scan for the electronic ground state of the complex as well as for the lowest excited electronic state (relaxed scans cannot be computed for higher excited states, since the energies of higher excited states usually collapse to the energy of the lowest excited state upon geometry optimization). The energy profiles of the electronic ground state and the relevant excited electronic states along these reaction paths are shown in [Figure 3](#). For clarity, we present the energy profiles for the

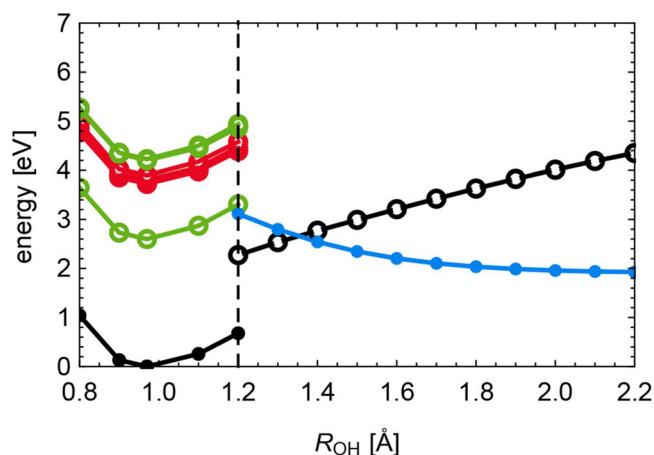


Figure 3. Energy profiles of the electronic ground state and the lowest excited states of the heptazine–H₂O complex along minimum-energy paths for H atom transfer from water to heptazine, calculated with the ADC(2) method. Full circles indicate that the reaction path has been optimized in this state. Open circles represent the energies of electronic states which have been calculated for geometries optimized in a different electronic state. The dashed vertical line separates the reaction path optimized in the S_0 state (left) from the reaction path optimized in the lowest charge-transfer state (right). Black: S_0 state; green: locally excited $^1\pi\pi^*$ states, red: locally excited $^1n\pi^*$ states; blue: charge-transfer state.

reaction path optimized in the electronic ground state for $R_{\text{OH}} < 1.2$ Å and the energy profiles for the reaction path optimized in the $^1\pi\pi^*$ state of charge-transfer character for $R_{\text{OH}} > 1.2$ Å. The vertical dashed line in [Figure 3](#) separates the two different reaction paths. For $R_{\text{OH}} < 1.2$ Å, the energy of the electronic ground state was optimized (full black circles), and the energies of the excited states were calculated at these geometries (open colored circles). For $R_{\text{OH}} > 1.2$ Å, the energy of the lowest charge-transfer state was optimized (full blue circles), and the energy of the closed-shell ground state was computed at these geometries (open black circles).

The left part of [Figure 3](#) ($R_{\text{OH}} < 1.2$ Å) reveals that there is no driving force for proton transfer in the locally excited states of heptazine in the heptazine–H₂O complex, since all excited-state energy profiles are parallel to the PE function of the electronic ground state. The right part of [Figure 3](#), on the other

hand, reveals that the lowest charge-transfer state is stabilized by several electronvolts when the geometry is optimized in this electronic state. For large R_{OH} ($R_{\text{OH}} \approx 2.0 \text{ \AA}$), the mobile proton is attached to the N atom of heptazine and is hydrogen bonded to the OH radical; that is, a proton transfer from H_2O to heptazine has occurred. The closed-shell ground state, on the other hand, is strongly destabilized by the transfer of the proton from water to heptazine. As a result, the energy of the lowest charge-transfer state drops below the energy of the S_0 state at $R_{\text{OH}} = 1.35 \text{ \AA}$ (see Figure 3). Since both electron and proton have moved from water to heptazine, the lowest electronic state for $R_{\text{OH}} \approx 2.0 \text{ \AA}$ is a neutral heptazinyl–OH biradical. It should be noted that the crossing of the blue and black lines on the right-hand side of Figure 3 is a true crossing (that is an intersection of electronic energies), since both energy profiles were calculated at the same geometries. Since the two electronic states have the same spatial and spin symmetry ($^1A'$), the curve crossing in Figure 3 indicates the existence of a conical intersection. The dynamics at this conical intersection governs the branching ratio between biradical formation (reaction) and relaxation to the electronic ground state (aborted reaction). In the case of reaction, the weakly hydrogen-bonded heptazinyl and OH radicals will dissociate owing to the large excess energy becoming available through the electron/proton transfer reaction, resulting in separated free heptazinyl and OH radicals. About 47% (2.0 eV) of the energy of the absorbed photon (4.2 eV) is thus stored as chemical energy in the two radicals. A similar photoinduced electron/proton transfer process leading to a free OH radical was recently revealed by first-principles nonadiabatic dynamics simulations at the TDDFT level for hydrogen-bonded clusters of $(\text{TiO}_2)_4(\text{OH})_4$ nanoparticles with water molecules.⁵⁹

It should be kept in mind that the energy profiles for $R_{\text{OH}} < 1.2 \text{ \AA}$ and $R_{\text{OH}} > 1.2 \text{ \AA}$ in Figure 3 correspond to minimum-energy reaction paths in different valleys of the multidimensional PE surface of the heptazine– H_2O complex. To determine the barrier which connects these two valleys of the PE surface, we constructed a two-dimensional relaxed scan at the ADC(2) level. The two most relevant nuclear coordinates for the description of the photoinduced H atom transfer dynamics in the heptazine– H_2O complex are the H atom transfer coordinate R_{OH} and the distance R_{ON} of the H atom donor (O) and H atom acceptor (N) atoms. For fixed R_{OH} and R_{ON} , the energy of the lowest excited electronic singlet state was optimized with respect to all other internal coordinates of the complex, except the three CH bond lengths of heptazine. The CH bond lengths were constrained to their ground-state equilibrium value to prevent H atom abstraction from heptazine by the nascent OH radical. In $g\text{-C}_3\text{N}_4$, the heptazine units are linked by nitrogen atoms. The CH-abstraction reaction therefore is not relevant for the aqueous photochemistry of $g\text{-C}_3\text{N}_4$.

The resulting relaxed two-dimensional PE surface in the vicinity of the reaction barrier is shown in Figure 4. The well on the left-hand side ($R_{\text{OH}} \approx 1.0 \text{ \AA}$, $R_{\text{ON}} \approx 2.9 \text{ \AA}$) represents the local minimum of the lowest $^1\pi\pi^*$ excited state of heptazine (it corresponds to the lowest green PE function on the left-hand side of Figure 3). The pronounced valley on the right-hand side of Figure 4 ($R_{\text{OH}} \approx 1.9 \text{ \AA}$, $R_{\text{ON}} \approx 2.9 \text{ \AA}$) represents the reaction channel to the $\text{C}_6\text{N}_7\text{H}_4\text{-OH}$ biradical (it corresponds to the blue PE function on the right-hand side of Figure 3). The two valleys are separated by a barrier which is estimated as 0.75 eV with respect to the energy minimum of the lowest $^1\pi\pi^*$ excited

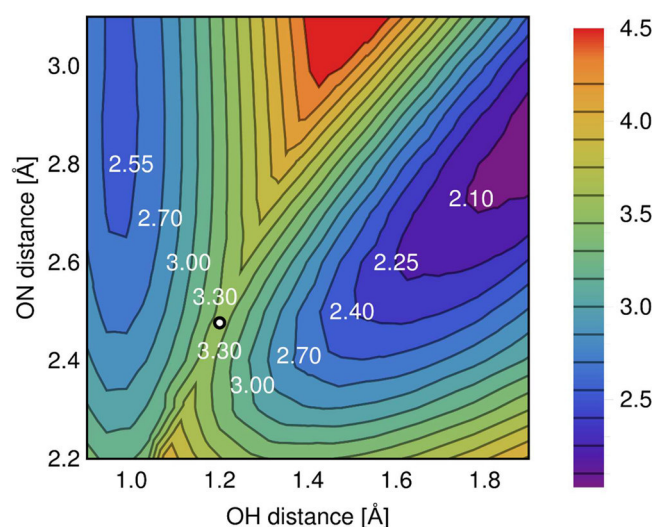


Figure 4. PE surface of the lowest excited singlet state in the vicinity of the barrier for H atom transfer from water to heptazine in the heptazine– H_2O complex, calculated with the ADC(2) method. The nuclear coordinates are the OH bond length of water and the distance of the oxygen atom of water from the peripheral nitrogen atom of heptazine. The PE surface is relaxed with respect to all other internal coordinates of the complex (except the CH bond lengths of heptazine). The numbers give the potential energy relative to the ground-state minimum in electronvolts. The circle indicates the location of the saddle point.

state (S_1). While this barrier is substantial, one has to keep in mind that not the dark S_1 state but the bright S_5 , S_6 states are prepared by photoexcitation of heptazine. The S_5 , S_6 states are 1.6 eV higher in energy than the S_1 state. When the S_1 PE surface is populated by ultrafast radiationless relaxation from the S_5 and S_6 states (as expected according to Kasha's rule), a vibrational excess energy of 1.6 eV becomes available on a femtosecond time scale. The vibrational energy of the system thus is substantially above the barrier for the H atom transfer reaction (0.75 eV). The reaction yield is determined by the competition between intrastate vibrational relaxation (IVR) on the locally excited S_1 surface, which drains energy out of the reactive coordinates, and the H atom transfer reaction, which requires a shrinking of the ON distance and stretching of the OH distance, possibly involving tunneling through the barrier. It should be stressed that the reaction is governed by nonequilibrium dissipative quantum dynamics rather than by conventional equilibrium barrier-crossing dynamics. The reaction is electronically nonadiabatic, since the character of the electronic wave function changes from locally excited $^1\pi\pi^*$ ($8a' \rightarrow 10a'', 11a''$) character to charge-transfer ($7a'' \rightarrow 9a''$) character across the barrier.

Alternatively to the S_5 , $S_6 \rightarrow S_1$ radiationless decay path, a barrierless or low-barrier reaction path may exist which connects the PE surfaces of the bright S_5 , S_6 states directly with the PE surface of the reactive charge-transfer state. To see whether this possibility exists, we constructed an approximate (nonoptimized) reaction path from the ground-state equilibrium geometry to the relaxed geometry of the lowest charge-transfer state at fixed $R_{\text{OH}} = 1.2 \text{ \AA}$ by linear interpolation in Cartesian coordinates. The corresponding energy profiles of the ground state and the lowest excited states are shown in Figure 5. Along this approximate reaction path, the energy profiles of the nearly degenerate bright S_5 , S_6 states as well as the energy

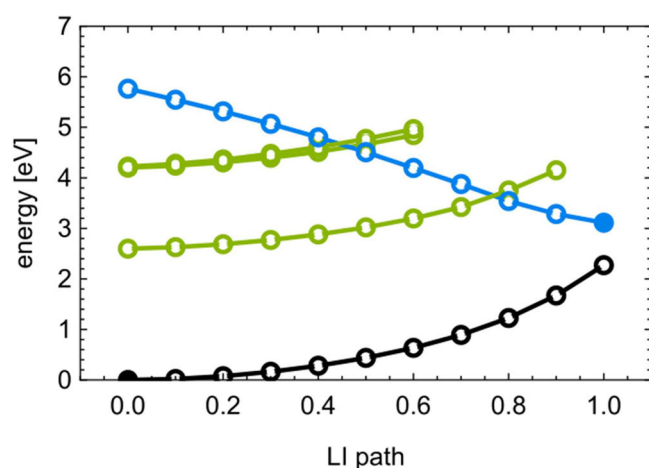


Figure 5. Energy profiles of the heptazine–water complex for the linearly interpolated (LI) path between the ground-state equilibrium geometry (left, full black circle) and the optimized geometry of the charge-transfer state at $R_{\text{OH}} = 1.2 \text{ \AA}$ (right, full blue circle). The charge-transfer state (blue) is stabilized along the reaction path and crosses the energies of the two nearly degenerate bright ${}^1\pi\pi^*$ states as well as the energy of the lowest ${}^1\pi\pi^*$ state of heptazine (green). An upper bound of 0.4 eV is estimated for the barrier resulting from the crossing of the charge-transfer state with the two bright ${}^1\pi\pi^*$ states.

profile of the S_1 state (green) are crossed by the profile of the reactive charge-transfer state (blue). These energy crossings are conical intersections, since all electronic states are of ${}^1A'$ symmetry. The crossing of the S_5 , S_6 states with the charge-transfer state is approximately 0.4 eV above the vertical excitation energy of the former (see Figure 5). The energy of this crossing is an upper limit to the actual height of the reaction barrier. The true barrier, if any, is estimated to be of a few tenths of an electronvolt at most. Such barriers can be overcome (or possibly tunneled) by the system within tens or hundreds of picoseconds, depending on the temperature and the vibrational excess energy available after vertical excitation of the bright ${}^1\pi\pi^*$ states. There exists thus a second nonadiabatic reaction mechanism by which the reactive charge-transfer state can be populated from the bright S_5 , S_6 states of heptazine.

While the reaction mechanism illustrated by the PE profiles of Figures 3 and 4 is qualitatively the same as described earlier for the pyridine–water complex⁴³ or the acridine–water complex,⁵⁸ there are important quantitative differences. Apart from the lower excitation energies of the bright ${}^1\pi\pi^*$ states and the much larger associated oscillator strengths in heptazine, the energy of the charge-transfer state is considerably lower in the heptazine– H_2O complex than in the pyridine– H_2O and acridine– H_2O complexes. Therefore, the crossing of the energies of the charge-transfer and S_0 states occurs “earlier” in the heptazine– H_2O complex (at $R_{\text{OH}} = 1.35 \text{ \AA}$) than in the pyridine–water complex (at $R_{\text{OH}} = 1.70 \text{ \AA}$) and the acridine–water complex (at $R_{\text{OH}} = 1.50 \text{ \AA}$). For heptazine– H_2O , the energy crossing is located in the repulsive part of the energy profile of the charge-transfer state, while it occurs in the flat asymptotic region in pyridine– H_2O . As a consequence, the recombination of heptazinyl and OH radicals is hindered by a sizable barrier (see Figures 3 and 4). This feature indicates that the geminate recombination of heptazinyl and OH radicals is strongly suppressed. These radicals should therefore be potentially long-lived metastable species.

3.2. Photodissociation of the Heptazinyl Radical. The vertical excitation energies and oscillator strengths of the heptazinyl radical ($\text{C}_6\text{N}_7\text{H}_4$) up to 5 eV are listed in Table 2.

Table 2. Vertical Electronic Excitation Energies (in eV) and Oscillator Strengths (f) of the Heptazinyl Radical

state	energy	f
$D_1 A'' (\pi\pi^*)$	1.59	0.003
$D_2 A'' (\pi\pi^*)$	1.83	0.009
$D_3 A' (\pi\sigma^*)$	3.21	0.000
$D_4 A'' (\pi\pi^*)$	3.40	0.011
$D_5 A'' (\pi\pi^*)$	3.64	0.038
$D_6 A' (n\pi^*)$	3.87	0.000
$D_7 A'' (\pi\pi^*)$	3.89	0.003
$D_8 A' (\pi\sigma^*)$	3.91	0.000
$D_9 A' (n\pi^*)$	4.05	0.001
$D_{10} A'' (\pi\pi^*)$	4.14	0.006
$D_{11} A' (\pi\sigma^*)$	4.41	0.002
$D_{12} A'' (\pi\pi^*)$	4.47	0.071
$D_{13} A'' (\pi\pi^*)$	4.49	0.152
$D_{14} A' (n\pi^*)$	4.49	0.000
$D_{15} A' (n\pi^*)$	4.57	0.000
$D_{16} A' (n\pi^*)$	4.77	0.001
$D_{17} A' (\pi\sigma^*)$	4.82	0.000
$D_{18} A'' (\pi\pi^*)$	4.86	0.292

The excitation spectrum exhibits two low-lying (1.6, 1.8 eV) essentially dark ${}^2\pi\pi^*$ states (D_1 , D_2), a dark state of ${}^2\pi\sigma^*$ character at 3.2 eV (D_3), and two weakly absorbing ($f = 0.05$) ${}^2\pi\pi^*$ states (D_4 , D_5) near 3.5 eV (355 nm), followed by a dense manifold of dark or nearly dark ${}^2n\pi^*$, ${}^2\pi\pi^*$, and ${}^2\pi\sigma^*$ states. The lowest strongly absorbing states are the states S_{13} and S_{18} at 4.49 and 4.86 eV, respectively. Unexpectedly, these strongly absorbing states are at higher energy in the heptazinyl radical than the strongly absorbing states in the closed-shell heptazine molecule. The vertical excitation energies of heptazinyl calculated with the COSMO continuum model are given in Table S2 of the Supporting Information. The ${}^2\pi\pi^*$ states are shifted by less than 0.1 eV by the inclusion of a polarizable environment. The ${}^2n\pi^*$ states and the ${}^2\pi\sigma^*$ states, on the other hand, are upshifted in energy by about 0.3 eV in the polarizable environment.

The ${}^2\pi\sigma^*$ (D_3) state plays a particular role in the chemistry and photochemistry of the heptazinyl radical. The singly occupied π orbital ($8a''$) and the σ^* orbital ($38a'$) at the ground-state equilibrium geometry of the heptazinyl radical are displayed in Figure 6. It can be seen that the σ^* orbital is a Rydberg orbital which is considerably more diffuse than the π orbital. In addition, the σ^* orbital is antibonding with respect to the NH bond and is mostly localized outside the heteroaromatic ring. In the electronic ground state of the radical, the unpaired electron occupies the π ($8a''$) orbital. In the ${}^2\pi\sigma^*$ excited state, the unpaired electron occupies the σ^* ($38a'$) orbital, while the π ($8a''$) orbital is empty. The $8a'' \rightarrow 38a'$ excitation therefore transfers electron density from the heteroaromatic ring beyond the H atom of the NH group. This electronic charge translocation provides the driving force for the dissociation of the NH bond. Upon stretching of the NH bond, the σ^* orbital contracts to the compact hydrogen 1s orbital. This contraction leads to an additional stabilization of the energy of the ${}^2\pi\sigma^*$ state at large NH distances. Because of these mechanisms, the ${}^2\pi\sigma^*$ state exhibits an exceptionally low

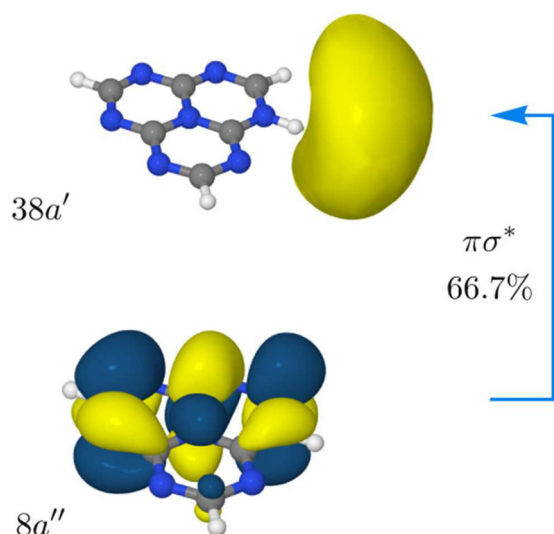


Figure 6. Singly occupied π orbital ($8a''$) and the σ^* orbital ($38a'$) involved in the excitation of the ${}^2\pi\sigma^*$ state of the heptazinyl radical. 66.7% is the percentage of the leading configuration state function in the excited-state electronic wave function.

dissociation energy, although there exists a strong covalent NH bond in the electronic ground state of the radical.

The PE profiles of the lowest seven electronic states (D_0 – D_6) for the dissociation of the NH bond of the heptazinyl radical are shown in Figure 7. For clarity, the densely spaced

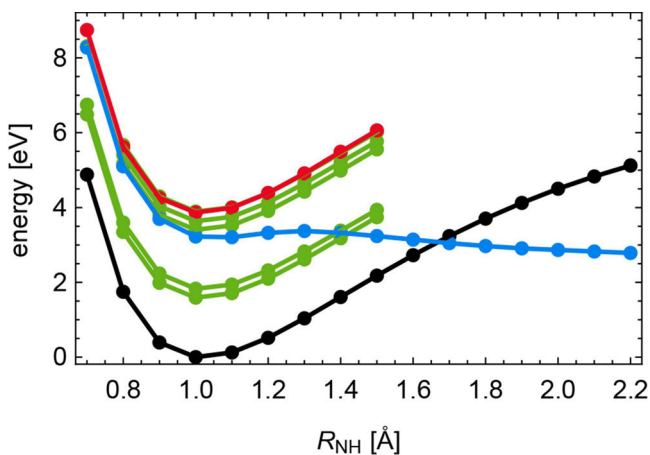


Figure 7. Energy profiles of the electronic ground state (black) and the lowest excited electronic states along the NH stretching coordinate of the heptazinyl radical, calculated with the ADC(2) method. Green: ${}^2\pi\pi^*$ excited states; red: ${}^2n\pi^*$ state; blue: ${}^2\pi\sigma^*$ state.

higher lying states are not included. These PE functions are rigid scans; that is, all internal nuclear coordinates except the NH distance are kept fixed at the ground-state equilibrium geometry. Previous calculations for closed-shell systems or radicals with azine groups have shown that the effect of the relaxation of the remaining nuclear degrees of freedom is minor for the NH bond dissociation.^{43,58,60–64} While the PE functions of all ${}^2\pi\pi^*$ (green) and ${}^2n\pi^*$ (red) excited states are essentially parallel to the bound PE function of the electronic ground state, the PE function of the lowest state of ${}^2\pi\sigma^*$ character (blue) is apart from a low barrier, dissociative with respect to the NH stretching coordinate of the heptazinyl radical. The low barrier at $R_{\text{NH}} \approx 1.3$ Å reflects the transformation of the singly

occupied σ^* orbital from a diffuse Rydberg orbital localized on the NH group of heptazine to a compact valence orbital localized on the departing H atom. This $\pi\sigma^*$ -mediated bond-dissociation phenomenon is experimentally and theoretically well established for closed-shell aromatic systems with acidic groups, such as pyrrole, indole, phenol, or aniline.^{60–63} While the dissociation energy of the ground state of heptazinyl is larger than 5 eV, the dissociation threshold of the ${}^2\pi\sigma^*$ state is merely 2.0 eV (calculated at the CCSD level), which is less than half of the dissociation energy of the D_0 state (see Figure 6). After dissociation, 2.0 eV (about 45% of the original photon energy of 4.5 eV) is stored as chemical energy in the H radical.

The ${}^2\pi\sigma^*$ state of heptazinyl is optically dark and therefore cannot be populated directly by photoabsorption from the electronic ground state. It can be populated, however, by a fast radiationless transition from the bright D_{13} , D_{18} states to the ${}^2\pi\sigma^*$ state. Figure 7 shows that dissociation in the ${}^2\pi\sigma^*$ state involves crossings of the ${}^2\pi\sigma^*$ energy (blue) with the energies of the lowest two ${}^2\pi\pi^*$ states (green) as well as with the D_0 state (black). These three energy crossings are symmetry allowed crossings in the planar system, since the ground state and the ${}^2\pi\pi^*$ states are of A' symmetry, while the ${}^2\pi\sigma^*$ state is of A'' symmetry. The symmetry allowed crossings are converted into conical intersections by displacements in out-of-plane vibrational modes. For a more detailed discussion of the nonadiabatic photodissociation dynamics via repulsive ${}^2\pi\sigma^*$ states, we refer to a recent study of the photodissociation dynamics of the pyridinyl radical.⁶⁴ It has been shown therein that efficient photodissociation reactions through several conical intersections are possible.

4. DISCUSSION

The results presented in section 3.1 provide a qualitative mechanistic picture of the photoreaction of the heptazine chromophore with a hydrogen-bonded water molecule. After photoabsorption of a UV/vis photon by the bright S_5 , S_6 states of heptazine in the heptazine–water complex, the lowest excited state (S_1) is populated by a fast radiationless transition. The vibrational excess energy becoming available by the radiationless transition (1.6 eV) is significantly higher than the height of the barrier (0.75 eV) which separates the local minimum of the S_1 surface from the reaction valley leading to the generation of the heptazinyl and OH radicals (Figure 4). In addition, there exists a low-barrier (or possibly barrierless) reaction channel which leads directly from the photoabsorbing S_5 , S_6 states to the reactive charge-transfer state (Figure 5). At the crossing of the PE surface of the charge-transfer state with the PE surface of the S_0 state, the reaction bifurcates. If the system remains in the charge-transfer state, a neutral heptazinyl–OH radical pair is generated with substantial excess energy. If, on the other hand, the system switches from the charge-transfer state to the S_0 state at the surface crossing, the H atom transfer reaction is aborted and the system relaxes by IVR and vibrational energy transfer to the environment to the minimum of the PE surface of the original electronic ground state. In the former case, part of the energy of the absorbed photon is stored as chemical energy in two radicals. In the latter case, the energy of the absorbed photon is dissipated into vibrational energy in the S_0 state and the environment and thus is lost.

The results presented in section 3.2 indicate that the excess hydrogen atom of the heptazinyl radical can be photodetached by a second UV/vis photon due to the existence of a low-lying

${}^2\pi\sigma^*$ state with a PE function which is repulsive with respect to NH dissociation. Although the ${}^2\pi\sigma^*$ state of heptazinyl cannot be excited directly by light, it can be populated via the excitation of two bright ${}^2\pi\pi^*$ states with excitation energies near 4.5 and 4.9 eV. Predissociation of the latter states by the repulsive ${}^2\pi\sigma^*$ state opens a channel for direct (nonstatistical) H atom photodetachment through conical intersections of the ${}^2\pi\sigma^*$ state with the lowest ${}^2\pi\pi^*$ states and the D_0 state (see Figure 7). Via this photodissociation reaction, the heptazinyl molecule is regenerated (and thus becomes a photocatalyst). In this scenario (henceforth referred to as scenario I), a water molecule is split into H and OH radicals by the sequential absorption of two photons by a single heptazine chromophore. Qualitatively, about 46% of the energy of the two photons is converted into the chemical energy of two radicals. With two heptazine molecules and four photons, two water molecules can be decomposed into four H atoms and two OH radicals. The former can recombine in a dark reaction with a conventional catalyst (dispersed Pt or Pd) to H_2 . The OH radicals either can be scavenged by a sacrificial reagent (e.g., methanol or triethanolamine) or can be recombined in a dark reaction to H_2O_2 with a suitable catalyst (e.g., manganese oxide, MnO). H_2O_2 can be catalytically decomposed into $H_2O + 1/2O_2$. Both light-driven reactions in this scenario are energetically downhill as well as barrierless and therefore ultrafast. The ensuing dark radical recombination reactions, on the other hand, are conventional overbarrier reactions which require catalysts.

Owing to the exceptionally low dissociation energy of the heptazinyl radical (2.0 eV, see Figure 7), there exists an alternative scenario, henceforth referred to as scenario II. Two heptazinyl radicals, which are generated by photoinduced H atom abstraction in two heptazine–water complexes, can recombine to form H_2 , thereby regenerating two heptazine molecules. This dark radical recombination reaction is exothermic, since the binding energy of H_2 (4.6 eV) is more than twice the binding energy of heptazinyl (2.0 eV). A conventional catalyst (dispersed Pt or Pd) is needed for the recombination reaction which recovers the heptazine chromophore. In this scenario, two water molecules are decomposed into H_2 and two OH radicals by the absorption of two photons. Other than in scenario I, the two photons are absorbed by two different heptazine chromophores. The photodissociation reaction of heptazinyl radicals is not needed in scenario II: the sequence of a light-driven reaction in two chromophore–water complexes and one dark recombination reaction regenerates the photocatalyst.

It may be worthwhile to emphasize that the two water-splitting scenarios suggested by the present work (and previous results for pyridine–water^{43,44,65} and acridine–water complexes^{58,66}) are mechanistically quite different from the established paradigms of photocatalytic water splitting with semiconductors or g- C_3N_4 polymers mentioned in the Introduction (exciton generation, exciton dissociation, diffusion of charge carriers to solid/liquid interfaces, reaction with water at the interfaces). While the excitation of the bright ${}^1\pi\pi^*$ state(s) can be considered as exciton generation and the electron transfer from the hydrogen-bonded water molecule to the heptazine chromophore as exciton dissociation, the proton involved in the hydrogen bond between the chromophore and the water molecule neutralizes the electronic charge separation on a time scale of tens of femtoseconds (the intrinsic time scale of barrierless proton transfer^{67,68}), resulting in the formation of neutral radicals on this time scale. In the prevailing paradigm,

on the contrary, electrons and holes are separated on time scales of nanoseconds or microseconds and over distances of micrometers. Clearly, the separation of neutral radicals is less challenging than the separation of electrons and holes against their Coulomb attraction, even in polarizable environments. In scenario I discussed above, both the H atom transfer reaction and the H atom dissociation reaction are light-driven, energetically downhill and ultrafast and, as such, do not require a conventional catalyst. Catalysts are needed for the ensuing dark radical recombination reactions, such as Pt or Pd for the recombination of H atoms to H_2 molecules and MnO or similar heterogeneous catalysts for the recombination of OH radicals. In scenario II, only the first step (the oxidation of water in heptazine–water complexes) is light-driven and ultrafast, whereas the dark recombination of two heptazinyl radicals to form H_2 and to regenerate heptazine is a conventional overbarrier reaction which requires a catalyst.

The photochemical picture of photoinduced water splitting with g- C_3N_4 materials predicts that the *in situ* detection of photogenerated free radicals should be possible. In scenario I, free OH radicals as well as free H radicals are generated. It should be possible to detect the OH radicals *in situ* by chemical scavenging and spectroscopic (laser-induced fluorescence) detection of the hydroxylated products, as demonstrated recently for OH radicals generated with TiO_2 materials (anatase, rutile)^{69–71} or titanyl porphyrin/phthalocyanine molecular photocatalysts.^{72,73} In scenario II, no free H radicals are generated. The *in situ* detection of H radicals could thus differentiate between the two scenarios.

It has recently been reported that unexpectedly long-lived reducing species (lifetimes of many hours in the dark) are generated by the irradiation of cyanamide-functionalized heptazine-based polymers in the presence of a sacrificial electron donor (methanol).⁷⁴ The detection of these yet unidentified species (presumably radicals, since separated charges could not have lifetimes of hours) provides strong support of a homolytic water-splitting mechanism. It has furthermore been shown that H_2 can be evolved from the long-lived (blue-colored) material by the addition of colloidal Pt in the dark, which regenerates the original (yellow) material.⁷⁴ These findings provide strong evidence for scenario II, since the heptazinyl radical absorbs weakly in the red (in contrast to heptazine, which does not absorb below 4.2 eV; see Tables 1 and 2) and thus exhibits blue color. The observed delayed generation of H_2 in the dark with dispersed Pt is in agreement with the prediction that H_2 can be generated by Pt-catalyzed recombination of heptazinyl radicals. The role of the sacrificial reagent in these experiments is to scavenge the OH radicals, which suppresses the recombination of OH radicals with heptazinyl radicals.

5. CONCLUSIONS

The photochemistry of the heptazine chromophore in a hydrogen-bonded heptazine– H_2O complex was explored with *ab initio* computational methods. The key feature of heptazine, apart from its high oscillator strength in the near-UV, are its electron-deficient peripheral nitrogen atoms embedded in the aromatic frame, which may be referred to as “pyridinic” nitrogen atoms. These N atoms readily form hydrogen bonds with surrounding water molecules. The decisive photochemical reaction is enabled by an exceptionally low-lying water-to-heptazine charge-transfer state in the hydrogen-bonded heptazine–water complex which has been identified in the

present work. This state drives the transfer of a proton from water to the N atom of heptazine along the hydrogen bond. By the light-induced transfer of an electron and a proton, a heptazinyl radical and an OH radical in their electronic ground states are formed.

Another key feature relevant for the water-splitting reaction with the heptazine chromophore is the existence of a low-lying dissociative ${}^2\pi\sigma^*$ state in the heptazinyl radical. The predissociation of the light-absorbing ${}^2\pi\pi^*$ states of the heptazinyl radical by this ${}^2\pi\sigma^*$ state opens a channel for direct and fast (nonstatistical) photodissociation of the radical. The catalytic cycle can thus be closed by the photodissociation of the heptazinyl radical with a second photon (scenario I). Owing to the exceptionally low H atom dissociation energy of the heptazinyl radical (≈ 2.0 eV), the recombination of two heptazinyl radicals to yield H_2 and two heptazine molecules is an exothermic reaction. The catalytic cycle can thus alternatively be closed by a dark radical recombination reaction with a suitable catalyst (scenario II).

Previous computational studies of photocatalytic water splitting with C_3N_4 materials addressed the thermodynamic stability^{20,21} and the electronic band structure of the crystalline or polymeric materials.^{22–25} Structural aspects of hydrogen bonding of water with heptazine oligomers also were explored.^{33,34} Wirth et al. explored H atom transfer reactions between heptazine units and hydrogen-bonded water molecules in the electronic ground state, demonstrating that these reactions are highly endothermic.³⁵ In the present work, the first computational investigations of the excited-state electronic structure and excited-state reaction paths of the heptazine–water complex and the heptazinyl radical were performed. Since such wave function-based excited-state electronic-structure calculations including geometry optimization are highly demanding, we had to restrict ourselves to the smallest model system exhibiting the relevant mechanisms. Future extensions of the present work should consider the effects of oligomerization of heptazine units and the effects of additional hydrogen-bonded water molecules. It would be highly desirable to reveal the dynamics of the light-driven reactions with nonadiabatic trajectory surface-hopping calculations^{59,75} for isolated heptazine–water clusters. Moreover, the effects of fluctuations of an ambient liquid environment should be simulated with QM/MM methods.⁷⁶

■ ASSOCIATED CONTENT

■ Supporting Information

The Supporting Information is available free of charge on the ACS Publications website at DOI: 10.1021/acs.jpca.7b04594.

Tables of the vertical excitation energies of heptazine and the heptazine– H_2O complex in an aqueous environment, calculated with the ADC(2) method and the COSMO continuum model (PDF)

■ AUTHOR INFORMATION

■ Corresponding Authors

*E-mail: domcke@ch.tum.de (W.D.).

*E-mail: johannes.ehrmaier@tum.de (J.E.).

■ ORCID

Wolfgang Domcke: 0000-0001-6523-1246

■ Notes

The authors declare no competing financial interest.

■ ACKNOWLEDGMENTS

This work has been supported by the Munich Centre for Advanced Photonics. J.E. acknowledges support by the International Max Planck Research School of Advanced Photon Science (IMPRS-APS). A.L.S. acknowledges support by the Alexander von Humboldt Research Award.

■ REFERENCES

- (1) Wang, Y.; Wang, X.; Antonietti, M. Polymeric Graphitic Carbon Nitride as a Heterogeneous Organocatalyst: From Photochemistry to Multipurpose Catalysis to Sustainable Chemistry. *Angew. Chem., Int. Ed.* **2012**, *51*, 68–89.
- (2) Wang, X.; Maeda, K.; Thomas, A.; Takanebe, K.; Xin, G.; Carlsson, J. M.; Domen, K.; Antonietti, M. A Metal-Free Polymeric Photocatalyst for Hydrogen Production from Water under Visible Light. *Nat. Mater.* **2009**, *8*, 76–80.
- (3) Wang, X.; Blechert, S.; Antonietti, M. Polymeric Graphitic Carbon Nitride for Heterogeneous Photocatalysis. *ACS Catal.* **2012**, *2*, 1596–1606.
- (4) Lin, Z.; Wang, X. Nanostructure Engineering and Doping of Conjugated Carbon Nitride Semiconductors for Hydrogen Photosynthesis. *Angew. Chem., Int. Ed.* **2013**, *52*, 1735–1738.
- (5) Chu, S.; Wang, Y.; Guo, Y.; Feng, J.; Wang, C.; Luo, W.; Fan, X.; Zou, Z. Band Structure Engineering of Carbon Nitride: In Search of a Polymer Photocatalyst with High Photooxidation Property. *ACS Catal.* **2013**, *3*, 912–919.
- (6) Martin, D. J.; Qiu, K.; Shevlin, S. A.; Handoko, A. D.; Chen, X.; Guo, Z.; Tang, J. Highly Efficient Photocatalytic H_2 Evolution from Water using Visible Light and Structure-Controlled Graphitic Carbon Nitride. *Angew. Chem., Int. Ed.* **2014**, *53*, 9240–9245.
- (7) Caputo, C. A.; Gross, M. A.; Lau, V. W.; Cavazza, C.; Lotsch, B. V.; Reiser, E. Photocatalytic Hydrogen Production using Polymeric Carbon Nitride with a Hydrogenase and a Bioinspired Synthetic Ni Catalyst. *Angew. Chem., Int. Ed.* **2014**, *53*, 11538–11542.
- (8) Zheng, Y.; Lin, L.; Wang, B.; Wang, X. Graphitic Carbon Nitride Polymers toward Sustainable Photoredox Catalysis. *Angew. Chem., Int. Ed.* **2015**, *54*, 12868–12884.
- (9) Bi, J.; Fang, W.; Li, L.; Wang, J.; Liang, S.; He, Y.; Liu, M.; Wu, L. Covalent Triazine-based Frameworks as Visible Light Photocatalysts for the Splitting of Water. *Macromol. Rapid Commun.* **2015**, *36*, 1799–1805.
- (10) Cao, S.; Low, J.; Yu, J.; Jaroniec, M. Polymeric Photocatalysts Based on Graphitic Carbon Nitride. *Adv. Mater.* **2015**, *27*, 2150–2176.
- (11) Gong, Y.; Li, M.; Wang, Y. Carbon Nitride in Energy Conversion and Storage: Recent Advances and Future Prospects. *ChemSusChem* **2015**, *8*, 931–946.
- (12) Liu, J.; Liu, Y.; Liu, N.; Han, Y.; Zhang, X.; Huang, H.; Lifshitz, Y.; Lee, S.-T.; Zhong, J.; Kang, Z. Metal-Free Efficient Photocatalysts for Stable Visible Water Splitting via a Two-Electron Pathway. *Science* **2015**, *347*, 970–974.
- (13) Zhang, G.; Lan, Z.-A.; Lin, L.; Lin, S.; Wang, X. Overall Water Splitting by Pt/g- C_3N_4 Photocatalysts Without Using Sacrificial Agents. *Chem. Sci.* **2016**, *7*, 3062–3066.
- (14) Algara-Siller, G.; Severin, N.; Chong, S. Y.; Björkman, T.; Palgrave, R. G.; Laybourn, A.; Antonietti, A.; Khimyak, Y. Z.; Krasheninnikov, A. V.; Rabe, J. P.; Kaiser, U.; Cooper, A. I.; Thomas, A.; Bojdys, M. J. Triazine-Based Graphitic Carbon Nitride: A Two-Dimensional Semiconductor. *Angew. Chem., Int. Ed.* **2014**, *53*, 7450–7455.
- (15) Cowan, A. J.; Durrant, J. R. Long-Lived Charge Separated States in Nanostructured Semiconductor Photoelectrodes for the Production of Solar Fuels. *Chem. Soc. Rev.* **2013**, *42*, 2281–2293.
- (16) Swierk, J. R.; Mallouk, T. E. Design and Development of Photoanodes for Water-Splitting Dye-Sensitized Photoelectrochemical Cells. *Chem. Soc. Rev.* **2013**, *42*, 2357–2387.
- (17) Osterloh, F. E. Inorganic Nanostructures for Photoelectrochemical and Photocatalytic Water Splitting. *Chem. Soc. Rev.* **2013**, *42*, 2294–2320.

- (18) Hisatomi, T.; Kubota, J.; Domen, K. Recent Advances in Semiconductors for Photocatalytic and Photoelectrochemical Water Splitting. *Chem. Soc. Rev.* **2014**, *43*, 7520–7535.
- (19) Jafari, T.; Moharreri, E.; Amin, A. S.; Miao, R.; Song, W.; Suib, S. L. Photocatalytic Water Splitting – The Untamed Dream: A Review of Recent Advances. *Molecules* **2016**, *21*, 900.
- (20) Melissen, S. T. A. G.; Steinmann, S. N.; Le Bahers, T.; Sautet, P. DFT Perspective on the Thermochemistry of Carbon Nitride Synthesis. *J. Phys. Chem. C* **2016**, *120*, 24542–24550.
- (21) Botari, T.; Huhn, W. P.; Lau, V. W.; Lotsch, B. V.; Blum, V. Thermodynamic Equilibria in Carbon Nitride Photocatalyst Materials and Conditions for the Existence of Graphitic Carbon Nitride $g\text{-C}_3\text{N}_4$. *Chem. Mater.* **2017**, *29*, 4445–4453.
- (22) Deifallah, M.; McMillan, P. F.; Cora, F. Electronic and Structural Properties of Two-Dimensional Carbon Nitride Graphenes. *J. Phys. Chem. C* **2008**, *112*, 5447–5453.
- (23) Wu, F.; Liu, Y.; Yu, G.; Shen, D.; Wang, Y.; Kan, E. Visible-Light-Absorption in Graphitic C_3N_4 Bilayer: Enhanced by Interlayer Coupling. *J. Phys. Chem. Lett.* **2012**, *3*, 3330–3334.
- (24) Gao, G.; Jiao, Y.; Ma, F.; Jiao, Y.; Waclawik, E.; Du, A. Metal-free Graphitic Carbon Nitride as Mechano-Catalyst for Hydrogen Evolution Reaction. *J. Catal.* **2015**, *332*, 149–155.
- (25) Srinivasu, K.; Modak, B.; Ghosh, S. K. Porous Graphitic Carbon Nitride: A Possible Metal-Free Photocatalyst for Water Splitting. *J. Phys. Chem. C* **2014**, *118*, 26479–26484.
- (26) Liang, D.; Jing, T.; Ma, Y.; Hao, J.; Sun, G.; Deng, M. Photocatalytic Properties of $g\text{-C}_6\text{N}_6/g\text{-C}_3\text{N}_4$ Heterostructure: A Theoretical Study. *J. Phys. Chem. C* **2016**, *120*, 24023–24029.
- (27) Butchosa, C.; McDonald, T. O.; Cooper, A. I.; Adams, D. J.; Zwiijnenburg, M. A. Shining Light on *s*-Triazine-Based Polymers. *J. Phys. Chem. C* **2014**, *118*, 4314–4324.
- (28) Butchosa, C.; Guiglion, P.; Zwiijnenburg, M. A. Carbon Nitride Photocatalysts for Water Splitting: A Computational Perspective. *J. Phys. Chem. C* **2014**, *118*, 24833–24845.
- (29) Melissen, S.; Le Bahers, T.; Steinmann, S. N.; Sautet, P. Relationship between Carbon Nitride Structure and Exciton Binding Energies: A DFT Perspective. *J. Phys. Chem. C* **2015**, *119*, 25188–25196.
- (30) Azofra, L. M.; MacFarlane, D. R.; Sun, C. A DFT Study of Planar vs. Corrugated Graphene-Like Carbon Nitride ($g\text{-C}_3\text{N}_4$) and its Role in the Catalytic Performance of CO_2 Conversion. *Phys. Chem. Chem. Phys.* **2016**, *18*, 18507–18514.
- (31) Feng, J.; Liu, G.; Yuan, S.; Ma, Y. Influence of Functional Groups on Water Splitting in Carbon Nanodot and Graphitic Carbon Nitride Composites: A Theoretical Mechanism Study. *Phys. Chem. Chem. Phys.* **2017**, *19*, 4997–5003.
- (32) Srinivasu, K.; Modak, B.; Ghosh, S. K. Improving the Photocatalytic Activity of *s*-Triazine Based Graphitic Carbon Nitride Through Metal Decoration: An Ab Initio Investigation. *Phys. Chem. Chem. Phys.* **2016**, *18*, 26466–26474.
- (33) Aspera, S. M.; David, M.; Kasai, H. First-Principles Study of the Adsorption of Water on Tri-*s*-Triazine-Based Graphitic Carbon Nitride. *Jpn. J. Appl. Phys.* **2010**, *49*, 115703.
- (34) Wu, H.-Z.; Liu, L.-M.; Zhao, S.-J. The Effect of Water on the Structural, Electronic and Photocatalytic Properties of Graphitic Carbon Nitride. *Phys. Chem. Chem. Phys.* **2014**, *16*, 3299–3304.
- (35) Wirth, J.; Neumann, R.; Antonietti, M.; Saalfrank, P. Adsorption and Photocatalytic Splitting of Water on Graphitic Carbon Nitride: A Combined First Principles and Semiempirical Study. *Phys. Chem. Chem. Phys.* **2014**, *16*, 15917–15926.
- (36) Merschjann, C.; Tyborski, T.; Orthmann, S.; Yang, F.; Schwarzburg, K.; Lublow, M.; Lux-Steiner, M.-C.; Schedel-Niedrig, T. Photophysics of Polymeric Carbon Nitride: An Optical Quasimonomer. *Phys. Rev. B: Condens. Matter Mater. Phys.* **2013**, *87*, 205204.
- (37) Kang, Y.; Yang, Y.; Yin, L.-C.; Kang, X.; Liu, G.; Cheng, H.-M. An Amorphous Carbon Nitride Photocatalyst with Greatly Extended Visible-Light-Responsive Range for Photocatalytic Hydrogen Generation. *Adv. Mater.* **2015**, *27*, 4572–4577.
- (38) Lau, V. W.-H.; Mesch, M. B.; Duppel, V.; Blum, V.; Senker, J.; Lotsch, B. V. Low-Molecular Weight Carbon Nitrides for Solar Hydrogen Evolution. *J. Am. Chem. Soc.* **2015**, *137*, 1064–1072.
- (39) Lau, V. W.-H.; Moudrakovski, I.; Botari, T.; Weinberger, S.; Mesch, M. B.; Duppel, V.; Senker, J.; Blum, V.; Lotsch, B. V. Rational Design of Carbon Nitride Photocatalysts by Identification of Cyanamide Defects as Catalytically Relevant Sites. *Nat. Commun.* **2016**, *7*, 12165.
- (40) Sobolewski, A. L.; Domcke, W. Computational Studies of the Photophysics of Hydrogen-Bonded Molecular Systems. *J. Phys. Chem. A* **2007**, *111*, 11725–11735.
- (41) Weinberg, D. R.; Gagliardi, C. J.; Hull, J. F.; Murphy, C. F.; Kent, C. A.; Westlake, B. C.; Paul, A.; Ess, D. H.; McCafferty, D. G.; Meyer, T. J. Proton-Coupled Electron Transfer. *Chem. Rev.* **2012**, *112*, 4016–4093.
- (42) Guiglion, P.; Berardo, E.; Butchosa, C.; Wobbe, M. C. C.; Zwiijnenburg, M. Modelling Materials for Solar Fuel Synthesis by Artificial Photosynthesis; Predicting the Optical, Electronic and Redox Properties of Photocatalysts. *J. Phys.: Condens. Matter* **2016**, *28*, 074001.
- (43) Liu, X.; Sobolewski, A. L.; Borrelli, R.; Domcke, W. Computational Investigation of the Photoinduced Homolytic Dissociation of Water in the Pyridine-Water Complex. *Phys. Chem. Chem. Phys.* **2013**, *15*, 5957–5966.
- (44) Liu, X.; Sobolewski, A. L.; Domcke, W. Photoinduced Oxidation of Water in the Pyridine-Water Complex: Comparison of the Singlet and Triplet Photochemistries. *J. Phys. Chem. A* **2014**, *118*, 7788–7795.
- (45) Dunning, T. H., Jr. Gaussian Basis Sets for Use in Correlated Molecular Calculations. I. The Atoms Boron Through Neon and Hydrogen. *J. Chem. Phys.* **1989**, *90*, 1007–1023.
- (46) Schirmer, J. Beyond the Random-Phase Approximation: A New Approximation Scheme for the Polarization Propagator. *Phys. Rev. A: At., Mol., Opt. Phys.* **1982**, *26*, 2395–2416.
- (47) Trofimov, A. B.; Schirmer, J. An Efficient Polarization Propagator Approach to Valence Excitation Spectra. *J. Phys. B: At., Mol. Opt. Phys.* **1995**, *28*, 2299–2324.
- (48) Christiansen, O.; Koch, H.; Jørgensen, P. The Second-Order Approximate Coupled Cluster Singles and Doubles Model CC2. *Chem. Phys. Lett.* **1995**, *243*, 409–418.
- (49) Köhn, A.; Tajti, A. Can Coupled-Cluster Theory Treat Conical Intersections? *J. Chem. Phys.* **2007**, *127*, 044105.
- (50) Shemesh, D.; Hättig, C.; Domcke, W. Photophysics of the Trp-Gly Dipeptide: Role of Electron and Proton Transfer for Efficient Excited-State Deactivation. *Chem. Phys. Lett.* **2009**, *482*, 38–43.
- (51) Winter, N. O. C.; Graf, N. K.; Leutwyler, S.; Hättig, C. Benchmarks for 0–0 Transitions of Aromatic Organic Molecules: DFT/B3LYP, ADC(2), CC2, SOS-CC2 and SCS-CC2 Compared to High-Resolution Gas-Phase Data. *Phys. Chem. Chem. Phys.* **2013**, *15*, 6623–6630.
- (52) Dreuw, A.; Wormit, M. The Algebraic Diagrammatic Construction Scheme for the Polarization Propagator for the Calculation of Excited States. *WIREs Comput. Mol. Sci.* **2015**, *5*, 82–95.
- (53) Wormit, W.; Rehn, D. R.; Harbach, P. H. P.; Wenzel, J.; Krauter, C. M.; Epifanovsky, E.; Dreuw, A. Investigating Excited Electronic States Using the Algebraic Diagrammatic Construction (ADC) Approach of the Polarization Propagator. *Mol. Phys.* **2014**, *112*, 774–784.
- (54) Starke, J. H.; Wormit, M.; Dreuw, A. Unrestricted Algebraic Diagrammatic Construction Scheme of Second Order for the Calculation of Excited States of Medium-Sized and Large Molecules. *J. Chem. Phys.* **2009**, *130*, 024104.
- (55) TURBOMOLE, V6.6, 2014; A development of University of Karlsruhe and Forschungszentrum Karlsruhe GmbH, 1989–2007; TURBOMOLE GmbH since 2007.
- (56) Hättig, C.; Weigend, F. CC2 Excitation Energy Calculations on Large Molecules Using the Resolution of the Identity Approximation. *J. Chem. Phys.* **2000**, *113*, 5154–5161.
- (57) Lunkenheimer, B.; Köhn, A. Solvent Effects on Electronically Excited States Using the Conductor-Like Screening Model and the

Second-Order Correlated Method ADC(2). *J. Chem. Theory Comput.* **2013**, *9*, 977–994.

(58) Liu, X.; Karsili, T. N. V.; Sobolewski, A. L.; Domcke, W. Photocatalytic Water Splitting with the Acridine Chromophore: A Computational Study. *J. Phys. Chem. B* **2015**, *119*, 10664–10672.

(59) Muuronen, M.; Parker, S. M.; Berardo, E.; Le, A.; Zwijnenburg, M. A.; Furche, F. Mechanism of Photocatalytic Water Oxidation on Small TiO₂ Nanoparticles. *Chem. Sci.* **2017**, *8*, 2179–2183.

(60) Sobolewski, A. L.; Domcke, W.; Dedonder-Lardeux, C.; Jouvét, C. Excited-State Hydrogen Detachment and Hydrogen Transfer Driven by Repulsive ¹ $\pi\sigma^*$ States: A New Paradigm for Nonradiative Decay in Aromatic Biomolecules. *Phys. Chem. Chem. Phys.* **2002**, *4*, 1093–1100.

(61) Ashfold, M. N. R.; Cronin, B.; Devine, A. L.; Dixon, R. N.; Nix, M. G. D. The Role of $\pi\sigma^*$ Excited States in the Photodissociation of Heteroaromatic Molecules. *Science* **2006**, *312*, 1637–1640.

(62) Ashfold, M. N. R.; King, G. A.; Murdock, D.; Nix, M. G. D.; Oliver, T. A. A.; Sage, A. G. $\pi\sigma^*$ Excited States in Molecular Photochemistry. *Phys. Chem. Chem. Phys.* **2010**, *12*, 1218–1238.

(63) Roberts, G. M.; Stavros, V. G. The Role of $\pi\sigma^*$ States in the Photochemistry of Heteroaromatic Biomolecules and Their Subunits: Insights from Gas-Phase Femtosecond Spectroscopy. *Chem. Sci.* **2014**, *5*, 1698–1722.

(64) Ehrmaier, J.; Picconi, D.; Karsili, T. N. V.; Domcke, W. Photodissociation Dynamics of the Pyridinyl Radical: Time-Dependent Quantum Wave-Packet Simulations. *J. Chem. Phys.* **2017**, *146*, 124304.

(65) Esteves-Lopez, N.; Coussan, S.; Dedonder-Lardeux, C.; Jouvét, C. Photoinduced Water Splitting in Pyridine Water Clusters. *Phys. Chem. Chem. Phys.* **2016**, *18*, 25637–25644.

(66) Liu, X.; Karsili, T. N. V.; Sobolewski, A. L.; Domcke, W. Photocatalytic Water Splitting with Acridine Dyes: Guidelines from Computational Chemistry. *Chem. Phys.* **2016**, *464*, 78–85.

(67) Schriever, C.; Lochbrunner, S.; Ofial, A. R.; Riedle, E. The Origin of Ultrafast Proton Transfer: Multidimensional Wave Packet Motion vs. Tunneling. *Chem. Phys. Lett.* **2011**, *503*, 61–65.

(68) Lee, J.; Kim, C. H.; Joo, T. Active Role of Proton in Excited State Intramolecular Proton Transfer Reaction. *J. Phys. Chem. A* **2013**, *117*, 1400–1405.

(69) Nosaka, A. Y.; Komori, S.; Yawata, K.; Hirakawa, T.; Nosaka, Y. Photocatalytic OH Radical Formation in TiO₂ Aqueous Suspension Studied by Several Detection Methods. *Phys. Chem. Chem. Phys.* **2003**, *5*, 4731–4735.

(70) Zhang, J.; Nosaka, Y. Mechanism of the OH Radical Generation in Photocatalysis with TiO₂ of Different Crystalline Types. *J. Phys. Chem. C* **2014**, *118*, 10824–10832.

(71) Kim, W.; Tachikawa, T.; Moon, G.-H.; Majima, T.; Choi, W. Molecular-Level Understanding of the Photocatalytic Activity Difference Between Anatase and Rutile Nanoparticles. *Angew. Chem.* **2014**, *126*, 14260–14265.

(72) Morawski, O.; Izdebska, K.; Karpiuk, E.; Nowacki, J.; Suchocki, A.; Sobolewski, A. L. Photoinduced Water Splitting with Oxotitanium Tetrphenylporphyrin. *Phys. Chem. Chem. Phys.* **2014**, *16*, 15256–15262.

(73) Morawski, O.; Izdebska, I.; Karpiuk, E.; Suchocki, A.; Zhydachevskyy, Y.; Sobolewski, A. L. Titanyl Phthalocyanine as a Water Photooxidation Agent. *J. Phys. Chem. C* **2015**, *119*, 14085–14093.

(74) Lau, V. W.-H.; Klose, D.; Kasap, H.; Podjaski, F.; Pignie, M.-C.; Reisner, E.; Jeschke, G.; Lotsch, B. V. Dark Photocatalysis: Storage of Solar Energy in Carbon Nitride for Time-Delayed Hydrogen Generation. *Angew. Chem., Int. Ed.* **2017**, *56*, 510–514.

(75) Barbatti, M. Nonadiabatic Dynamics with Trajectory Surface Hopping Method. *WIREs Comput. Mol. Sci.* **2011**, *1*, 620–633.

(76) Senn, H. M.; Thiel, W. QM/MM Methods for Biomolecular Systems. *Angew. Chem., Int. Ed.* **2009**, *48*, 1198–1229.

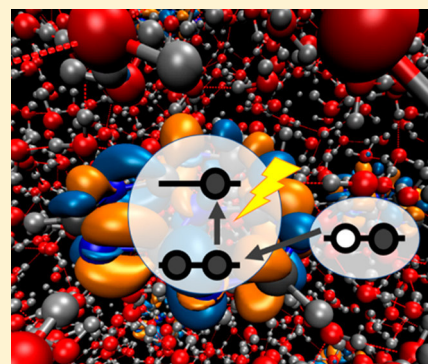
Mechanism of Photocatalytic Water Oxidation by Graphitic Carbon Nitride

Johannes Ehrmaier, Wolfgang Domcke, and Daniel Opalka*

Department of Chemistry, Technical University of Munich, Lichtenbergstr. 4, 85748 Garching, Germany

S Supporting Information

ABSTRACT: Carbon nitride materials are of great interest for photocatalytic water splitting. Herein, we report results from first-principles simulations of the specific electron- and proton-transfer processes that are involved in the photochemical oxidation of liquid water with heptazine-based molecular photocatalysts. The heptazine chromophore and the solvent molecules have been described strictly at the same level of electronic structure theory. We demonstrate the critical role of solvent molecules for the absorption properties of the chromophore and the overall photocatalytic cycle. A simple model is developed to describe the photochemical water oxidation mechanism. Our results reveal that heptazine possesses energy levels that are suitable for the water oxidation reaction. We suggest design principles for molecular photocatalysts which can be used as descriptors in future experimental and computational screening studies.



Photocatalytic water splitting has great potential to complement existing and future technologies for the production of clean and sustainable energy. Graphitic carbon nitride (CN) materials represent an alternative to traditional photocatalysts based on semiconductor materials or organometallic complexes. CN materials offer enormous flexibility with respect to the optimization of the molecular building blocks and the supramolecular structures, making use of well-established techniques of chemical synthesis. CNs are photostable and consist of earth abundant elements, and experiments have established their photocatalytic activity for the photochemical conversion of liquid water into molecular hydrogen and oxygen. In 2009, Antonietti, Domen, and co-workers reported hydrogen evolution using a CN photocatalyst, a sacrificial electron donor, and nanodisperse Pt as cocatalyst.¹ Since then, numerous studies have been published in this field, reporting in a few cases also stoichiometric hydrogen and oxygen evolution.^{2–4} Despite considerable experimental and theoretical efforts, the underlying atomistic mechanism is still not well-understood.^{5,6} It has been reported that OH radicals are generated by visible light irradiation of CN materials in water,^{7–10} which indicates a homolytic water-splitting reaction mechanism via a proton-coupled electron-transfer (PCET)^{11–13} reaction. It has also been shown that small CN oligomers generate molecular hydrogen at least as efficiently as CN polymers^{14,15} despite their substantial exciton dissociation energies.^{15,16} This observation supports the notion of a molecular photochemical reaction mechanism in which localized electronic excitations of CN building blocks oxidize adjacent water molecules.

It is established that so-called graphitic CN materials consist of heptazine (tri-s-triazine) units which are linked by imine groups.^{1–4,17} In recent theoretical work, the hydrogen-bonded

complex of heptazine with a single water molecule was considered as a model system for the exploration of the primary photochemical reactions involved in water splitting.¹⁸ It was shown that photoexcited heptazine may abstract an H atom from a hydrogen-bonded water molecule by sequential electron/proton-transfer reactions. The products of this photochemical reaction are a heptazinyl (N-hydrogenated heptazine) radical and an OH radical in their respective electronic ground states. The calculations provided evidence that the transferred H atom can be photodetached from the heptazinyl radical by an additional photon, resulting in the formation of atomic hydrogen. A water molecule is thus decomposed into a hydroxyl radical and atomic hydrogen in a biphotonic photochemical reaction.¹⁸

In this work, the electronic energy levels of heptazine, the building block of most CN materials, in bulk liquid water were investigated with first-principles simulations. Redox processes such as the oxidation of water require appropriately aligned energy levels of the reactants. According to the established band structure model of semiconductor photocatalysts, an electron is excited from the valence band of the photocatalyst to the conduction band, where charge carriers can attain high mobility. If the valence band maximum with the electron vacancy (hole) is at lower energy (that is, more positive potential vs standard hydrogen electrode) than the oxidation potential of liquid water, the transfer of an electron from a water molecule to the catalyst is considered to be thermodynamically feasible. Molecular catalysts such as heptazine units in CN structures are characterized by discrete

Received: June 28, 2018

Accepted: August 1, 2018

Published: August 1, 2018

energy levels rather than a band structure. Nevertheless, in analogy to the band structure model of semiconductor photocatalysis, the highest occupied molecular orbital (HOMO) of the molecular catalyst must be at lower energy than the valence band of liquid water for the photoinduced water-oxidation reaction to occur.

Our model system consists of a single heptazine molecule solvated in 120 water molecules with periodic boundary conditions to model bulk water. We used ab initio molecular dynamics simulations to follow the evolution of the equilibrated system for 10 ps. To account for the fluctuating structure of the liquid phase, the excited-state properties and the electronic density of states were computed with density functional theory (DFT) every 125 fs. The computational methods are described in section 1 of the [Supporting Information](#). Details of the structural properties of solvated heptazine are discussed in section 2 of the [Supporting Information](#).

Figure 1 shows the total electronic density of states (DOS) of the system (blue line) and the projected density of states of

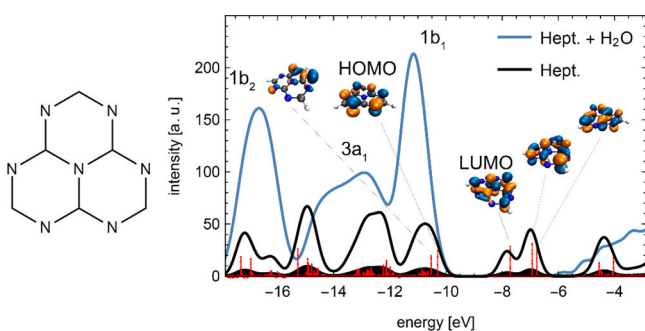


Figure 1. Averaged total density of states of the heptazine/water system (blue line) and the averaged projected density of states for the heptazine molecule (black line, multiplied by 7 for clarity). The red sticks show the orbital energies of the heptazine. The chemical structure of heptazine is shown on the left.

the heptazine molecule (black line) averaged over all snapshots. The maximum of the $1b_1$ highest occupied band of liquid water is found experimentally at -11.16 eV vs vacuum (6.7 V vs RHE) with an onset at -9.9 eV.¹⁹ The projected DOS of the heptazine molecule shows two features which are critical for efficient photocatalytic water oxidation. The HOMO of heptazine is energetically only about ~ 0.4 eV below the valence band maximum of the solvent, i.e. ~ 0.4 eV below the energy of the HOMO of water. This near-degeneracy of orbitals indicates that solute and solvent

electronic states may be coupled, which implies that a consistent description of both at the same level of electronic structure theory is required. Moreover, two unoccupied solute bands have been identified within the band gap of water at -7.82 and -7.00 eV (**Figure 1**). **Figure 2** shows the HOMO (left) and the lowest unoccupied molecular orbital (LUMO) (right) of heptazine which can be classified as π type orbitals. For clarity, the HOMO and LUMO of the hydrogen-bonded complex of heptazine with a single water molecule are shown in **Figure S6** of the [Supporting Information](#). It can be seen that the HOMO is exclusively localized at the peripheral N atoms of heptazine, while the LUMO is localized exclusively at the C atoms. These qualitative features of the electronic DOS are preserved along the molecular dynamics trajectory.

An essential prerequisite for the efficient conversion of light to chemical energy is the absorption of light which triggers the relevant electronic excitation in the photocatalyst. Efficient photocatalysts for photochemical water splitting should absorb light in the spectral range of $2\text{--}3$ eV to provide sufficient energy for the water oxidation, which requires a thermoneutral potential of 1.48 V, and to be compatible with the intensity distribution of the solar spectrum. In a first approximation, the excitation of a heptazine unit by the absorption of a photon can be interpreted in the single-particle picture on the basis of the electronic density of states. Excitation of an electron from the HOMO to the LUMO of heptazine forms a $\pi\pi^*$ state. This excitation generates extremely electron-deficient peripheral N atoms. The hole in the HOMO of the heptazine molecule, which corresponds to a hole state in the band structure model of semiconductor catalysts, can be filled by the transfer of an electron from the hydrogen-bonded water molecule to heptazine. The oxidation of water is thermodynamically feasible because the valence band maximum of water is quasi-degenerate with the HOMO of heptazine (**Figure 1**). The $n\pi^*$ states of heptazine need not be considered in this discussion, because the optically dark $n\pi^*$ states are located more than one electronvolt above the lowest $\pi\pi^*$ state.¹⁸

We have used time-dependent density functional theory to compute the ultraviolet–visible (UV–vis) absorption spectrum of our model system representing a fully solvated heptazine molecule in a bulk water environment (see section 1 of the [Supporting Information](#) for the computational methods). The inset of **Figure 3** displays the computed spectrum of the system for one representative snapshot along the molecular dynamics trajectory. While a single snapshot is clearly insufficient for a description of the fluctuating solvent environment, the fundamental features of the absorption spectrum and the assignment of the electronic transitions do

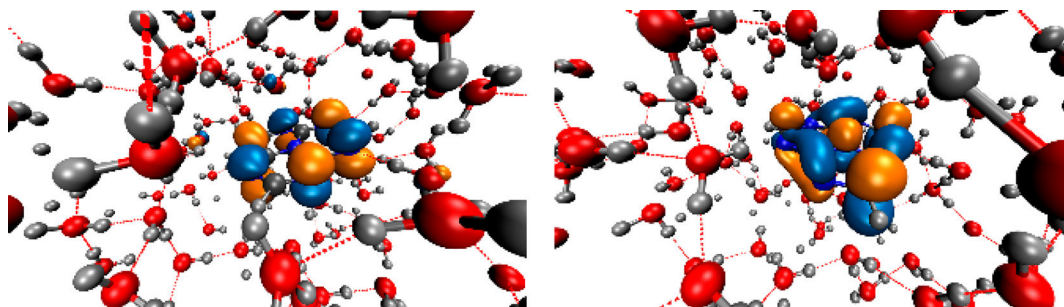


Figure 2. HOMO (left) and LUMO (right) of the solvated heptazine molecule. While the HOMO is localized at the N atoms, the LUMO density is found at the C atoms of the heptazine molecule. A more detailed illustration is provided in **Figure S6** of the [Supporting Information](#).

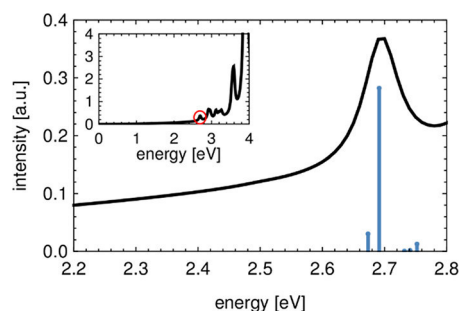


Figure 3. Onset of the absorption spectrum of heptazine in aqueous solution. Blue sticks: computed electronic transition energies. Black line: spectral envelope after convolution with a Gaussian broadening function. Inset: UV-vis absorption spectrum of a solvated heptazine molecule up to 4.0 eV. The red circle indicates the onset of the absorption spectrum shown in the main graph.

not change because of solvent fluctuations. Hence, for the sake of clarity, our results are discussed for a single structure. This structure is shown in the left frame of Figure S3 of the Supporting Information. It can be seen that a single water molecule forms a hydrogen bond with one of the peripheral N atoms of heptazine. For the statistical analysis (radial distribution functions, distribution of hydrogen bonds), we refer to section 4 of the Supporting Information. The lowest-energy electronic transition (marked by the red circle in the inset of Figure 3) is located at about 2.7 eV and is shown on an enlarged scale in the main graph. The major contribution to the intensity of this band arises from the lowest local $\pi \rightarrow \pi^*$ excitation on heptazine. For isolated heptazine, the HOMO-to-LUMO transition is symmetry-forbidden in D_{3h} symmetry in the dipole approximation. However, the strict symmetry selection rules of the isolated chromophore are relaxed in the presence of the solvent, because the symmetry is reduced by the environment. This leads to a nonvanishing oscillator strength, and the lowest singlet $\pi\pi^*$ state of solvated heptazine can be populated by the absorption of a photon.

To reveal the statistical fluctuations due to the solvent, the $\pi\pi^*$ excitation energy has been examined for multiple snapshots along the trajectory. Figure 4 shows the distribution

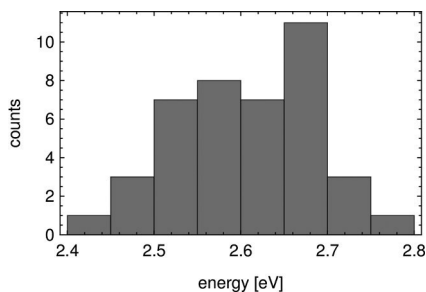


Figure 4. Distribution of the $\pi\pi^*$ excitation energies of the different snapshots.

of the excitation energies of the lowest $\pi\pi^*$ state for the different snapshots. We find a mean absorption energy of 2.6 eV (477 nm), which is in very good agreement with experimental results for heptazine-based carbon nitride polymers.^{1–4} The width of the distribution is about 0.2 eV. Our findings for the energy and intensity of the HOMO–LUMO transition in solvated heptazine are also in very good

agreement with recent GW-BSE results for crystalline $g\text{-C}_3\text{N}_4$ sheets with hydrogen-bonded water.²⁰

When the HOMO orbital of heptazine becomes degenerate with the 1b_1 orbital of water by a fluctuation of the solvent, photoexcited heptazine can pull an electron from the hydrogen-bonded water molecule in an ultrafast resonant electron-transfer process. This oxidation of a water molecule and the formation of a heptazine anion represent the initial step of the photocatalyzed water-splitting reaction. However, significant turnover rates can be expected only if the charged intermediates are rapidly stabilized and reverse electron transfer is inhibited. In earlier work, electron-driven proton transfer from the oxidized water molecule to the chromophore anion was identified as a mechanism that typically occurs on a femtosecond time scale and can efficiently stabilize the reaction products of the primary electron transfer.¹⁸ To explore the energetics of the coupled electron/proton-transfer reaction for heptazine embedded in a large water environment, we have analyzed the DOS of the solute and the solvent along an approximate reaction coordinate describing the transfer of a proton from a hydrogen-bonded water molecule to the N atom of heptazine. The reaction coordinate was approximated as the distance between the N atom of heptazine and the H atom of the hydrogen-bonded water molecule. For large NH distances ($R_{\text{NH}} \approx 2.0$ Å, middle part of Figure 5), the H atom is covalently bound to the water molecule. With decreasing NH distance, the hydrogen atom is transferred to the N atom of heptazine molecule. For small values of the NH distance ($R_{\text{NH}} \approx 1.0$ Å), the H atom is covalently bonded to the N atom of heptazine and two radicals, the hydroxyl radical and the

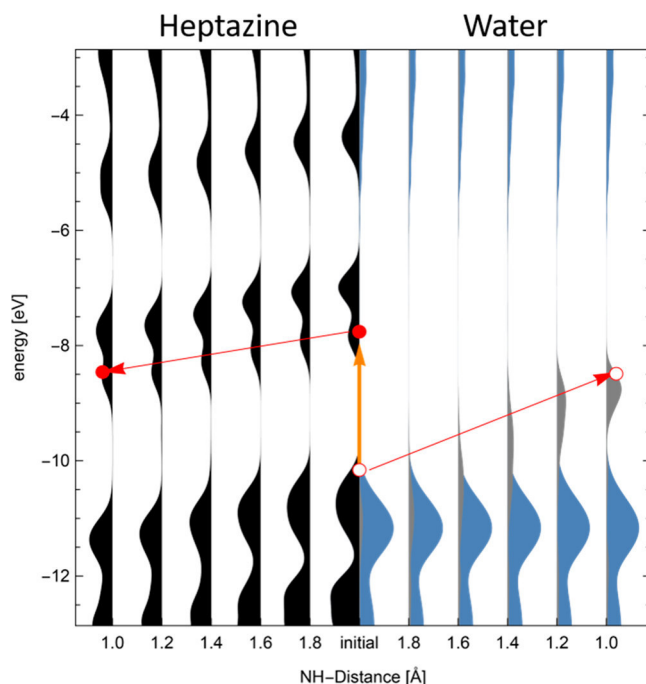


Figure 5. Averaged projected DOS for water and heptazine along the reaction coordinate for H atom transfer from water to heptazine. The orange arrow indicates the photoexcitation of an electron hole pair at the equilibrium geometry of heptazine. The red arrows schematically indicate the decrease of the energy of the singly occupied LUMO of heptazine (left) and the increase of the energy of the hole in the valence band of water (right). These gradients provide the driving force for the H atom-transfer reaction.

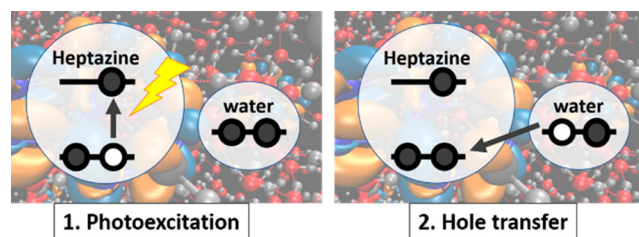
heptazinyl radical, are formed. While this linearly interpolated reaction path is not the true minimum-energy reaction path, it provides a qualitative description of the energetics of the reaction.

Figure 5 shows the projected DOS of water (blue, right part of Figure 5) of the emerging OH radical (gray, right part of Figure 5) and of heptazine (black, left part of Figure 5) along the linearly interpolated reaction coordinate between the equilibrium structure in the electronic ground state ($R_{\text{NH}} \approx 2.0$ Å, middle) up to NH-distances of 1.0 Å, averaged over all snapshots. Along the reaction coordinate for the proton transfer, the energy levels of the HOMO and the LUMO of heptazine both decrease by about 0.6 eV. On the other hand, the valence band edge of the solvent, which is now determined by the OH radical, rises by about 1.4 eV (Figure 5).

The reaction mechanism suggested by the calculations can be briefly summarized as follows (more details are given in section 5 of the Supporting Information). Photoexcitation of heptazine to the lowest singlet $\pi\pi^*$ state leads to the creation of an electron hole pair (orange arrow in Figure 5) in the HOMO and LUMO of heptazine. The electron vacancy in the HOMO has sufficient oxidizing strength to oxidize a water molecule which is attached to heptazine by a hydrogen bond. The electron transfer from the water molecule to heptazine is followed by the ultrafast transfer of the proton involved in the hydrogen bond (the proton follows the electron), which results in heptazinyl and hydroxyl free radicals. The photocatalytic cycle can be closed by the spontaneous recombination of two photogenerated heptazinyl radicals to form H_2 . The dissociation energy of heptazinyl radicals was computed as 2.0 eV,¹⁸ while the dissociation energy (D_e) of H_2 is 4.6 eV. The radical recombination reaction is thus exoenergetic and can occur in a dark reaction. Alternatively, free hydrogen radicals can be generated by the photodetachment of the excess H atom from the heptazinyl radical.¹⁸ Free hydrogen and hydroxyl radicals were indeed experimentally detected after irradiation of an aqueous solution of CN at 405 nm.²¹

In summary, our computational analysis of the electronic absorption spectrum of solvated heptazine reveals a weak absorption band near 2.6 eV (477 nm). The electronic excitation is assigned to the promotion of an electron from the HOMO to the LUMO of the solvated heptazine molecule. While the transition is symmetry-forbidden at the equilibrium geometry of isolated heptazine, it acquires oscillator strength in solution due to the lowering of the symmetry by the solvent molecules. On the basis of the present analysis and previous calculations for the heptazine– H_2O complex, we propose a detailed mechanism for the photochemical water oxidation reaction as illustrated in Scheme 1. After the initial local photoexcitation of the heptazine molecule, the hole in the HOMO of heptazine is transferred to the nearby (hydrogen-bonded) water molecule. This electronic charge separation in turn drives a proton-transfer reaction which neutralizes the electronic charge separation. The sequential electron/proton-transfer reactions result in the formation of a hydroxyl radical and a heptazinyl radical in their electronic ground states. The electronic transition near 2.6 eV (477 nm) in heptazine-based polymers in aqueous solution provides sufficient energy for the formation of hydroxyl radicals and reduced heptazine via the homolytic splitting of a water molecule. This theoretical model explains experimental in situ observations of photogenerated hydroxyl radicals in irradiated CN solutions.^{7–10,21} It supports the paradigm of a localized (molecular) character of the

Scheme 1. : Proposed Mechanism of Water Oxidation by Photoexcited Heptazine^a



^a(1) An electron is excited from the HOMO to the LUMO of heptazine, forming a hole in the HOMO. (2) The hole in the HOMO is filled by an electron from an energetically higher orbital of a hydrogen-bonded water molecule, resulting in a hole transfer from heptazine to water.

reaction, that is, the catalytic reaction mechanism is determined by single molecular CN chromophores. In this picture, efficient CN photocatalysts are characterized by a HOMO near the valence band maximum of liquid water and a local electronic transition in the chromophore in the range of 2–3 eV. The size and relative position of the CN HOMO–LUMO gap with respect to bulk water, which can be computed with relatively inexpensive semilocal DFT methods, may serve as a descriptor model for future screening studies. The present computational results extend the results of earlier high-level electronic-structure calculations for the complex of heptazine with a single water molecule in vacuum¹⁸ toward a realistic simulation of an aqueous environment. In the future, excited-state nonadiabatic dynamics simulations should be performed to obtain information on the time scales of the decisive processes involved in the water oxidation and hydrogen evolution reactions.

From a thermodynamic perspective, CN materials show great promise for the efficient conversion of solar energy to chemical energy. The flexibility of CNs offers substantial potential for improvement of the catalytic performance by optimization of their molecular structure, morphology, and optical properties. For example, it should be straightforward to lower the decisive barrier for H atom transfer from water to the chromophore by the substitution of heptazine with electron-withdrawing groups.

■ COMPUTATIONAL METHODS

Ab initio molecular dynamics simulations were performed for a system of one heptazine molecule surrounded by 120 water molecules with periodic boundary conditions. Solute and solvent both were treated at the same level of density functional theory (DFT) using the Perdew–Burke–Ernzerhof (PBE) functional. After equilibration, the system was propagated for 10 ps to sample the fluctuating solvent environment. At several snapshots of the trajectory, the density of states, orbitals, and vertical excitation energies were computed using time-dependent DFT. Data from multiple snapshots have been averaged for statistical sampling of the thermal fluctuations of water. Further details about the calculations and data analysis are provided in the Supporting Information.

■ ASSOCIATED CONTENT**■ Supporting Information**

The Supporting Information is available free of charge on the ACS Publications website at DOI: 10.1021/acs.jpcl.8b02026.

Computational details and statistical analysis (PDF)

■ AUTHOR INFORMATION**Corresponding Author**

*E-mail: daniel.opalka@tum.de.

Notes

The authors declare no competing financial interest.

■ ACKNOWLEDGMENTS

The authors are grateful to the Gauss Centre for Supercomputing e.V. (www.gauss-centre.eu) for providing the computing resources for this project on the GCS Supercomputer SuperMUC at the Leibniz Supercomputing Centre (www.lrz.de). This work has been supported by the Munich Centre for Advanced Photonics (MAP). J.E. also acknowledges support by the International Max Planck Research School of Advanced Photon Science (IMPRS-APS).

■ REFERENCES

- (1) Wang, X.; Maeda, K.; Thomas, A.; Takanabe, K.; Xin, G.; Carlsson, J. M.; Domen, K.; Antonietti, M. A metal-free polymeric photocatalyst for hydrogen production from water under visible light. *Nat. Mater.* **2009**, *8*, 76.
- (2) Ong, W.-J.; Tan, L.-L.; Ng, Y. H.; Yong, S.-T.; Chai, S.-P. Graphitic carbon nitride (g-C₃N₄)-based photocatalysts for artificial photosynthesis and environmental remediation: Are we a step closer to achieving sustainability? *Chem. Rev.* **2016**, *116*, 7159–7329.
- (3) Liu, J.; Liu, Y.; Liu, N.; Han, Y.; Zhang, X.; Huang, H.; Lifshitz, Y.; Lee, S.-T.; Zhong, J.; Kang, Z. Metal-free efficient photocatalyst for stable visible water splitting via a two-electron pathway. *Science* **2015**, *347*, 970–974.
- (4) Lau, V. W.-H.; Moudrakovski, I.; Botari, T.; Weinberger, S.; Mesch, M. B.; Duppel, V.; Senker, J.; Blum, V.; Lotsch, B. V. Rational design of carbon nitride photocatalysts by identification of cyanamide defects as catalytically relevant sites. *Nat. Commun.* **2016**, *7*, 12165.
- (5) Sprick, R. S.; Jiang, J.-X.; Bonillo, B.; Ren, S.; Ratvijitvech, T.; Guiglion, P.; Zwijnenburg, M. A.; Adams, D. J.; Cooper, A. I. Tunable organic photocatalysts for visible-light-driven hydrogen evolution. *J. Am. Chem. Soc.* **2015**, *137*, 3265–3270.
- (6) Wirth, J.; Neumann, R.; Antonietti, M.; Saalfrank, P. Adsorption and photocatalytic splitting of water on graphitic carbon nitride: a combined first principles and semiempirical study. *Phys. Chem. Chem. Phys.* **2014**, *16*, 15917–15926.
- (7) Liu, G.; Niu, P.; Sun, C.; Smith, S. C.; Chen, Z.; Lu, G. Q.; Cheng, H.-M. Unique electronic structure induced high photo-reactivity of sulfur-doped graphitic C₃N₄. *J. Am. Chem. Soc.* **2010**, *132*, 11642–11648.
- (8) Niu, P.; Zhang, L.; Liu, G.; Cheng, H. M. Graphene-like carbon nitride nanosheets for improved photocatalytic activities. *Adv. Funct. Mater.* **2012**, *22* (22), 4763–4770.
- (9) She, X.; Liu, L.; Ji, H.; Mo, Z.; Li, Y.; Huang, L.; Du, D.; Xu, H.; Li, H. Template-free synthesis of 2D porous ultrathin nonmetal-doped g-C₃N₄ nanosheets with highly efficient photocatalytic H₂ evolution from water under visible light. *Appl. Catal., B* **2016**, *187*, 144–153.
- (10) Huang, K.; Hong, Y.; Yan, X.; Huang, C.; Chen, J.; Chen, M.; Shi, W.; Liu, C. Hydrothermal synthesis of g-C₃N₄/CdWO₄ nanocomposite and enhanced photocatalytic activity for tetracycline degradation under visible light. *CrystEngComm* **2016**, *18*, 6453–6463.

(11) Gagliardi, C. J.; Vannucci, A. K.; Concepcion, J. J.; Chen, Z.; Meyer, T. J. The Role of Proton Coupled Electron Transfer in Water Oxidation. *Energy Environ. Sci.* **2012**, *5*, 7704–7717.

(12) Goyal, P.; Hammes-Schiffer, S. Tuning the Ultrafast Dynamics of Photoinduced Proton-Coupled Electron Transfer in Energy Conversion Processes. *ACS Energy Lett.* **2017**, *2*, 512–519.

(13) Lennox, J. C.; Kurtz, D. A.; Huang, T.; Dempsey, J. L. Excited-State Proton-Coupled Electron Transfer: Different Avenues for Promoting Proton/Electron Movement with Solar Photons. *ACS Energy Lett.* **2017**, *2*, 1246–1256.

(14) Lau, V. W.-H.; Mesch, M. B.; Duppel, V.; Blum, V.; Senker, J.; Lotsch, B. V. Low-molecular-weight carbon nitrides for solar hydrogen evolution. *J. Am. Chem. Soc.* **2015**, *137*, 1064–1072.

(15) Merschjann, C.; Tyborski, T.; Orthmann, S.; Yang, F.; Schwarzburg, K.; Lublow, M.; Lux-Steiner, M.-C.; Schedel-Niedrig, T. Photophysics of polymeric carbon nitride: An optical quasimonomer. *Phys. Rev. B: Condens. Matter Mater. Phys.* **2013**, *87*, 205204.

(16) Wei, W.; Jacob, T. Strong excitonic effects in the optical properties of graphitic carbon nitride g-C₃N₄ from first principles. *Phys. Rev. B: Condens. Matter Mater. Phys.* **2013**, *87* (8), 085202.

(17) Lotsch, B. V.; Döblinger, M.; Sehnert, J.; Seyfarth, L.; Senker, J.; Oeckler, O.; Schnick, W.; Unmasking Melon by a Complementary Approach Employing Electron Diffraction, Solid-State NMR Spectroscopy, and Theoretical Calculations—Structural Characterization of a Carbon Nitride Polymer. *Chem. - Eur. J.* **2007**, *13*, 4969–4980.

(18) Ehrmaier, J.; Karsili, T. N.; Sobolewski, A. L.; Domcke, W. On the Mechanism of Photocatalytic Water Splitting with Graphitic Carbon Nitride: Photochemistry of the Heptazine-Water Complex. *J. Phys. Chem. A* **2017**, *121*, 4754–4764.

(19) Winter, B.; Faubel, M. Photoemission from liquid aqueous solutions. *Chem. Rev.* **2006**, *106*, 1176–1211.

(20) Sun, J.; Li, X.; Yang, J. The Roles of Buckled Geometry and Water Environment on the Excitonic Properties of graphitic C₃N₄. *Nanoscale* **2018**, *10*, 3738–3743.

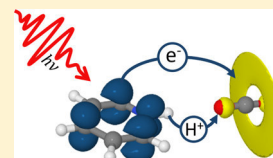
(21) Morawski, O.; Ehrmaier, A.; Ehrmaier, J.; Schropp, E.; Khare, R.; Ehrmaier, B.; Lercher, J. A.; Sobolewski, A. L.; Domcke, W. Photochemical water splitting with carbon nitride: Spectroscopic detection of photogenerated hydrogen and hydroxyl radicals. *Sust. Energy & Fuels*, **2018**, in press.

Role of the Pyridinyl Radical in the Light-Driven Reduction of Carbon Dioxide: A First-Principles Study

Johannes Ehrmaier,[†] Andrzej L. Sobolewski,[‡] and Wolfgang Domcke^{*,†}[†]Department of Chemistry, Technical University of Munich, D-85747 Garching, Germany[‡]Institute of Physics, Polish Academy of Sciences, PL-02-668 Warsaw, Poland

S Supporting Information

ABSTRACT: The reduction of carbon dioxide to fuels or chemical feedstocks with solar energy is one of the grand goals of current chemistry. In recent years, electrochemical, photoelectrochemical, and photochemical experiments provided hints of an unexpected catalytic role of the pyridine molecule in the reduction of carbon dioxide to formic acid or methanol. In particular, it has been suggested that the 1-pyridinyl radical (PyH) may be able to reduce carbon dioxide to the hydroxy-formyl radical. However, extensive theoretical studies of the thermodynamics and kinetics of the reaction called this interpretation of the experimental observations into question. Using ab initio computational methods, we investigated the photochemistry of the hydrogen-bonded PyH...CO₂ complex. Our results reveal that carbon dioxide can be reduced to the hydroxy-formyl radical by a proton-coupled electron-transfer (PCET) reaction in excited states of the PyH...CO₂ complex. In contrast to the ground-state PCET reaction, which exhibits a substantial barrier, the excited-state PCET reaction is barrierless but requires the passage through two conical intersections. Our results provide a tentative explanation of the catalytic role of the PyH radical in the reduction of CO₂ with the qualification that the absorption of a photon by PyH is necessary.



I. INTRODUCTION

A key element of a future carbon-neutral energy economy will be the solar-driven reduction of carbon dioxide to liquid fuels and valuable chemical feedstocks. The reduction of carbon dioxide is challenging due to the extreme stability of the CO₂ molecule. There exists an extensive literature on the electrochemical, photochemical, and photoelectrochemical reduction of CO₂ (see refs 1–3 for recent reviews).

In 1994, Bocarsly and co-workers reported evidence of an unexpected catalytic function of the pyridine (Py) molecule in the electrochemical reduction of CO₂ on a Pd electrode.⁴ A simple homogeneous reaction mechanism was proposed that involves the protonation of Py (pK_a = 5.25) to the pyridinium cation (C₅H₅NH⁺), the electrooxidation of pyridinium to the neutral 1-pyridinyl radical (C₅H₅NH, henceforth pyridinyl, PyH), and the reduction of CO₂ by PyH to the hydroxy-formyl radical (HOCO). In 2008 and 2012, they showed that light-driven Py-catalyzed selective reduction of CO₂ to methanol occurs in a photoelectrochemical cell with a p-type semiconductor electrode (GaP) with 100% faradaic efficiency and no overpotentials.^{5,6} The GaP electrode was illuminated with a tunable light source. The photoaction spectrum for methanol formation showed an onset near 440 nm and a peak near 365 nm.⁵ In subsequent work, a carbamate (Py-OCOH) complex was postulated as an intermediate species, and the subsequent reduction steps toward methanol were discussed.^{7,8}

These results and their interpretation stimulated a significant number of computational studies on the reduction of CO₂ by the PyH radical. Keith and Carter ruled out the homogeneous reduction of CO₂ by the PyH radical based on first-principles simulations of the thermodynamics.^{9,10} The atomic-scale

mechanisms of the reaction driven by electrons from an illuminated electrode were also extensively scrutinized by Carter and co-workers with advanced computational methods. It has been suggested that either an adsorbed dihydropyridine or a surface-bound hydride (H⁻) is involved in the two-electron reduction of CO₂, and detailed mechanistic models have been developed.^{11–19} Musgrave and co-workers, on the other hand, demonstrated that the reaction barrier for proton-coupled electron transfer (PCET) from PyH to CO₂ is substantially lowered by water wires, rendering the homogeneous reduction of CO₂ by PyH feasible.²⁰ Keith and Carter²¹ as well as Musgrave and co-workers²² suggested that a dihydropyridine species may catalyze a two-electron transfer reaction to yield formic acid as a closed-shell product. In subsequent work, the role of the Pd or Pt electrode in Py-supported electrocatalysis has been controversially discussed. While Musgrave and co-workers advocated a homogeneous two-electron reaction mechanism via a dihydropyridine, Batista and co-workers suggested an active mechanistic role of the cathode in the catalysis.²³ The hydrogen-bonded PyH...Py complex also has been suggested as a possible intermediate species in the homogeneous electrocatalytic reduction of CO₂.²⁴

Recently, Colussi and co-workers reported homogeneous reduction of CO₂ to various products in deaerated aqueous solutions of Py, 2-propanol, and CO₂, initiated by 254 nm irradiation.²⁵ 2-Propanol served as a sacrificial electron donor

Received: February 8, 2019

Revised: April 2, 2019

Published: April 8, 2019

for the photoreduction of Py to the PyH radical. The products were detected by electrospray mass spectrometry and included, in particular, the Py-COOH radical, which provided evidence that the photogenerated PyH radical reacts homogeneously with CO₂. No evidence of dihydropyridine or the PyH...Py complex was found.²⁵ Their observations suggest that PyH may act as a homogeneous catalyst in the photoreduction of CO₂.

Herein, we are concerned with the light-driven reduction of CO₂ and refer in what follows to the photochemical and photoelectrochemical experiments mentioned above. In none of the discussions of photochemical or photoelectrochemical light-driven reduction of CO₂,^{5,6,11–19,25} it was taken in consideration that the PyH radical may act as a chromophore, absorbing UV or visible photons and reacting with CO₂ in excited electronic states. The free PyH radical was recently generated in a mixed Py/H₂ supersonic expansion by an electric discharge, and its ionization potential and the electronic excitation energies in the range of 450 to 300 nm were determined and assigned.²⁶ It was shown by mass spectrometry that PyH...(H₂O)_{n-1}OH biradicals are formed upon 255 nm excitation of Py...(H₂O)_n clusters for $n > 3$.²⁶ Moreover, it has been observed that the nitrogen-bound H atom of PyH can be photodetached with 255 nm radiation.²⁶ These findings prove that the PyH radical absorbs UV light and that it is photochemically reactive. Remarkably, the onset of the photoaction spectrum for methanol formation in a photoelectrochemical cell (440 nm, 2.82 eV)⁵ is in good agreement with the lowest absorption band of the PyH radical in a supersonic jet (426 nm, 2.91 eV).²⁶

The mechanism of the photodetachment reaction of PyH has been clarified by a computational study by Ehrmaier et al.²⁷ It was shown that the ² $\pi\pi^*$ excited states of PyH are predissociated via conical intersections by a ² $\pi\sigma^*$ excited state, which is repulsive with respect to the NH bond. Ab initio time-dependent wave-packet simulations for a reduced-dimensional model of PyH revealed a fast (nonstatistical) and efficient photodetachment reaction.²⁷ When PyH is excited at 254 nm,²⁵ the kinetic energy of the photodetached ground-state H atom is about 2.9 eV.²⁷ While this energy is sufficient for H-atom attachment to CO₂, the free H atom is not suitable for reduction of CO₂ since the 1s orbital of the H atom is too compact for transfer to the unoccupied orbitals of CO₂. However, we hypothesize that the reduction of CO₂ may be feasible by an excited-state PCET reaction in the hydrogen-bonded PyH...OCO complex, taking advantage of the diffuse (Rydberg-like) character of the σ^* orbital of the ² $\pi\sigma^*$ excited state of PyH.²⁷

In the present work, we explored the photochemistry of the hydrogen-bonded PyH...OCO complex with ab initio wave-function-based electronic structure calculations. We determined minimum-energy reaction paths and their energy profiles for the excited-state PCET reaction from PyH to CO₂. In addition, two-dimensional relaxed potential energy (PE) surfaces were computed, including the bending coordinate of CO₂ in addition to the H-atom-transfer coordinate. Our results reveal that the formation of the hydroxy-formyl radical in the ² $\pi\sigma^*$ excited state of the PyH...OCO complex is a barrierless reaction but requires the passage through two conical intersections of the ² $\pi\sigma^*$ state with a nonreactive ² $\pi\pi^*$ excited state and with the electronic ground state. These conical intersections have to be passed diabatically for a successful PCET reaction. As is typical for photochemical

reactions, the feasibility of the reaction is governed by (ultrafast) nonadiabatic dynamics at conical intersections rather than by (slow) barrier-crossing dynamics.

We focus in the present communication on the initial one-electron reduction step from CO₂ to the HOCO radical, which is by far the most endoenergetic and kinetically most difficult step, as it requires bending of the extremely stiff OCO molecule. As discussed, for example, in ref 7, the ensuing five one-electron reductions to methanol are much easier and can be achieved by H-atom transfer reactions from PyH radicals to reduced CO₂ species in the electronic ground state.

II. COMPUTATIONAL METHODS

The ground-state equilibrium geometry of the PyH...OCO complex was optimized with the unrestricted second-order Møller–Plesset method (UMP2) without symmetry constraints. The vertical excitation energies of the PyH...OCO complex were computed with the unrestricted second-order algebraic-diagrammatic construction (UADC(2)) method using the resolution of identity (RI) approximation.^{28–30} For benchmarking purposes, the vertical excitation energies at the UMP2 equilibrium geometry were also computed with the unrestricted equation-of-motion singles-and-doubles coupled-cluster (UEOM-CCSD) method³¹ and with the complete-active-space self-consistent-field (CASSCF) method augmented by second-order perturbation theory (CASPT2).³² The active space for the CASSCF calculation of vertical excitation energies consists of the two highest doubly occupied π orbitals, the singly occupied π orbital, the five lowest unoccupied π^* orbitals, and eight σ^* orbitals. While the occupied active orbitals are all located on the pyridinyl radical, specifically one diffuse σ^* orbital exhibits density on the CO₂ molecule. In total, the active space comprises 5 electrons in 16 orbitals. This rather large active orbital space including many unoccupied orbitals is necessary to describe the dense set of excited states of the PyH radical in the PyH...CO₂ complex. These states arise mostly from excitations of the electron in the singly occupied π orbital to σ^* and π^* virtual orbitals of PyH. This active space has been carefully selected, guided by the orbital character of the excited states obtained with the UADC(2) method. It is similar to the active space used for the calculation of the vertical excitation energies of the isolated PyH radical.²⁷ The CASSCF calculations were performed as state-averaged calculations including eight states of A' symmetry and five states of A'' symmetry, using equal weights for all states of a given symmetry. For the CASPT2 calculations, a standard level shift of 0.3 au was applied to avoid problems with intruder states.

For geometry optimizations of the PyH...CO₂ complex in the ² $\pi\pi^*$ and ² $\pi\sigma^*$ excited states, it is generally necessary to impose C_s symmetry to avoid collapse of the wave function to the ground state or other excited states. All excited-state geometry optimizations were therefore performed with the C_s symmetry constraint. The geometry of the reaction product, the Py...HOCO complex, was obtained by optimizing the energy of the ² $\pi\sigma^*$ state at the UMP2 level.

A two-dimensional relaxed PE surface of the ² $\pi\sigma^*$ state was calculated at the UADC(2) level. The OH distance and the OCO angle of the HOCO radical were taken as reaction coordinates. For fixed values of these coordinates, the energy of the ² $\pi\sigma^*$ state was optimized with the C_s symmetry constraint. To improve convergence, it was additionally enforced that the donating N atom, the transferred H atom,

and the accepting O atom stay on a line. All other degrees of freedom were relaxed. In addition, a linearly interpolated scan connecting the educt and product geometries was constructed. The relaxed energies of the electronic ground state, the ${}^2\pi\pi^*$ state, and the ${}^2\pi\sigma^*$ state were calculated along this linear cut.

The two-dimensional relaxed PE surface and energy profiles along the linear cut from the educt geometry to the product geometry were also computed with the CASSCF/CASPT2 method to ensure the reliability of the single-reference UADC(2) method. The active space used for these benchmark calculations is described in the [Supporting Information](#).

All calculations were performed using Dunning's augmented correlation-consistent double- ζ basis set (aug-cc-pVDZ) for all atoms.³³ The UMP2 and UADC(2) calculations were performed with the TURBOMOLE program package.³⁴ The EOM-CCSD energies were calculated with Q-Chem.³⁵ The CASSCF/CASPT2 calculations were performed using MOLPRO.³⁶

III. RESULTS

A. Ground-State Geometry and Vertical Excitation Energies. The ground-state equilibrium geometry of the PyH \cdots CO₂ complex optimized without symmetry constraints is shown in [Figure 1a](#). It is planar. A hydrogen-bond length of 2.204 Å indicates a hydrogen bond of intermediate strength, slightly weaker than the Py \cdots H₂O hydrogen bond.

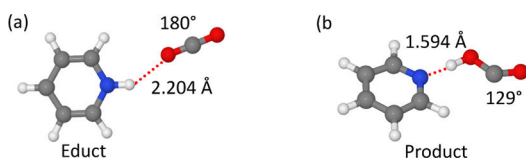


Figure 1. Educt (a) and product (b) geometries of the PyH \cdots CO₂ complex optimized at the UMP2 level.

The 12 lowest vertical excitation energies of the PyH \cdots CO₂ complex (up to 4.6 eV) calculated with the UADC(2), UCC2, UEOM-CCSD, and CASPT2 methods and the aug-cc-pVDZ basis set are given in [Table 1](#). The augmentation of the basis set is essential for the PyH radical due to the diffuseness of the virtual orbitals. The UADC(2) and UCC2 calculations were performed, in addition, with the aug-cc-pVTZ basis set. These excitation energies deviate by less than 0.2 eV from those obtained with the double- ζ basis set, most of them even less

than 0.1 eV. As expected, the UCC2 energies are very similar to the UADC(2) energies. Comparing the excitation energies obtained with different methods, the largest difference is found for the D₁ state calculated at the CASPT2 level, which is significantly lower (1.33 eV) than the excitation energies obtained with the other methods (1.71–1.86 eV). We will focus on the UADC(2) results in the following discussion.

There is a rather densely spaced set of ${}^2\pi\sigma^*$ and ${}^2\pi\pi^*$ excited states. The lowest excited states (D₁, D₂) correspond to the excitation of the electron from the singly occupied molecular orbital (SOMO) of PyH to the lowest π^* orbital and the lowest σ^* orbital, respectively. The higher excited states (D₃–D₁₂) correspond to excitations from the singly occupied π orbital or from doubly occupied π orbitals to the lowest π^* orbital or higher σ^* orbitals. Most of the states are dark or exhibit very small oscillator strengths. The lowest state carrying significant oscillator strength ($f = 0.021$) is the D₁₂ state of ${}^2\pi\pi^*$ character with an excitation energy of 4.59 eV (270 nm). The corresponding excitation energies for the isolated PyH radical can be found in [ref 27](#). In general, the excitation energies of the PyH \cdots CO₂ complex are very similar to those of the isolated PyH radical since CO₂ does not absorb in the considered energy range and the hydrogen bond of CO₂ with PyH represents a weak perturbation of the latter.

[Figure 2a,b](#) displays the frontier Hartree–Fock molecular orbitals of PyH and the PyH \cdots CO₂ complex, respectively. The lowest excited state (D₁) in both systems corresponds to an excitation from the SOMO (4a'' for PyH, 6a'' for the PyH \cdots CO₂ complex) to the lowest π^* orbital (6a'' for PyH, 9a'' for the PyH \cdots CO₂ complex). The energy of the D₁ state is hardly affected by the hydrogen-bonded CO₂ molecule. The second excited state is of ${}^2\pi\sigma^*$ character where an electron from the SOMO located on PyH (4a'' or 6a'') is transferred to the LUMO (19a' or 28a').

For PyH, the LUMO is a diffuse Rydberg orbital that is located outside the pyridine ring and is antibonding with respect to the NH bond (see [Figure 2a](#)). In the PyH \cdots CO₂ complex, on the other hand, the diffuse σ^* orbital is located on the CO₂ molecule and forms a torus around the carbon atom (see [Figure 2b](#)). The D₂ state of the PyH \cdots CO₂ complex is a charge-transfer (CT) state in which one electronic charge is transferred from the PyH radical to the CO₂ molecule. The PyH \cdots CO₂ complex in the ${}^2\pi\sigma^*$ excited state thus consists of a CO₂ anion and a pyridinium cation. Despite the substantial difference in location and charge distribution of the σ^* orbital,

Table 1. Vertical Excitation Energies of the Pyridinyl-CO₂ Complex^a

state	UADC(2) aug-ccpVDZ	CC2 aug-ccpVDZ	EOM-CCSD aug-ccpVDZ	CASPT2 aug-ccpVDZ
D ₁ ($\pi\pi^*$)	1.86 (0.001)	1.71 (0.001)	1.78	1.33 (0.002)
D ₂ ($\pi\sigma^*$)	2.10 (0.002)	2.03 (0.001)	2.26	2.22 (0.004)
D ₃ ($\pi\sigma^*$)	2.74 (0.000)	2.66 (0.000)	2.93	2.87 (0.000)
D ₄ ($\pi\sigma^*$)	2.75 (0.000)	2.68 (0.000)	2.96	2.87 (0.002)
D ₅ ($\pi\sigma^*$)	3.32 (0.008)	3.24 (0.011)	3.51	3.49 (0.001)
D ₆ ($\pi\sigma^*$)	3.37 (0.000)	3.29 (0.000)	3.59	3.53 (0.000)
D ₇ ($\pi\pi^*$)	3.42 (0.001)	3.36 (0.002)	3.55	3.49 (0.013)
D ₈ ($\pi\sigma^*$)	3.64 (0.003)	3.57 (0.002)		3.69 (0.003)
D ₉ ($\pi\sigma^*$)	4.16 (0.000)	4.08 (0.000)		4.40 (0.000)
D ₁₀ ($\pi\pi^*$)	4.29 (0.003)	4.22 (0.005)	4.39	4.35 (0.008)
D ₁₁ ($\pi\sigma^*$)	4.30 (0.000)	4.22 (0.000)		4.45 (0.000)
D ₁₂ ($\pi\pi^*$)	4.59 (0.021)	4.52 (0.026)	4.60	4.60 (0.014)

^aOscillator strengths are given in parentheses.

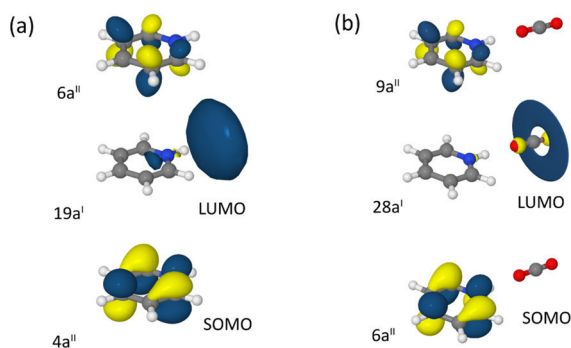


Figure 2. Hartree–Fock molecular orbitals of the PyH radical (a) and the PyH···CO₂ complex (b) at the respective ground-state equilibrium geometry. The singly occupied molecular orbital (SOMO) is a π orbital of pyridine. The lowest unoccupied molecular orbital (LUMO) of PyH (19a') is a Rydberg-like diffuse orbital. It is N–H antibonding, and the center of the charge distribution is located beyond the H atom of the NH group. In the PyH···CO₂ complex, the LUMO (28a') is located on the carbon atom of the CO₂ molecule. The second-lowest unoccupied molecular orbital (6a'' or 9a'', respectively) is a π^* orbital of pyridine.

the σ^* orbital energy of the PyH···CO₂ complex differs by only 0.05 eV from the σ^* orbital energy of the free PyH radical.

The ${}^2\pi\sigma^*$ state of CT character in the PyH···CO₂ complex can be populated via two pathways. First, the complex can be directly photoexcited to the lowest ${}^2\pi\sigma^*$ state by visible light. Although its calculated electronic oscillator strength in the fixed-nuclei approximation is very small (see Table 1), it may be enhanced by vibronic intensity borrowing from higher bright electronic states. Alternatively, the complex may be excited to higher-lying bright excited states from which it can relax by ultrafast internal conversion to the D₁(${}^2\pi\pi^*$) and D₂(${}^2\pi\sigma^*$) states. In ref 26, a rather dense spectrum of excited states of the PyH radical has been detected (by two-photon ionization) and assigned between 2.91 (426) and 4.13 eV (300 nm). The ionization potential of PyH is exceptionally low at 5.28 eV (235 nm). In the experiments of refs 25 and 26, the photochemistry was initiated by excitation at 254 nm (4.88 eV) and 255 nm (4.87 eV), respectively, just 0.4 eV below the lowest ionization threshold. This implies that excitation occurred into Rydberg excited states converging toward the

lowest ionization threshold. These Rydberg states have low oscillator strengths but are generically mixed with high-lying valence states, which have large oscillator strengths. According to Kasha's rule, the high-lying excited states of PyH are expected to relax to the lowest excited state(s) on ultrafast (femtosecond) timescales. The excess energy becoming available by the internal conversion process may enhance the reactivity of the complex in the D₁ and D₂ states.

As is well known, the equilibrium geometry of the CO₂ anion is bent with a bending angle of 138°. When vertically excited to the ${}^2\pi\sigma^*$ state, the PyH···CO₂ complex is at a geometry which is far from equilibrium. The ${}^2\pi\sigma^*$ PE surface therefore provides a strong driving force toward bending of the CO₂ molecule in the PyH···CO₂ complex. The bending in turn stabilizes the negative electronic charge on the carbon atom of CO₂. The energy of the ${}^2\pi\sigma^*$ state is further lowered by the transfer of the proton from the pyridinium cation to the CO₂ anion (the proton follows the electron). The concerted bending of the CO₂ anion and neutralization of the charge separation by proton transfer lead to the Py···HOCO product, as discussed in more detail below.

B. Reaction Paths and Energy Profiles for Photo-induced Reduction of CO₂. The equilibrium geometry of the Py···HOCO complex, optimized with the UMP2 method, is shown in Figure 1b. The electronic ground state is of A' symmetry since a σ orbital on the HOCO radical is singly occupied. The length of the hydrogen bond between Py and the HOCO radical is 1.594 Å, which indicates an unusually short and strong hydrogen bond. The energy of the Py···HOCO radical is 0.59 eV above the minimum energy of the PyH···CO₂ complex.

Figure 3a shows the two-dimensional relaxed PE surface of the ${}^2\pi\sigma^*$ state of the PyH···CO₂ complex calculated at the UADC(2) level. The OCO bending angle of the CO₂ molecule and the distance of the active proton from the oxygen atom of CO₂ were chosen as reaction coordinates. The educt geometry corresponds to the upper left corner (linear OCO molecule, H atom on Py). The lower right corner (OCO angle of 140°, H atom on OCO) corresponds approximately to the equilibrium geometry of the Py···HOCO radical. The two-dimensional relaxed PE surface could not be extended to OCO angles < 140° and R_{OH} < 1.2 Å due to convergence problems with the UADC(2) method. With the CASSCF/CASPT2 method, the

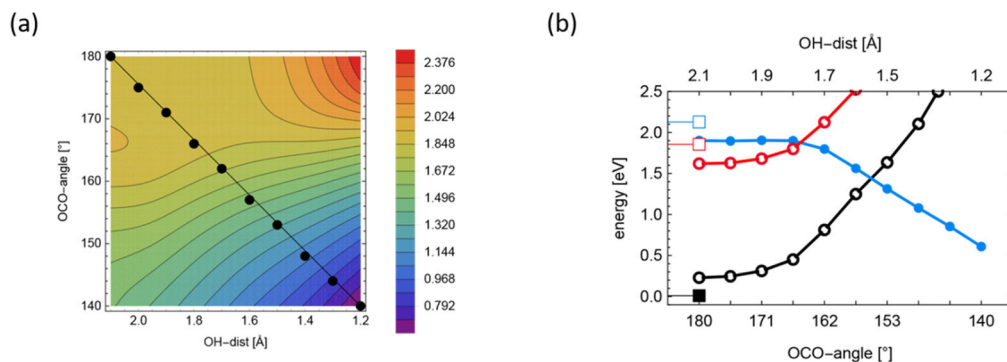


Figure 3. (a) Two-dimensional relaxed PE surface of the ${}^2\pi\sigma^*$ excited state of the PyH···CO₂ complex calculated at the UADC(2) level. The reaction coordinates are the OH distance of the HOCO fragment and the OCO bending angle of CO₂. The color code gives the energy (in eV) relative to the energy minimum of the electronic ground state. (b) Energy profiles of the D₀, ${}^2\pi\pi^*$ (D₁), and ${}^2\pi\sigma^*$ (D₂) electronic states along the line with dots indicated in panel (a). The energy of the lowest ${}^2\pi\sigma^*$ state (full circles) was optimized. The energies of the D₀ state and the lowest ${}^2\pi\pi^*$ state (open circles) were calculated at the same geometries. The squares represent the vertical excitation energies at the ground-state equilibrium geometry. Blue: $\pi\sigma^*$ state; red: $\pi\pi^*$ state; black: D₀ state.

surface could be extended to include an OCO angle of 120° and an OH distance of 1.0 Å. The relaxed PE surface of the ${}^2\pi\sigma^*$ state calculated with the CASSCF/CASPT2 method is presented in the [Supporting Information](#).

After population of the ${}^2\pi\sigma^*$ state by vertical electronic excitation or by rapid relaxation from higher excited states, as discussed above, the system is in the Franck–Condon region with an OCO angle of 180° and R_{OH} of 2.1 Å, which is a plateau of the PE surface shown in [Figure 3a](#). The ${}^2\pi\sigma^*$ surface exhibits a deep minimum at an OCO angle of 129° and an OH distance of 1.029 Å (beyond the lower right corner). It can be seen from [Figure 3a](#) that the PE function is repulsive for H-atom transfer in the linear configuration of CO_2 . Along the OCO angle for a fixed R_{OH} of 2.1 Å, the energy is stabilized apart from a small barrier near 166° (see [Figure 3a](#)).

The reactive ${}^2\pi\sigma^*$ surface displayed in [Figure 2](#) exhibits seams of intersection with the nonreactive surfaces of the lowest ${}^2\pi\pi^*$ state and the D_0 state. This is illustrated by a linear cut along the diagonal of [Figure 3a](#), which is indicated by the black line with dots. The energy profiles of the D_0 (black), ${}^2\pi\pi^*$ (red), and ${}^2\pi\sigma^*$ (blue) states along this cut are shown in [Figure 3b](#). The squares indicate the ground-state energy at the $\text{PyH}\cdots\text{CO}_2$ equilibrium geometry (full black square) and the vertical excitation energies of the ${}^2\pi\pi^*$ (red) and ${}^2\pi\sigma^*$ (blue) states (open squares).

At an OH distance of 2.1 Å, the relaxed energy of the ${}^2\pi\sigma^*$ state is 0.2 eV below the vertical excitation energy. The energy of the ${}^2\pi\pi^*$ state is also red-shifted by about 0.2 to 1.6 eV when the geometry is optimized in the ${}^2\pi\sigma^*$ state (see [Figure 3b](#)). The energy extrapolated to an OCO angle of 129° corresponds to the energy of the product and was calculated at the UMP2 level. The energy of the product is 0.59 eV above the ground-state energy minimum of $\text{PyH}\cdots\text{OCO}$. The energy profile of the ${}^2\pi\sigma^*$ state in [Figure 3b](#) reveals the existence of a barrierless pathway for the H-atom transfer reaction on the PE surface. Along this path, the energy of the lowest ${}^2\pi\sigma^*$ state crosses the energy of the lowest ${}^2\pi\pi^*$ state as well as the energy of the electronic ground state. These energy crossings represent conical intersections. The ${}^2\pi\sigma^*/{}^2\pi\pi^*$ (D_2/D_1) and ${}^2\pi\sigma^*/D_0$ (D_1/D_0) conical intersections are so-called symmetry-allowed conical intersections since the ${}^2\pi\sigma^*$ state transforms as A' , while the D_0 and ${}^2\pi\pi^*$ states transform as A'' in the C_s point group. The corresponding energy profiles along the diagonal of the ${}^2\pi\sigma^*$ surface obtained with the CASSCF/CASPT2 method are qualitatively similar and are discussed in the [Supporting Information](#).

For the isolated PyH radical, the relevant coupling modes of a'' symmetry at the two conical intersections were determined in [ref 27](#). It was shown that the dynamics at the ${}^2\pi\sigma^*/{}^2\pi\pi^*$ (D_2/D_1) conical intersection is determined by three strong coupling modes of a'' symmetry (Q_7 , Q_8 , Q_{13}), while the modes Q_9 , Q_{15} , and Q_{19} of a'' symmetry are the active modes at the ${}^2\pi\sigma^*/D_0$ (D_1/D_0) conical intersection.²⁷ The dynamics at these conical intersections in the isolated PyH radical was investigated with time-dependent quantum wave-packet calculations.²⁷

The nonadiabatic dynamics at the D_2/D_1 and D_1/D_0 conical intersections of the $\text{PyH}\cdots\text{CO}_2$ complex determines the branching ratios of the reaction. Diabatic crossing of both conical intersections leads to H-atom transfer from PyH to CO_2 . Adiabatic crossing at either conical intersection with subsequent vibronic energy relaxation leads to recovery of the

$\text{PyH}\cdots\text{CO}_2$ complex in the electronic ground state. The computational simulation of the nonadiabatic dynamics at these conical intersections of the $\text{PyH}\cdots\text{CO}_2$ complex is a challenging problem that is beyond the scope of the present work.

IV. DISCUSSION AND CONCLUSIONS

We have explored in this work basic descriptors of the photochemistry of the $\text{PyH}\cdots\text{CO}_2$ complex with state-of-the-art electronic structure calculations. The vertical electronic excitation spectrum of $\text{PyH}\cdots\text{CO}_2$ is found to be, as expected, very similar to the electronic excitation spectrum of the isolated PyH radical. This result notwithstanding, a look at the Hartree–Fock molecular orbitals at the ground-state equilibrium geometry of $\text{PyH}\cdots\text{CO}_2$ reveals a significant effect of the complexation of PyH with CO_2 . The lowest diffuse σ^* orbital occupied in the ${}^2\pi\sigma^*$ excited state locates spontaneously (that is, without nuclear motion) on the CO_2 molecule, forming an eye-catching torus around the electron-deficient carbon atom of CO_2 ([Figure 2b](#)). Due to its ($\text{PyH}^+\cdots\text{OCO}^-$) charge-separated character, the energy of the ${}^2\pi\sigma^*$ excited state is strongly stabilized by the bending of the OCO angle (the equilibrium structure of the CO_2^- anion is bent^{37,38}). In addition, the ${}^2\pi\sigma^*$ excited state is stabilized by the transfer of the proton from PyH^+ to CO_2^- (the proton follows the electron). This phenomenon exhibits analogies to the photochemistry in ${}^1\pi\sigma^*$ excited states of pyrrole-water or phenol-water clusters, where the electron density of the σ^* orbital drives the transfer of a proton from the chromophore to a hydrogen-bonded water or ammonia molecule, forming H_3O or NH_4 radicals.

As a result of the stabilizing effects of OCO bending and proton transfer, the ${}^2\pi\sigma^*$ PE surface exhibits a barrierless reaction path from the $\text{PyH}\cdots\text{OCO}$ structure ([Figure 1a](#)) to the $\text{Py}\cdots\text{HOCO}$ structure ([Figure 1b](#)) with a significant stabilization energy of about 0.6 eV at the UADC(2) level. At the CASSCF/CASPT2 level, a small barrier of about 0.05 eV is found, which is below the zero-point energy of the NH stretching vibration ([Figure S3b](#)). Along this approximate reaction path, the energy profile of the reactive ${}^2\pi\sigma^*$ state intersects the energy profiles of the nonreactive D_0 and ${}^2\pi\pi^*$ states, as shown in [Figure 3b](#). The figure reveals the existence of a barrier of about 1.5 eV in the electronic ground state, which separates the energy minimum of the $\text{PyH}\cdots\text{OCO}$ complex from the energy minimum of the $\text{Py}\cdots\text{HOCO}$ complex.

[Figure 3b](#) qualitatively explains why CO_2 cannot be reduced by the PyH radical in the electronic ground state under ambient conditions. The photochemical reaction on the ${}^2\pi\sigma^*$ PE surface, on the other hand, is barrierless, albeit two conical intersections have to be passed diabatically (that is, following the diabatic ${}^2\pi\sigma^*$ state rather than switching to the ${}^2\pi\pi^*$ state or the D_0 state). While the D_0 state and the ${}^2\pi\pi^*$ state are of A'' symmetry, the ${}^2\pi\sigma^*$ state is of A' symmetry. The two conical intersections are thus of the symmetry-allowed type in the terminology of Yarkony.³⁹ The possible product channels are the ${}^2\pi\pi^*$ excited state, the D_0 state of $\text{PyH}\cdots\text{OCO}$, or the D_0 state of $\text{Py}\cdots\text{HOCO}$ at their respective equilibrium geometries. Nonadiabatic quantum wave-packet calculations or quasi-classical surface-hopping trajectory simulations are necessary to estimate the branching ratios into these channels.

The possibility of a photoinduced excited-state PCET reaction of PyH with CO_2 was not considered in previous

investigations of the catalytic role of the PyH radical in the reduction of CO₂. The present results provide a tentative explanation of the observations of Bocarsly and co-workers for the photoelectrochemical reduction of CO₂ using an illuminated GaP electrode^{5,6} as well as of the observations of Colussi and co-workers for homogeneous photochemical reduction of CO₂.²⁵ When the PyH radical is photochemically generated by H-atom abstraction from a H₂O molecule and the H atom is subsequently photochemically transferred to CO₂, the reduction of CO₂ is a purely light-driven process. These photochemical reactions of water and carbon dioxide with an exceptionally simple chromophore may serve as a blueprint for future developments of solar-driven generation of clean fuels from CO₂.

Py is not the ideal chromophore for solar water oxidation and hydrogen evolution. Py absorbs in the UV, and the absorbing ¹ππ* state has a very short lifetime due to easily accessible ¹ππ*-S₀ conical intersections of the ring-puckering type.^{40,41} It has been shown in a recent computational study that the fast quenching of the ¹ππ* excited-state of Py results in a low reaction probability for PCET in Py-water clusters.⁴² While the PyH radical exhibits low-lying excited electronic states, their oscillator strengths are very low (Table 1). To what extent the excited states of PyH are quenched by internal conversion via ring-puckering conical intersections is currently not known.

A more suitable chromophore for photocatalytic water oxidation and carbon dioxide reduction could be heptazine (heptaazaphenalene or tri-*s*-triazine, C₆N₇H₃). Heptazine is the building block of the polymer “melon”, generally referred to as graphitic carbon nitride (g-C₃N₄) in the literature.⁴³ The heptazine chromophore possesses a very weakly absorbing ¹ππ* state with an excitation energy of about 2.6 eV (477 nm) and a strongly absorbing second ¹ππ* state near 4.0 eV (310 nm). Due to the fused ring structure, excited-state quenching by ring-puckering conical intersection is suppressed in heptazine. The S₁ state of heptazine therefore exhibits a nanosecond lifetime and a high fluorescence quantum yield.⁴⁴ It has been predicted that the heptazinyl radical (C₆N₇H₄) possesses, like PyH, a low-lying (3.2 eV) excited state, which drives the detachment of the excess hydrogen atom.⁴⁵ The heptazinyl radical may therefore be a promising chromophore for the photocatalytic reduction of CO₂. It has indeed been shown that heptazine-based carbon nitride in combination with a ruthenium organometallic complex can reduce CO₂ to CO and formic acid with visible light.^{46–48} Oxygen-doped and carbon-deficient carbon nitride materials also have been found to exhibit photocatalytic CO₂ reduction activity.^{49,50} Homogeneous photocatalytic CO₂ reduction with heptazine-derived molecular chromophores has not yet been explored but seems promising when comparing the relevant parameters of the heptazinyl radical with those of the pyridinyl radical.

■ ASSOCIATED CONTENT

● Supporting Information

The Supporting Information is available free of charge on the ACS Publications website at DOI: 10.1021/acs.jpca.9b01292.

Description of CASSCF/CASPT2 calculations for the PyH...OCO complex. Relaxed two-dimensional PE surfaces at the CASSCF/CASPT2 level and at the UMP2 level (PDF)

■ AUTHOR INFORMATION

Corresponding Author

*E-mail: domcke@ch.tum.de.

ORCID

Andrzej L. Sobolewski: 0000-0001-5718-489X

Wolfgang Domcke: 0000-0001-6523-1246

Notes

The authors declare no competing financial interest.

■ ACKNOWLEDGMENTS

This work has been supported by the Munich Centre for Advanced Photonics (MAP). J.E. acknowledges support by the International Max Planck Research School of Advanced Photon Science (IMPRS-APS). A.S. acknowledges support by the Alexander von Humboldt Research Award.

■ REFERENCES

- (1) Kumar, B.; Llorente, M.; Froehlich, J.; Dang, T.; Sathrum, A.; Kubiak, C. P. Photochemical and Photoelectrochemical Reduction of CO₂. *Annu. Rev. Phys. Chem.* **2012**, *63*, 541–569.
- (2) White, J. L.; Baruch, M. F.; Pander, J. E., III; Hu, Y.; Fortmeyer, I. C.; Park, J. E.; Zhang, T.; Liao, K.; Gu, J.; Yan, Y.; et al. Light-Driven Heterogeneous Reduction of Carbon Dioxide: Photocatalysts and Photoelectrodes. *Chem. Rev.* **2015**, *115*, 12888–12935.
- (3) Wang, W.-H.; Himeda, Y.; Muckerman, J. T.; Manbeck, G. F.; Fujita, E. CO₂ Hydrogenation to Formate and Methanol as an Alternative to Photo- and Electrochemical CO₂ Reduction. *Chem. Rev.* **2015**, *115*, 12936–12973.
- (4) Seshadri, G.; Lin, C.; Bocarsly, A. B. A New Homogeneous Electrocatalyst for the Reduction of Carbon Dioxide to Methanol at Low Overpotential. *J. Electroanal. Chem.* **1994**, *372*, 145–150.
- (5) Barton, E. E.; Rampulla, D. M.; Bocarsly, A. B. Selective Solar-Driven Reduction of CO₂ to Methanol Using a Catalyzed p-GaP Based Photoelectrochemical Cell. *J. Am. Chem. Soc.* **2008**, *130*, 6342–6344.
- (6) Keets, K. A.; Cole, E. B.; Morris, A. J.; Sivasankar, N.; Teamey, K.; Lakkaraju, P. S.; Bocarsly, A. B. Analysis of Pyridinium Catalyzed Electrochemical and Photoelectrochemical Reduction of CO₂: Chemistry and Economic Impact. *Indian J. Chem.* **2012**, *51A*, 1284–1297.
- (7) Barton Cole, E.; Lakkaraju, P. S.; Rampulla, D. M.; Morris, A. J.; Abelev, E.; Bocarsly, A. B. Using a One-Electron Shuttle for the Multielectron Reduction of CO₂ to Methanol: Kinetic, Mechanistic, and Structural Insights. *J. Am. Chem. Soc.* **2010**, *132*, 11539–11551.
- (8) Morris, A. J.; McGibbon, R. T.; Bocarsly, A. B. Electrocatalytic Carbon Dioxide Activation: The Rate-Determining Step of Pyridinium-Catalyzed CO₂ Reduction. *ChemSusChem* **2011**, *4*, 191–196.
- (9) Keith, J. A.; Carter, E. A. Theoretical Insights into Pyridinium-Based Photoelectrocatalytic Reduction of CO₂. *J. Am. Chem. Soc.* **2012**, *134*, 7580–7583.
- (10) Keith, J. A.; Carter, E. A. Electrochemical Reactivities of Pyridinium in Solution: Consequences for CO₂ Reduction Mechanisms. *Chem. Sci.* **2013**, *4*, 1490–1496.
- (11) Muñoz-García, A. B.; Carter, E. A. Non-Innocent Dissociation of H₂O on GaP (110): Implications for Electrochemical Reduction of CO₂. *J. Am. Chem. Soc.* **2012**, *134*, 13600–13603.
- (12) Keith, J. A.; Muñoz-García, A. B.; Lessio, M.; Carter, E. A. Cluster Models for Studying CO₂ Reduction on Semiconductor Photoelectrodes. *Top. Catal.* **2015**, *58*, 46–56.
- (13) Lessio, M.; Carter, E. A. What Is the Role of Pyridinium in Pyridine-Catalyzed CO₂ Reduction on p-GaP Photocathodes? *J. Am. Chem. Soc.* **2015**, *137*, 13248–13251.
- (14) Senftle, T. P.; Lessio, M.; Carter, E. A. Interaction of Pyridine and Water with the Reconstructed Surfaces of GaP(111) and

CdTe(111) Photoelectrodes: Implications for CO₂ Reduction. *Chem. Mater.* **2016**, *28*, 5799–5810.

(15) Lessio, M.; Riplinger, C.; Carter, E. A. Stability of Surface Protons in Pyridine-Catalyzed CO₂ reduction at p-GaP Photoelectrodes. *Phys. Chem. Chem. Phys.* **2016**, *18*, 26434–26443.

(16) Lessio, M.; Senftle, T. P.; Carter, E. A. Is the Surface Playing a Role during Pyridine-Catalyzed CO₂ Reduction on p-GaP Photoelectrodes? *ACS Energy Lett.* **2016**, *1*, 464–468.

(17) Senftle, T. P.; Lessio, M.; Carter, E. A. The Role of Surface-Bound Dihydropyridine Analogues in Pyridine-Catalyzed CO₂ Reduction over Semiconductor Photoelectrodes. *ACS Cent. Sci.* **2017**, *3*, 968–974.

(18) Lessio, M.; Dieterich, J. M.; Carter, E. A. Hydride Transfer at the GaP(110)/Solution Interface: Mechanistic Implications for CO₂ Reduction Catalyzed by Pyridine. *J. Phys. Chem. C* **2017**, *121*, 17321–17331.

(19) Xu, S.; Li, L.; Carter, E. A. Why and How Carbon Dioxide Conversion to Methanol Happens on Functionalized Semiconductor Photoelectrodes. *J. Am. Chem. Soc.* **2018**, *140*, 16749–16757.

(20) Lim, C. H.; Holder, A. M.; Musgrave, C. B. Mechanism of Homogeneous Reduction of CO₂ by Pyridine: Proton Relay in Aqueous Solvent and Aromatic Stabilization. *J. Am. Chem. Soc.* **2012**, *135*, 142–154.

(21) Keith, J. A.; Carter, E. A. Theoretical Insights into Electrochemical CO₂ Reduction Mechanisms Catalyzed by Surface-Bound Nitrogen Heterocycles. *J. Phys. Chem. Lett.* **2013**, *4*, 4058–4063.

(22) Lim, C.-H.; Holder, A. M.; Hynes, J. T.; Musgrave, C. B. Catalytic Reduction of CO₂ by Renewable Organohydrides. *J. Phys. Chem. Lett.* **2015**, *6*, 5078–5092.

(23) Ertem, M. Z.; Konezny, S. J.; Araujo, C. M.; Batista, V. S. Functional Role of Pyridinium during Aqueous Electrochemical Reduction of CO₂ on Pt (111). *J. Phys. Chem. Lett.* **2013**, *4*, 745–748.

(24) Yan, Y.; Gu, J.; Bocarsly, A. B. Hydrogen Bonded Pyridine Dimer: A Possible Intermediate in the Electrocatalytic Reduction of Carbon Dioxide to Methanol. *Aerosol Air Qual. Res.* **2014**, *14*, 515–521.

(25) Riboni, F.; Selli, E.; Hoffmann, M. R.; Colussi, A. J. Homogeneous Reduction of CO₂ by Photogenerated Pyridinyl Radicals. *J. Phys. Chem. A* **2014**, *119*, 4433–4438.

(26) Esteves-López, N.; Coussan, S.; Dedonder-Lardeux, C.; Jovet, C. Photoinduced Water Splitting in Pyridine-Water Clusters. *Phys. Chem. Chem. Phys.* **2016**, *18*, 25637–25644.

(27) Ehrmaier, J.; Picconi, D.; Karsili, T. N.; Domcke, W. Photodissociation Dynamics of the Pyridinyl Radical: Time-Dependent Quantum Wave-Packet Calculations. *J. Chem. Phys.* **2017**, *146*, 124304.

(28) Schirmer, J. Beyond the Random-Phase Approximation: A new Approximation Scheme for the Polarization propagator. *Phys. Rev. A* **1982**, *26*, 2395–2416.

(29) Hättig, C.; Weigend, F. CC2 Excitation Energy Calculations on Large Molecules Using the Resolution of the Identity Approximation. *J. Chem. Phys.* **2000**, *113*, 5154–5161.

(30) Starcke, J. H.; Wormit, M.; Dreuw, A. Unrestricted Algebraic Diagrammatic Construction Scheme of Second Order for the Calculation of Excited States of Medium-Sized and Large Molecules. *J. Chem. Phys.* **2009**, *130*, No. 024104.

(31) Stanton, J. F.; Bartlett, R. J. The Equation of Motion Coupled-Cluster Method. A Systematic Biorthogonal Approach to Molecular Excitation Energies, Transition Probabilities, and Excited State Properties. *J. Chem. Phys.* **1993**, *98*, 7029–7039.

(32) Roos, B. O.; Andersson, K. Multiconfigurational Perturbation Theory with Level Shift—the Cr₂ Potential Revisited. *Chem. Phys. Lett.* **1995**, *245*, 215–223.

(33) Dunning, T. H., Jr. Gaussian Basis Sets for Use in Correlated Molecular Calculations. I. The Atoms Boron Through Neon and Hydrogen. *J. Chem. Phys.* **1989**, *90*, 1007–1023.

(34) TURBOMOLE (V6.3), a Development of University of Karlsruhe and Forschungszentrum Karlsruhe GmbH, 1989–2007, TURBOMOLE GmbH, 2011.

(35) Shao, Y.; Gan, Z.; Epifanovsky, E.; Gilbert, A. T.; Wormit, M.; Kussmann, J.; Lange, A. W.; Behn, A.; Deng, J.; Feng, X.; Ghosh, D. Advances in Molecular Quantum Chemistry Contained in the Q-Chem 4 Program Package. *Mol. Phys.* **2014**, *113*, 184–215.

(36) Werner, H.-J.; Knowles, P.; Knizia, G.; Manby, F.; Schütz, M.; Celani, P.; Györffy, W.; Kats, D.; Korona, T.; Lindh, R., *MOLPRO*, 2012.1, a Package of Ab Initio Programs, 2012.

(37) Schröder, D.; Schalley, C. A.; Harvey, J. N.; Schwarz, H. On the Formation of the Carbon Dioxide Anion Radical CO₂^{•−} in the Gas Phase. *Int. J. Mass Spectrom.* **1999**, *185-187*, 25–35.

(38) Sommerfeld, T.; Meyer, H.-D.; Cederbaum, L. S. Potential Energy Surface of the CO₂^{•−} Anion. *Phys. Chem. Chem. Phys.* **2004**, *6*, 42–45.

(39) Yarkony, D. R., Conical Intersections: Their Description and Consequences. In: *Conical Intersections: Electronic Structure, Dynamics & Spectroscopy*; Eds. Domcke, W., Yarkony, D. R., Köppel, H., World Scientific: Singapore, 2004; pp 41–127.

(40) Sobolewski, A. L.; Domcke, W. Photophysically Relevant Potential Energy Functions of Low-Lying Singlet States of Benzene, Pyridine and Pyrazine: an Ab Initio Study. *Chem. Phys. Lett.* **1991**, *180*, 381–386.

(41) Varras, P. C.; Gritzapis, P. S.; Fylaktakidou, K. C. An Explanation of the Very Low Fluorescence and Phosphorescence in Pyridine: a CASSCF/CASMP2 Study. *Mol. Phys.* **2017**, *116*, 154–170.

(42) Pang, X.; Jiang, C.; Xie, W.; Domcke, W., Photoinduced Electron-Driven Proton Transfer from Water to an N-Heterocyclic Chromophore: Nonadiabatic Dynamics Studies for Pyridine-Water Clusters. *Phys. Chem. Chem. Phys.* **2019**, in press DOI: 10.1039/c8cp07015f.

(43) Wang, Y.; Wang, X.; Antonietti, M. Polymeric Graphitic Carbon Nitride as a Heterogeneous Organocatalyst: From Photochemistry to Multipurpose Catalysis to Sustainable Chemistry. *Angew. Chem. Int. Ed.* **2012**, *51*, 68–89.

(44) Merschjann, C.; Tyborski, T.; Orthmann, S.; Yang, F.; Schwarzburg, K.; Lublow, M.; Lux-Steiner, M.-C.; Schedel-Niedrig, T. Photophysics of Polymeric Carbon Nitride: An Optical Quasimonomer. *Phys. Rev. B* **2013**, *87*, 205204.

(45) Ehrmaier, J.; Karsili, T. N. V.; Sobolewski, A. L.; Domcke, W. Mechanism of Photocatalytic Water Splitting with Graphitic Carbon Nitride: Photochemistry of the Heptazine–Water Complex. *J. Phys. Chem. A* **2017**, *121*, 4754–4764.

(46) Kuriki, R.; Sekizawa, K.; Ishitani, O.; Maeda, K. Visible-Light-Driven CO₂ Reduction with Carbon Nitride: Enhancing the Activity of Ruthenium Catalysts. *Angew. Chem. Int. Ed.* **2015**, *54*, 2406–2409.

(47) Kuriki, R.; Ishitani, O.; Maeda, K. Unique Solvent Effects on Visible-Light CO₂ Reduction over Ruthenium(II)-Complex/Carbon Nitride Hybrid Photocatalysts. *ACS Appl. Mater. Interfaces* **2016**, *8*, 6011–6018.

(48) Kuriki, R.; Matsunaga, H.; Nakashima, T.; Wada, K.; Yamakata, A.; Ishitani, O.; Maeda, K. Nature-Inspired, Highly Durable CO₂ Reduction System Consisting of a Binuclear Ruthenium(II) Complex and an Organic Semiconductor Using Visible Light. *J. Am. Chem. Soc.* **2016**, *138*, 5159–5170.

(49) Fu, J.; Zhu, B.; Jiang, C.; Cheng, B.; You, W.; Yu, J. Hierarchical Porous O-Doped g-C₃N₄ with Enhanced Photocatalytic CO₂ Reduction Activity. *Small* **2017**, *13*, 1603938.

(50) Yang, P.; Zhuzhang, H.; Wang, R.; Lin, W.; Wang, X. Carbon Vacancies in a Melon Polymeric Matrix Promote Photocatalytic Carbon Dioxide Conversion. *Angew. Chem. Int. Ed.* **2019**, *58*, 1134–1137.